Synthesis and Study of Different Carbon Nanomaterials: Diamond like Carbon, Carbon Nanoflakes and Graphene Thin Films

A thesis submitted

by

Mukesh Singh

Roll No: 09612117

In partial fulfillment of the requirement for the award of the degree of Doctor of Philosophy

Department of Physics
Indian Institute of Technology, Guwahati
Guwahati – 781 039, Assam, India

November 2015

DECLARATION

The work contained in this thesis entitled **"Synthesis and Study of Different Carbon Nanomaterials: Diamond like Carbon, Carbon Nanoflakes and Graphene Thin Films"** has been carried out by me under the supervision of Dr. Pratima Agarwal, Professor, Department of Physics, Indian Institute of Technology, Guwahati, Assam, India. This thesis does not contain any materials previously submitted for the award of any degree or diploma.

Mukesh Singh

Date: Nov 25, 2015

Mukesh Singh
Department of Physics
Indian Institute of Technology Guwahati
Guwahati-781039, Assam, India

DECLARATION

The work contained in this thesis entitled **"Synthesis and Study of Different Carbon Nanomaterials: Diamond like Carbon, Carbon Nanoflakes and Graphene Thin Films"** has been carried out by me under the supervision of Dr. Pratima Agarwal, Professor, Department of Physics, Indian Institute of Technology, Guwahati, Assam, India. This thesis does not contain any materials previously submitted for the award of any degree or diploma.

Date: Nov 25, 2015

Mukesh Singh
Department of Physics
Indian Institute of Technology Guwahati
Guwahati-781039, Assam, India

भारतीय प्रौद्योगिकी संस्थान गुवाहाटी
Indian Institute of Technology Guwahati
North Guwahati, Guwahati
PIN- 781 039, Assam State, INDIA
Phone: +91 361 2583000 Extn 2702, 2582702
Fax: +91 361 2690 762 (Institute). 2582749 (Department)

Dr. Pratima Agarwal
Professor
Department of Physics
E-mail:pratima@iitg.ernet.in

Dated: Nov 25, 2015

CERTIFICATE

This is certified that the work contained in this thesis entitled **"Synthesis and Study of Different Carbon Nanomaterials: Diamond like Carbon, Carbon Nanoflakes and Graphene Thin Films"**submitted by Mr. Mukesh Singh, a Ph.D. student in the Department of Physics, Indian Institute of Technology, Guwahati, Assam, India, for the award of the degree of Doctor of Philosophy has been carried out under my supervision. This work has not been submitted elsewhere for the award of any degree or diploma.

Pratima Agarwal
(Dr. Pratima Agarwal)

भारतीय प्रौद्योगिकी संस्थान गुवाहाटी
Indian Institute of Technology Guwahati
North Guwahati, Guwahati
PIN- 781 039, Assam State, INDIA
Phone: +91 361 2583000 Extn 2702, 2582702
Fax: +91 361 2690 762 (Institute), 2582749 (Department)

Dr. Pratima Agarwal
Professor
Department of Physics
E-mail:pratima@iitg.ernet.in

Dated: Nov 25, 2015

CERTIFICATE

This is certified that the work contained in this thesis entitled **"Synthesis and Study of Different Carbon Nanomaterials: Diamond like Carbon, Carbon Nanoflakes and Graphene Thin Films"** submitted by Mr. Mukesh Singh, a Ph.D. student in the Department of Physics, Indian Institute of Technology, Guwahati, Assam, India, for the award of the degree of Doctor of Philosophy has been carried out under my supervision. This work has not been submitted elsewhere for the award of any degree or diploma.

(Dr. Pratima Agarwal)

Dedicated

to

my grandfather and parents

for their love and

encouragement

Acknowledgements

I am extremely grateful to my thesis supervisor, Prof. Pratima Agarwal, for her continuous support and guidance throughout my Ph.D. work. She taught me a lot on how to approach research problems, how to analyze and understand the results from a physicist's perspective. I am very thankful to her for giving me opportunity to work under her supervision and will remain ever grateful to her.

I am grateful to my doctoral committee members Prof. Alika Khare (Chairperson), Prof. Saurabh Basu and Prof. G. Krishnamoorthy for reviewing my research work regularly and giving valuable suggestions. I am thankful to earlier head of Department of Physics Prof. S. Ravi, Prof. Saurabh Basu and current Head of Department Prof. Poulose Poulose as well as all the faculty members of the Department of Physics for their support.

I am grateful to Prof. S. C. Agarwal, visiting faculty in Department of Physics, for the valuable discussion in different area of research.

I am grateful to Dr. Shailendra Kumar, Indus Synchrotron Utilization Division, RRCAT, Indore and Dr. D. M. Phase UGC-DAE Consortium for Scientific research, Indore, for XPS measurement. I am also grateful to Dr. Rajeev Gupta, Department of Physics, I.I.T. Kanpur for Raman measurement on some of the samples in present thesis. I would like to thank his students for their help during measurements.

I would like to acknowledge my lab mates seniors Dr. J. Anto Pradeep, Dr. Himanshu S. Jha and my colleagues Mr. Lalhriatzuala, Mr. Ramakrishna Madka, Ms. Asha Yadav, Mr. Venkanna Kanneboina and Mr. Suman Sarkar for providing an ambient atmosphere for research in the lab as well as for their help in my research work. I would also like to thank undergraduate project students Mr. Anjani K. Maurya, Ms. Sayanti Banerjee, Mr. Bholuram Swami and Mr. Adesh Kumar for their help in different stages of my thesis work.

I am very fortunate to have friends Dr. Subbarao V.V. Nimmakayala, Mr. Indrajeet Kumar, Mr. Biroju Ravi Kumar and Mr. Nilanjan Mandal for their help during my research work.

I would like to express my sincere thanks to all the staff members of Department of Physics including Dr. Sidananda Sarma, Mr. Lokesh Chakraborty, Mr. Atul Deka and Mr. Basab B. Purakayastha for their support and cooperation during my research work.

I would like to acknowledge CIF, IIT Guwahati for using CIF facilities and I am also thankful to technical officers Mr. Chandan Borgohain, Dr. K.K. Senapati, Mr. Madhurjya Borah and Mr. Kh. Kesho Singh.

I would like to thank Prof. Alika Khare, Department of Physics, for allow me to do nonlinear measurements on some of my samples in “Lasers and Photonics lab”.

I would like to thank Prof. P. K. Iyer, Department of Chemistry, for allow me to do some measurements in “Center for organic electronics lab”.

I would also like to thank Prof. Perumal Alagarsamy, Department of Physics, for allow me to do the thickness measurement using stylus profilometer and I also thank to Prof. S. Ravi, Department of Physics, for allow me to do some measurements in “Magnetism lab”.

I am thankful to all the research scholars of Department of Physics for their help and wonderful time shared with me.

I am also thankful to Dr. Dilip K. Singh, Dr. Satchi Kumari, Dr. Enamullah Khan, Dr. Satendra Kumar, Dr. Akhilesh K. Singh, Dr. Onkar N. Verma, Mr. Upendra Kumar, Ms. Nisha Shankhwar, Mr. Ram Kumar, Mr. Partha P. Dey, Mr. Gyan P. Bharti, Mr. Rahul Kesarwani, Mr. Anil Kumar C, Mr. Prahlad K. Baruah and all other friends.

My special thanks go to Mr. Subash Pai of M/s Excel Instruments for fabricating the HFCVD system as per our design and requirement.

I am grateful to IIT Guwahati for providing the financial support during my present thesis work.

Last but not the least, I would like to thank my family members for their patience and constant support in my life and finally I would like to thank God for the blessings.

Mukesh Singh

Guwahati

Preface

Carbon is the fourth most abundant element on the earth. The diversity in different hybridized states of carbon makes unlimited number of different allotropes such as diamond like carbon (DLC), graphite, graphene, carbon nanotubes (CNT), carbon nanoflakes (CNF), carbon nanofibers, fullerene, etc. All these structures have different hybridized state of carbon, in which structures are formed by only sp^1, sp^2 or sp^3 or combined phase of sp^2 and sp^3 hybridized carbon atoms. Diamond like carbon is stable form of amorphous carbon containing mix phase of sp^3 ($\leq 40\%$) and sp^2 ($\leq 60\%$) bonded carbon. It is low mobility semiconductor having wide band gap of 1 – 4 eV. A very thin layer (~ few nm thick) of diamond like carbon films is used to increase the hardness as well as the life time of different mechanical and surgical tools. Carbon nanoflakes are a type of vertically aligned carbon nanostructure having large specific surface area of 300 – 700 m^2/g. Due to large surface area and having high carrier mobility, CNF can be used as current collector electrode in different charge storage devices like battery, supercapacitor, etc. Apart from these carbon nanostructures, discovery of graphene has opened huge possibilities in the field of electronic devices due to high carrier mobility (~ 1000 – 15000 $cm^2/V\text{-}s$) and high current density (~ 10^8 A/cm^2). Therefore, it is expected to play an important role in electronic devices in the field of applied nanotechnology in near future. For the development of devices on large scale, cost effective growth of defect free graphene films of large area are very important. Therefore, researchers are developing different methods for the growth of high quality graphene films at low cost. Although, graphene is chemically inert material, under certain conditions it reacts with various organic and inorganic reactants which increase the diversity in different fields of research.

The thesis work is mainly focused on the preparation of various allotropes of carbon: diamond like carbon, carbon nanoflakes, single and multi-layers graphene thin films using less explored but highly versatile hot filament chemical vapor deposition (HFCVD) method and preparation of graphene oxide (GO) using chemical routes as well as reduction of GO. This thesis also presents the structural, optical and electrical properties of these carbon nanomaterials. The aim of present thesis work is to optimize the deposition parameters for the growth of different carbon nanomaterials. Films are prepared by varying different deposition parameters such as process pressure, substrate temperature, deposition time, precursor gas flow rate and substrate to filament distance using HFCVD method. These films are characterized by field emission scanning electron microscopy (FESEM), atomic force microscopy (AFM), Raman scattering, Fourier transform infrared spectroscopy (FTIR), X-ray photoelectron spectroscopy (XPS), transmission electron microscopy (TEM), UV-Vis-NIR spectroscopy, Z-scan (third order optical nonlinearity) and I-V measurements for the study of structural, optical and electrical properties.

The present thesis work is divided into eight chapters. Chapter 1 is introduction, which gives a brief introductory idea about the different form of carbon allotropes along with literature review. The motivation of the present work and outline of the thesis are also contained in this chapter. Chapter 2 gives a quick review on the description of HFCVD system and a brief discussion about different characterization techniques used for the study of structural, optical and electrical properties of the films. Chapter 3 contains the extensive studies on the influence of different deposition parameters for the growth and microstructural properties of diamond like carbon thin films. Chapter 4 presents a systematic study on the influence of different deposition parameters for the growth and microstructural properties of carbon nanoflakes. This chapter also contains the study of electrical and optical (linear/nonlinear) properties of some of the films. Chapter 5 presents the influence of different deposition parameters on the growth of single and multi-layers graphene films and study the structural, optical (linear/nonlinear) and electrical properties of the films. Chapter 6 presents the study of structural, optical and electrical properties of functionalized graphene oxide and thermally reduced GO (rGO) thin films. Chapter 7 is on the study of transport properties of charge carriers in graphene using as fabricated graphene channel field effect transistor and finally in chapter 8, we have summarized the results and also present the future scope of the work.

ABBREVIATIONS AND SYMBOLS

DLC	Diamond like carbon
NCD	Nanocrystalline diamond
CNT	Carbon nanotubes
CNF	Carbon nanoflakes
a-C	Amorphous carbon
a-C:H	Hydrogenated amorphous carbon
GO	Graphene Oxide
rGO	reduced Graphene Oxide
CVD	Chemical vapor deposition
rf-PECVD	radio frequency – plasma enhanced chemical vapor deposition
DC-PECVD	Direct current – plasma enhanced chemical vapor deposition
HFCVD	Hot filament chemical vapor deposition
MWCVD	Microwave chemical vapor deposition
Cat-CVD	Catalytic chemical vapor deposition
c-BN	Cubic – Boron Nitride
SiC	Silicon Carbide
HOPG	Highly ordered pyrolytic graphite
1D/2D/3D	One/two/three dimension
SS	Stainless Steel
ITO	Indium tin oxide
c-Si	Crystalline silicon
UV-Vis-NIR	Ultraviolet – visible – near infrared
FESEM	Field emission scanning electron microscopy
AFM	Atomic force microscopy
XRD	X-ray diffraction

FTIR	Fourier transform infrared
XPS	X-ray photoelectron spectroscopy
TEM	Transmission electron microscopy
HRTEM	High resolution transmission electron microscopy
SAED	Selected area electron diffraction
PMMA	Poly methyl methacrylate
GFET	Graphene channel field effect transistor
$\mathbf{T_S}$	Substrate temperature
PP	Process pressure
$\mathbf{t_d}$	Deposition time
sccm	Standard cubic centimeter per minute
FWHM	Full width at half maxima
eV	Electron volt
at %	Atomic percentage
$\mathbf{n_2}$	Third order optical nonlinear refractive index coefficient
$\mathbf{n_r}$	Refractive index
n	Number of graphene layers
$\mathbf{L_a}$	average grain size of sp^2 bonded carbon atoms
$\mathbf{E_a}$	Activation energy
$\mathbf{K_B}$	Boltzmann constant
$\mathbf{E_L}$	Laser energy
$\boldsymbol{\lambda}$	Wavelength
$\boldsymbol{\sigma}$	Electrical conductivity
$\boldsymbol{\mu}$	Carrier mobility

CONTENTS

Chapter 6: Graphene Oxide and Thermally Reduced Graphene Oxide Thin Films 121

LIST OF FIGURES

LIST OF TABLES

Chapter 1

Introduction

Carbon is an essential material for life on the earth. Carbon based systems show unlimited number of different allotropes, such as diamond like carbon (DLC), diamond, graphene, carbon nanotubes (CNT), carbon nanoflakes (CNF), fullerene, etc [1, 2]. The reason of different allotropes of carbon based systems is due to feasibility of C-C bonds in three hybridized states: sp^1, sp^2 and sp^3. In sp^3 configuration, as in diamond, each of a carbon atom's four valance electrons is assigned to a tetrahedrally directed sp^3 hybrid orbital, which makes a strong σ bonds with an electron of adjacent atom. In sp^2 configuration, as in graphite, three of the four valance electrons are assigned to trigonally directed sp^2 hybrid orbitals which form strong intra-layer σ bonds. The fourth electron lies in a p_z orbital, which is in a direction normal to the σ bonding plane. This p_z orbitals form weak π bonds with neighboring p_z orbitals. Whereas, in sp^1 configuration, as in acetylene, two valance electrons are assigned to linearly directed sp^1 hybrid orbitals which form σ bonds and other two electrons are placed one each in the p_y and p_z orbitals to form π bonds [3-6]. The properties of different allotropes of carbon are strongly dependent on the ratio of different hybridized states of carbon atoms and are listed in table 1.1. This chapter presents the introductory idea about different allotropes of carbon such as diamond like carbon, carbon nanoflakes, graphene and graphene oxide and its properties, applications and history of the development. This chapter also contains the motivation behind the present work followed by outline of the thesis.

1.1 Different allotropes of carbon: properties, applications and history of development

1.1.1 Diamond like carbon

Diamond like carbon is a stable form of amorphous carbon (a-C), bonded with sp^2 and sp^3 hybridized states of carbon, containing less than or equal to 40% sp^3 bonded carbon atoms. The term DLC is also used to designate the hydrogenated form of a-C (a-C:H). Films with high sp^3 content (≥ 85%) are called tetrahedral amorphous carbon film [3, 4, 7, 8], whereas in case of diamond, all the carbon atoms are covalently bonded in sp^3 configuration. Diamond is the hardest known material on the earth and it has several peculiar properties such as high mechanical hardness (~ 100 GPa) [7, 9], high thermal conductivity (~ 2000 W/m-K) [10, 11], very low coefficient of friction [12], etc. After a few years of diamond growth, another form of carbon known as diamond like carbon (also the family of nano-crystalline diamond) came into the picture due to its easier growth as compared to single crystal diamond as well as having similar properties as that of diamond. The comparative study of the properties of DLC and diamond are listed in table 1.1. DLC is a low mobility semiconductor having wide band gap of 1 – 4 eV [7, 8]. It has high mechanical hardness (40 – 80 GPa) [13], excellent thermal conductivity, smallest thermal expansion coefficient and is chemically inert. These properties of DLC films have a wide range of applications in electronics and mechanical systems such as protective coating on optical windows, cutting tools, surgical tools, magnetic storage disc to protect the head crash, etc. Due to high thermal conductivity, it can be used as heat sink to increase the packing density of large scale multiple chips in electronic devices.

DLC films were deposited for the first time in early 1970s by Aisenberg et al. [14] by carbon ions sputtered from carbon electrodes using direct ion beam deposition (IBD) method. However, this method had a low deposition rate of 1 µm/h and was suitable for laboratory use only. In 1978, Holland et al. [15] reported the deposition of hard amorphous carbon films by CH_4/Ar precursor gases using rf-PECVD technique. In 1982, Matsumoto et al. [16] made a breakthrough in CVD diamond technology using hot filament CVD method, where hydrocarbon gases are directly activated while passing through hot filament of ~ 2000 ^{o}C and lead to a high growth rate of ~ 1 mm/h.

Table 1.1: Properties of different form of carbon allotropes [3, 7, 8, 17-22].

	Diamond (Cubic)	**ta-C (amorphous)**	**DLC (amorphous)**	**Graphite (Hexagonal)**	**Graphene (Hexagonal)**
Mass density (g/cm^3)	3.51	2.4	1.2-2.2	2.26	1.5-2.0
Sp^3 content (%)	100	70-80	≤ 60	0	0
Sp^2 content (%)	0	10-20	≤ 40	100	100
Hydrogen content (at. %)	0	~ 1	10-50	0	0
Band gap (eV)	5.5	2-2.5	1.1-4	0.04	0
Friction coefficient	0.1	0.6	0.02-0.2	≥ 0.6	
Electrical resistivity (Ω cm)	$> 10^{16}$	10^{10}-10^{6}	10^{7}-10^{4}	10^{-6}	$\sim 10^{-6}$
Thermal conductivity (W/m-K)	2000	< 2000		25-470	3080-5000

In the late 1985, synthesis of diamond under low pressure by DC plasma jet attracted many researchers and industries owing to its high growth rate [23]. However, apparatus of the DC-plasma jet is highly expensive. Since then, various CVD methods such as rf-plasma CVD [24], microwave plasma CVD [25], HFCVD [26, 27] as well as other physical vapor deposition methods such as sputtering [28] and pulsed laser deposition [29] and their modifications have been developed for the deposition of DLC thin films. Therefore, with the development of deposition techniques, now a days, chemical vapor deposition is considered as the most important method for the growth of DLC as well as diamond in both the level of research and industry [6]. Among various CVD methods, HFCVD has more advantage over other plasma CVD due to ability of large area deposition, high growth rate and reduced defects concentration due to the absence of bombardment of high energetic ions during deposition on growing surface of the films.

In the development of growth of high density sp^3 bonded diamond like carbon films, in the early days of 1980s, diamond single crystals were used as substrates [30]. In 1982, Matsumoto et al. [16] made a breakthrough in growing diamond films on non-diamond substrates. However, apart from very low nucleation density of diamond / DLC in the range of 10^4 – 10^6/cm^2, continuous films could not be formed [16, 31]. Numerous approaches have been used to enhance the nucleation density such as substrate abrasion with diamond powder [32], addition of carbide formation [33, 34], substrate biasing [35-37], etc. It was found that abrasion of the substrate surface with diamond powder could greatly enhance the nucleation density in the range of 10^7 – 10^8/cm^2 [6]. Besides diamond powder, other abrasive powder such as c-BN, SiC, etc. can be used to scratch the substrate surface to enhance the nucleation density [6]. Yugo et al. [38] reported bias-enhanced nucleation method and obtained high density of nucleation in the range of 10^9 – 10^{10}/cm^2 on a mirror-polished Si substrates using microwave CVD (MWCVD). Subsequent developments of bias enhanced nucleation by Chang et al. [37] and Stoner et al. [35] have led to the growth of diamond on silicon and silicon carbide substrates respectively. So far maximum nucleation density ~ 10^{11} – 10^{12}/cm^2 have been reported on carbon affinity substrates [39-42]. Nucleation density was calculated by simply counting the number of diamond particles in a given area. This is adequate when the density lies below 10^{10}/cm^2. However, as the nucleation density exceeds 10^{11}/cm^2, it becomes impossible to resolve individual nucleation sites and it is in the order of 10^{12}/cm^2 for 10 nm particles with no space between them or 5 nm dimension of the particles with 5 nm spacing [41].

1.1.2 Carbon nanoflakes

Carbon nanoflakes, also known as carbon nanowalls (CNW), are a type of two dimensional vertically aligned carbon nanostructures like carbon nanotube (1D), carbon nanofiber (1D), as shown in figure 1.1.

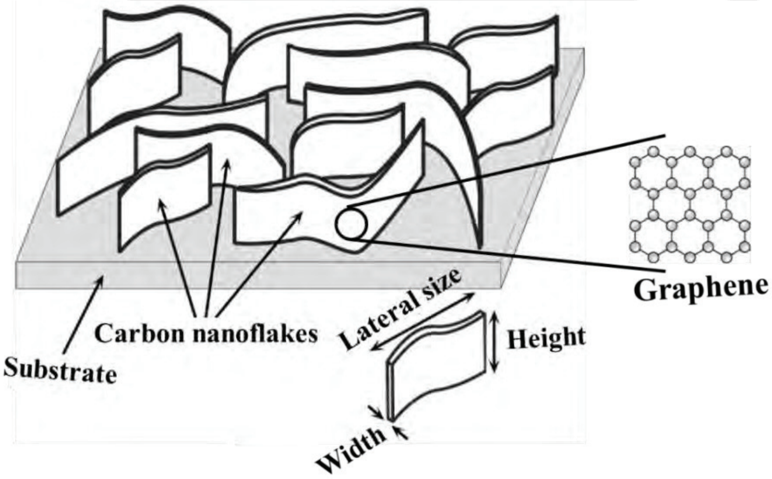

Figure 1.1: *Schematic of vertically aligned carbon nanoflakes* [43].

It has wall structure which consists of multi-layers graphene with an individual sheet thickness of several to ten nanometers [44]. It has large surface area (300 – 700 m^2/g) [45] and large surface to volume ratio. Due to large surface area with high aspect ratio, carbon nanoflakes could be an ideal material for catalytic support and also allow for the developing of effective field emission cathode for vacuum electronic devices.

Furthermore, since CNF is essentially consists of multi-layers graphene sheets, it is expected to have high carrier mobility and high sustainable current density [46, 47]. Due to large surface area and high carrier mobility, it is also expected to be promising material for current collector electrodes [48] in different electronic devices.

Carbon nanoflakes were accidently discovered in 2002 by Wu et al. [49] during the growth of carbon nanotubes using microwave PECVD. Now a days, several methods have been developed for the preparation of carbon nanoflakes such as DC-PECVD [50], radio frequency capacitively / inductively coupled PECVD [51, 52], microwave PECVD [53], HFCVD [54], etc. In recent years, PECVD is much popular method for the uniform growth of vertically aligned carbon nanoflakes. However, HFCVD is more efficient for the growth of comparatively denser flakes on larger area in comparison to other fabrication systems. Moreover, the additional advantage of feasibility to use high hydrogen radical density in HFCVD method, which involves in the removal of undesirable amorphous carbon during growth and therefore leading to improve surface morphology and crystalline quality of the CNF thin films. HFCVD method is used to prepare carbon nanoflakes first time in 2002 by Shang et al. [55]. In recent years, several studies have been done on the growth of CNF with/without catalyst on different substrates. Shiji et al. [56] have prepared CNF on Si substrates without catalyst using different fluorocarbon / hydrocarbon source gases C_2F_6, CF_4, CH_4, etc. by capacitively coupled rf-PECVD. Kurita et al. [43] have prepared CNF using Ni and Cr catalyst on quartz substrates using $CH_4/H_2/Ar$ gas mixture by rf-PECVD. After the detail study of growth parameters which is reported in literature, we have observed that structural properties of CNF were studied by varying substrate temperature (T_S) [43, 55, 57, 58], filament temperature [58, 59] and concentration of different hydrocarbon / fluorocarbon gases [54, 60, 61]. Whereas, effect of process pressure on the structural properties of CNF have been rarely studied. Shimabukuro et al. [58] have reported the structural properties of CNF on stainless steel (SS) substrates at different substrate temperatures of 400 – 600 °C and at different filament temperatures of 1850 – 2150 °C. The effect of different concentrations of hydrocarbon gases (C_2H_2, CH_4) on the structural properties of CNF is reported by Teii et al. [60]. In the continuation of growth of carbon nanoflakes at different substrates, CNF are mostly grown on semiconductor / metallic substrates such as Si, Ni, Cu and SS [43, 55, 57, 62, 63], whereas only a few reports are available in literature for the growth of CNF on glass substrate [64, 65].

1.1.3 Single and Multi – layers Graphene

Graphene is one atom thick planar sheet of purely (100%) sp^2 bonded carbon atoms tightly packed into two dimensional honeycomb structure made out of hexagons. It is considered to be basic building block of other carbon allotropes such as graphite, CNT, fullerene, etc. The honeycomb structure of single layer graphene is shown in figure 1.2. In single layer graphene, the arrangement of lattice can be seen as consisting of two interpenetrated triangular sub-lattices in a manner that atoms of one sub-lattice are at the center of the triangles joined by the other sub-lattice with a carbon to carbon interatomic distance, a_{c-c} of 1.42 Å [2, 66]. The unit cell comprises two carbon atoms and is invariant under a rotation of 120° around any atom. Multi-layers graphene can be formed through stacking of a few layer of graphene with an interplanar spacing of 3.35 Å, as shown in figure 1.3. These layers could be stacked along c-axis in alternating sequence of --ABAB-- (Bernal type) or --ABCABC-- (rhombohedral type) which are bonded by weak van der Waals forces [67, 68]. Graphene has attracted a worldwide attention of researchers and technologist due to its unique transport properties which make it promising material for the applications in next generation electronic devices. It has high carrier mobility (~ 1000-15000 cm^2/V-s) [68-70], high current carrying capacity (~ 10^8 A/cm^2) [71], large specific surface area (~2600 m^2/g) [72] and high optical transparency in Vis-NIR region [22]. Due to these peculiar properties of graphene, it can be used in transistors [73], transparent electrodes [74, 75], supercapacitors [76], etc.

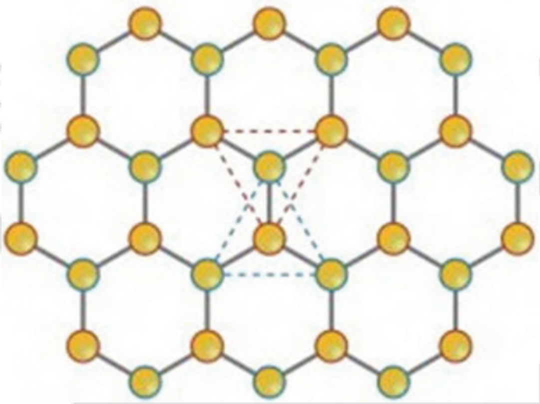

Figure 1.2: *Honeycomb structure of single layer graphene* [2].

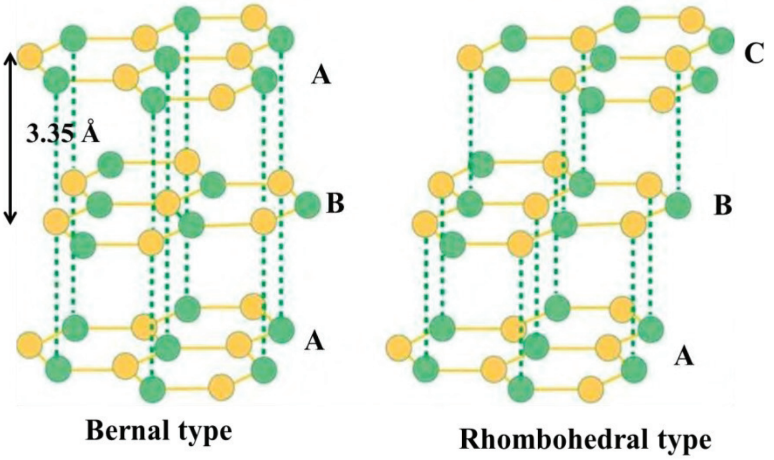

Figure 1.3: *Structure of multi-layers graphene: Bernal type (left) and Rhombohedral type (right)* [67].

In the development of single layer graphene, it was first prepared in 2004 by mechanical cleavage from highly ordered pyrolytic graphite (HOPG) [69]. In this procedure, a layer is peeled off from the HOPG crystal using scotch tape and then transferred to different substrates. But, this method can only produce small area films of the order of a few tens of micrometers and is not scalable. After the investigation of single layer graphene, several preparation methods have been developed to enhance the area of graphene such as chemical cleavage method [77], thermal desorption of Si from SiC [78, 79] and chemical vapor deposition (CVD) [80-83]. In chemical cleavage method, exfoliation of graphite oxide layers can produce reduced graphene oxide by reduction of oxygen which is bonded with carbon atoms. But, electrical properties of reduced graphene oxide films are inferior to that of exfoliated natural graphite [84]. This is possible due to a combination of factors such as damage of graphene lattice during the formation of graphite oxide (by chemical reaction, ultracentrifugation) and creation of defects (pores) during the reduction of graphite oxide. In thermal desorption of Si, single layer graphene films are produced on the Si- terminated (0001) face of single crystal 6H-SiC [85]. In this method, SiC substrates are subjected to heat in the temperature range of 1200 to 1500 °C for 1 – 20 min under high vacuum [86, 87], whereas furnace CVD method involves the decomposition of hydrocarbon gases such as CH_4, C_2H_2, etc. at high temperature of 1000 – 1200 °C [80, 81, 88]. In spite of many methods for the preparation of graphene, the most challenging task is to produce high quality graphene with large area (μm to mm dimension). In recent years, for the development of high quality graphene, CVD methods are much popular method for the growth of graphene in large area. Graphene is deposited by quartz tube furnace CVD at T_S of approximately 1000 °C [80, 81, 89] and also at low T_S of 700 – 800 °C using plasma CVD [83, 90] on various transition metals Co, Cu, Ni, etc. which acts as catalysts for the growth of graphene films. Several transition metals that have been used successfully for the growth of graphene films are Co [91], Pt [92, 93], Ir [94], Ru [95], Cu [84, 96] and Ni [80, 81]. Among these transition metals, Ni substrate is very popular for the growth of graphene.

Since in case of Ni, the in-plane lattice constant of (111) plane is 0.232 nm, as compared to graphite (for which in-plane lattice constant is 0.246 nm) [66, 97-99]. This lattice match is sufficient to allow continuous growth of graphene films on the surface of Ni. In the continuation of quality of the graphene, films deposited at low T_S of 450 – 600 ^oC have lot of defects in comparison to those deposited at high temperature [82, 83, 90, 100]. Since for the application of graphene in different fields, it is necessary to fabricate over large area. In recent years, relatively new method, known as HFCVD, is developed for the growth of graphene in large area. Only a few reports are available in literature on the growth of graphene using HFCVD at T_S of 800 – 900 ^oC, having 4 to 10 number of graphene layers with large defects [88, 101, 102] and no results are reported about the high quality single layer graphene using HFCVD method.

1.1.4 Graphene oxide and reduced graphene oxide

Graphene oxide (GO) consists of graphene with various oxygen functional groups such as epoxide (C-O-C), hydroxyl (C-OH), carbonyl (C=O) and carboxyl (-COOH) groups at the basal plane and at the edges of graphene [103], as shown in figure 1.4, resulting in a hybrid structure comprising a mixture of sp^2 and sp^3 hybridized carbon atoms bonded with oxygen containing functional groups [104-107]. The oxygen functionalities of GO films can be reduced to obtain graphene like sheets (also known as reduced graphene oxide (rGO)). It has attracted much interest in research due to cost-effective and high volume manufacturing of reduced GO. From the reduction of GO, one can control the electrical properties from insulating to semi metallic behavior as well as band gap of GO by controlling the fraction of sp^2 and sp^3 bonded carbon with oxygen containing functional groups [108, 109]. It is therefore, being proposed and developed for making large area conductive coating and other technological applications in many field such as energy storage devices [110, 111], electrodes in dye-sensitized solar cells [112], gas sensor [113], chemical and biological sensors [105, 114], etc.

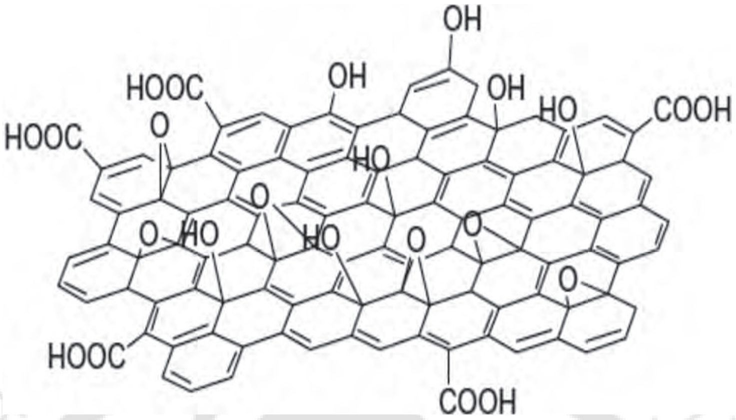

Figure 1.4: *Structure of graphene oxide (GO) functionalized with different oxygen containing functional groups* [104].

There are several different methods such as chemical reduction [115, 116], thermal reduction [106, 117], plasma reduction [103], etc. for the reduction of oxygen containing functional groups from graphene oxide for the preparation of graphene like (rGO) thin films. Among these methods, chemical reduction is very simple. But from this method, the prepared graphene like (rGO) films exhibit a relatively low C:O ratio and resulting in highly resistive films [118-120]. Also, most of the reducing regent used for the reduction of GO are highly toxic in nature. On the other hand, thermal reduction is highly effective in producing graphene like films with a relatively high C:O ratio in comparison to chemical routes. However, this approach has disadvantage of choice of substrates, i.e. this method is not suitable for the substrates with low glass transition temperature [118].

Thus, due to feasibility of different type of carbon bonds existing in nature, the physical properties of different bonding structures are different. Therefore, it is important to study the properties of carbon nanomaterials with different fraction of sp^2 and sp^3 hybridized carbon bonded atoms for the application in different field of optics, electronics, mechanical system, etc.

1.2 Motivation

Though, several studies have been done in the field of diamond like carbon for the enhancement of nucleation density of sp^3 bonded carbon atoms on carbon affinity substrates, however, the most challenging task is to prepare high density sp^3 bonded carbon on non-carbon affinity substrates. Therefore, our motivation is to deposit high density sp^3 bonded carbon on non-carbon affinity substrates without any surface pre-treatment, which is important for the applications in several fields such as to increase the hardness of different mechanical and surgical tools, etc. Furthermore, since HFCVD is a new method for the growth of large area graphene films and it is still in progress. Therefore, our motivation is to fabricate large area single and multi-layers graphene thin films by HFCVD method. The advantage of HFCVD method is that hydrocarbon gases are dissociated at high filament temperature (1800 – 2200 ^{o}C) and therefore it is possible to deposit high quality films at relatively low substrate temperature in comparison to other CVD process. Therefore, keeping all aspects in our mind, present thesis work is focused on the study of influence of deposition parameters on the growth of diamond like carbon, carbon nanoflakes, single and multi-layers graphene and graphene oxide thin films as well as study of its structural, optical and electrical properties.

1.3 Contents of Thesis chapters

The present thesis consists of eight chapters. Chapter 1 is introduction, where a brief introductory idea about the different form of carbon allotropes along with literature review and motivation behind the present thesis work is given. Chapter 2 is on experimental details, which gives a quick description of HFCVD system, which is used for the preparation of thin films of different carbon nanomaterials. This chapter also contains the brief description of different characterization techniques used to study the different properties of the films.

Chapter 3 is on the preparation and study of structural properties of DLC thin films on two different substrates: Si and ITO coated glass substrates and the influence of different concentration of precursor gases using HFCVD method.

Chapter 4 presents the study of influence of different deposition parameters such as process pressure and substrate temperature on the growth of CNF thin films using HFCVD method. This chapter also contains the study of structural, optical (linar/nonlinear) and electrical properties of the as deposited carbon nanoflakes.

Chapter 5 presents a systematic study on the influence of different deposition parameters such as substrate temperature, process pressure, precursor gas flow rate and deposition time for the fabrication of high quality single and multi-layers graphene films by HFCVD method. This chapter also contains about the structural, optical (linear/nonlinear) and electrical properties of single and multi-layers graphene films.

Chapter 6 contains the study of chemically derived graphene oxide thin films and followed by thermal reduction of garphene oxide at different temperature. Structural, optical (linear) and electrical properties of graphene oxide / thermally reduced graphene oxide are discussed in details.

Chapter 7 is on the study of transport properties of charge carriers in graphene using graphene channel field effect transistor.

Chapter 8 is the final chapter of the thesis, which gives the final conclusion based on the work reported in the present thesis. This chapter also presents the scope of future work from the present thesis work.

1.5 References

[1] A.K. Geim, K.S. Novoselov, The rise of graphene, Nature Materials, 6 (2007) 183-191.

[2] C. Soldano, A. Mahmood, E. Dujardin, Production, properties and potential of graphene, Carbon, 48 (2010) 2127-2150.

[3] J. Robertson, Diamond-like amorphous carbon, Materials Science and Engineering: R: Reports, 37 (2002) 129-281.

[4] J. Robertson, Diamond-like carbon, Pure and Applied Chemistry, 66 (1994) 1789-1796.

[5] A.C. Ferrari, J. Robertson, Raman spectroscopy of amorphous, nanostructured, diamond–like carbon, and nanodiamond, Phil. Trans. R. Soc. Lond. A, 362 (2004) 2477-2512.

[6] S.T. Lee, Z. Lin, X. Jiang, CVD diamond films: nucleation and growth, Materials Science and Engineering: R: Reports, 25 (1999) 123-154.

[7] J. Robertson, Properties of diamond-like carbon, Surface and Coatings Technology, 50 (1992) 185-203.

[8] A. Grill, Diamond-like carbon: state of the art, Diamond and Related Materials, 8 (1999) 428-434.

[9] J.J. Gracio, Q.H. Fan, J.C. Madaleno, Diamond growth by chemical vapour deposition, Journal of Physics D: Applied Physics, 43 (2010) 374017.

[10] W.B. Yang, F.X. Lü, Z.X. Cao, Growth of nanocrystalline diamond protective coatings on quartz glass, Journal of Applied Physics, 91 (2002) 10068-10073.

[11] S.E. Coe, R.S. Sussmann, Optical, thermal and mechanical properties of CVD diamond, Diamond and Related Materials, 9 (2000) 1726-1729.

[12] M. Goto, F. Honda, M. Uemura, Extremely low coefficient of friction of diamond sliding against Ag thin films on Si(1 1 1) surface under ultrahigh vacuum condition, Wear, 252 (2002) 777-786.

[13] B. Schultrich, H.J. Scheibe, D. Drescher, H. Ziegele, Deposition of superhard amorphous carbon films by pulsed vacuum arc deposition, Surface and Coatings Technology, 98 (1998) 1097-1101.

[14] S. Aisenberg, R. Chabot, Ion-Beam Deposition of Thin Films of Diamondlike Carbon, Journal of Applied Physics, 42 (1971) 2953-2958.

[15] L. Holland, S.M. Ojha, Deposition of hard and insulating carbonaceous films on an r.f. target in a butane plasma, Thin Solid Films, 38 (1976) L17-L19.

[16] S. Matsumoto, Y. Sato, M. Tsutsumi, N. Setaka, Growth of diamond particles from methane-hydrogen gas, J Mater Sci, 17 (1982) 3106-3112.

[17] K. Bewilogua, D. Hofmann, History of diamond-like carbon films — From first experiments to worldwide applications, Surface and Coatings Technology, 242 (2014) 214-225.

[18] A.A. Balandin, S. Ghosh, W. Bao, I. Calizo, D. Teweldebrhan, F. Miao, C.N. Lau, Superior Thermal Conductivity of Single-Layer Graphene, Nano Letters, 8 (2008) 902-907.

[19] J. Robertson, Comparison of diamond-like carbon to diamond for applications, physica status solidi (a), 205 (2008) 2233-2244.

[20] K. Enke, H. Dimigen, H. Hübsch, Frictional properties of diamondlike carbon layers, Applied Physics Letters, 36 (1980) 291-292.

[21] J. Robertson, Hard amorphous (diamond-like) carbons, Progress in Solid State Chemistry, 21 (1991) 199-333.

[22] Ö.D. Coşkun, T. Zerrin, Optical, structural and bonding properties of diamond-like amorphous carbon films deposited by DC magnetron sputtering, Diamond and Related Materials, 56 (2015) 29-35.

[23] K. Kurihara, K. Sasaki, M. Kawarada, N. Koshino, High rate synthesis of diamond by dc plasma jet chemical vapor deposition, Applied Physics Letters, 52 (1988) 437-438.

[24] G.A.J. Amaratunga, S.R.P. Silva, D.R. McKenzie, Influence of dc bias voltage on the refractive index and stress of carbon-diamond films deposited from a CH_4/Ar rf plasma, Journal of Applied Physics, 70 (1991) 5374-5379.

[25] S. Sahoo, S.S. Pradhan, V. Bhavanasi, S.K. Pradhan, Structural and mechanical characterization of diamond like carbon films grown by microwave plasma CVD, Surface and Coatings Technology, 204 (2010) 2817-2821.

[26] M. Amaral, A.J.S. Fernandes, M. Vila, F.J. Oliveira, R.F. Silva, Growth rate improvements in the hot-filament CVD deposition of nanocrystalline diamond, Diamond and Related Materials, 15 (2006) 1822-1827.

[27] P.W. May, J.A. Smith, Y.A. Mankelevich, Deposition of NCD films using hot filament CVD and $Ar/CH_4/H_2$ gas mixtures, Diamond and Related Materials, 15 (2006) 345-352.

[28] M. Rybachuk, J.M. Bell, Growth of diamond-like carbon films using low energy ion beam sputter - bombardment deposition with Ar ions, Journal of Physics: Conference Series, 100 (2008) 082009.

[29] Y.K. Hong, J.-J. Kim, C. Park, J.S. Kim, J.K. Kim, Field electron emission of diamondlike carbon films deposited by a laser ablation method, Journal of Vacuum Science and Technology B, 16 (1998) 729-731.

[30] B.V. Spitsyn, L.L. Bouilov, B.V. Derjaguin, Vapor growth of diamond on diamond and other surfaces, Journal of Crystal Growth, 52 (1981) 219-226.

[31] W.S. Yang, J.H. Je, Effects of secondary pretreatments of substrate on the nucleation of diamond film, Journal of Materials Research, 11 (1996) 1787-1794.

[32] J.E. Gerbi, J. Birrell, M. Sardela, J.A. Carlisle, Macrotexture and growth chemistry in ultrananocrystalline diamond thin films, Thin Solid Films, 473 (2005) 41-48.

[33] Y. Mitsuda, Y. Kojima, T. Yoshida, K. Akashi, The growth of diamond in microwave plasma under low pressure, J Mater Sci, 22 (1987) 1557-1562.

[34] L.C. Nistor, J. Van Landuyt, V.G. Ralchenko, E.D. Obraztsova, A.A. Smolin, Nanocrystalline diamond films: transmission electron microscopy and Raman spectroscopy characterization, Diamond and Related Materials, 6 (1997) 159-168.

[35] B.R. Stoner, J.T. Glass, Textured diamond growth on (100) β-SiC via microwave plasma chemical vapor deposition, Applied Physics Letters, 60 (1992) 698-700.

[36] C.-H. Liang, C.-F. Huang, H.-Y. Tsai, The influence of substrate bias voltages on structure, mechanical properties and anti-corrosion performance of Cr doped diamond-like carbon films deposited by steered cathodic arc evaporation, Thin Solid Films, (doi: 10.1016/j.tsf.2015.11.010) Article in press.

[37] T.-F. Chang, L. Chang, Highly oriented diamond growth on positively biased Si substrates, Journal of Materials Research, 16 (2001) 3351-3354.

[38] S. Yugo, T. Kanai, T. Kimura, T. Muto, Generation of diamond nuclei by electric field in plasma chemical vapor deposition, Applied Physics Letters, 58 (1991) 1036-1038.

[39] T. Hao, H. Zhang, C. Shi, G. Han, Nano-crystalline diamond films synthesized at low temperature and low pressure by hot filament chemical vapor deposition, Surface and Coatings Technology, 201 (2006) 801-806.

[40] H. Liu, D.S. Dandy, Studies on nucleation process in diamond CVD: an overview of recent developments, Diamond and Related Materials, 4 (1995) 1173-1188.

[41] O.A. Williams, Nanocrystalline diamond, Diamond and Related Materials, 20 (2011) 621-640.

[42] S. Iijima, Y. Aikawa, K. Baba, Growth of diamond particles in chemical vapor deposition, Journal of Materials Research, 6 (1991) 1491-1497.

[43] S. Kurita, A. Yoshimura, H. Kawamoto, T. Uchida, K. Kojima, M. Tachibana, P. Molina-Morales, H. Nakai, Raman spectra of carbon nanowalls grown by plasma-enhanced chemical vapor deposition, Journal of Applied Physics, 97 (2005) 104320.

[44] Z. Bo, K. Yu, G. Lu, P. Wang, S. Mao, J. Chen, Understanding growth of carbon nanowalls at atmospheric pressure using normal glow discharge plasma-enhanced chemical vapor deposition, Carbon, 49 (2011) 1849-1858.

[45] T.-C. Hung, C.-F. Chen, C.-C. Chen, W.-T. Whang, Catalyst-free, low-temperature growth of high-surface area carbon nanoflakes on carbon cloth, Applied Surface Science, 255 (2009) 3676-3681.

[46] L. Cui, J. Chen, B. Yang, D. Sun, T. Jiao, RF-PECVD synthesis of carbon nanowalls and their field emission properties, Applied Surface Science, 357, Part A (2015) 1-7.

[47] H.J. Cho, H. Kondo, K. Ishikawa, M. Sekine, M. Hiramatsu, M. Hori, Density control of carbon nanowalls grown by CH_4/H_2 plasma and their electrical properties, Carbon, 68 (2014) 380-388.

[48] V.A. Krivchenko, D.M. Itkis, S.A. Evlashin, D.A. Semenenko, E.A. Goodilin, A.T. Rakhimov, A.S. Stepanov, N.V. Suetin, A.A. Pilevsky, P.V. Voronin, Carbon nanowalls decorated with silicon for lithium-ion batteries, Carbon, 50 (2012) 1438-1442.

[49] Y. Wu, P. Qiao, T. Chong, Z. Shen, Carbon Nanowalls Grown by Microwave Plasma Enhanced Chemical Vapor Deposition, Advanced Materials, 14 (2002) 64-67.

[50] A. Yoshimura, S. Kurita, M. Tachibana, K. Kojima, P. Molina-Morales, H. Nakai, Fabrication of carbon nanowalls by dc plasma-enhanced chemical vapor deposition and characterization of their structures, in: Nanotechnology, 2005. 5th IEEE Conference on, 2005, pp. 482-485 vol. 482.

[51] M. Hiramatsu, K. Shiji, H. Amano, M. Hori, Fabrication of vertically aligned carbon nanowalls using capacitively coupled plasma-enhanced chemical vapor deposition assisted by hydrogen radical injection, Applied Physics Letters, 84 (2004) 4708-4710.

[52] J. Wang, M. Zhu, R.A. Outlaw, X. Zhao, D.M. Manos, B.C. Holloway, Synthesis of carbon nanosheets by inductively coupled radio-frequency plasma enhanced chemical vapor deposition, Carbon, 42 (2004) 2867-2872.

[53] A.T.H. Chuang, B.O. Boskovic, J. Robertson, Freestanding carbon nanowalls by microwave plasma-enhanced chemical vapour deposition, Diamond and Related Materials, 15 (2006) 1103-1106.

[54] S. Shimabukuro, Y. Hatakeyama, M. Takeuchi, T. Itoh, S. Nonomura, Effect of hydrogen dilution in preparation of carbon nanowall by hot-wire CVD, Thin Solid Films, 516 (2008) 710-713.

[55] N.G. Shang, F.C.K. Au, X.M. Meng, C.S. Lee, I. Bello, S.T. Lee, Uniform carbon nanoflake films and their field emissions, Chemical Physics Letters, 358 (2002) 187-191.

[56] K. Shiji, M. Hiramatsu, A. Enomoto, M. Nakamura, H. Amano, M. Hori, Vertical growth of carbon nanowalls using rf plasma-enhanced chemical vapor deposition, Diamond and Related Materials, 14 (2005) 831-834.

[57] K. Davami, M. Shaygan, N. Kheirabi, J. Zhao, D.A. Kovalenko, M.H. Rümmeli, J. Opitz, G. Cuniberti, J.-S. Lee, M. Meyyappan, Synthesis and characterization of carbon nanowalls on different substrates by radio frequency plasma enhanced chemical vapor deposition, Carbon, 72 (2014) 372-380.

[58] S. Shimabukuro, Y. Hatakeyama, M. Takeuchi, T. Itoh, S. Nonomura, Preparation of Carbon Nanowall by Hot-Wire Chemical Vapor Deposition and Effects of Substrate Heating Temperature and Filament Temperature, Japanese Journal of Applied Physics, 47 (2008) 8635.

[59] T. Itoh, Synthesis of carbon nanowalls by hot-wire chemical vapor deposition, Thin Solid Films, 519 (2011) 4589-4593.

[60] K. Teii, S. Shimada, M. Nakashima, A.T.H. Chuang, Synthesis and electrical characterization of n-type carbon nanowalls, Journal of Applied Physics, 106 (2009) 084303.

[61] H.G. Jain, H. Karacuban, D. Krix, H.-W. Becker, H. Nienhaus, V. Buck, Carbon nanowalls deposited by inductively coupled plasma enhanced chemical vapor deposition using aluminum acetylacetonate as precursor, Carbon, 49 (2011) 4987-4995.

[62] J.J. Wang, M.Y. Zhu, R.A. Outlaw, X. Zhao, D.M. Manos, B.C. Holloway, V.P. Mammana, Free-standing subnanometer graphite sheets, Applied Physics Letters, 85 (2004) 1265-1267.

[63] V.A. Krivchenko, V.V. Dvorkin, N.N. Dzbanovsky, M.A. Timofeyev, A.S. Stepanov, A.T. Rakhimov, N.V. Suetin, O.Y. Vilkov, L.V. Yashina, Evolution of carbon film structure during its catalyst-free growth in the plasma of direct current glow discharge, Carbon, 50 (2012) 1477-1487.

[64] T. Itoh, Y. Nakanishi, T. Ito, A. Vetushka, M. Ledinský, A. Fejfar, J. Kočka, S. Nonomura, Electrical properties of carbon nanowall films, Journal of Non-Crystalline Solids, 358 (2012) 2548-2551.

[65] K. Sung Yun, J. Yeun Ho, C. Won Seok, Growth properties of carbon nanowalls on glass substrates by a microwave plasma-enhanced chemical vapor deposition, Japanese Journal of Applied Physics, 53 (2014) 05FD09.

[66] L.M. Malard, M.A. Pimenta, G. Dresselhaus, M.S. Dresselhaus, Raman spectroscopy in graphene, Physics Reports, 473 (2009) 51-87.

[67] C.H. Lui, Z. Li, K.F. Mak, E. Cappelluti, T.F. Heinz, Observation of an electrically tunable band gap in trilayer graphene, Nature Physics, 7 (2011) 944-947.

[68] A.H. Castro Neto, F. Guinea, N.M.R. Peres, K.S. Novoselov, A.K. Geim, The electronic properties of graphene, Reviews of Modern Physics, 81 (2009) 109-162.

[69] K.S. Novoselov, A.K. Geim, S.V. Morozov, D. Jiang, Y. Zhang, S.V. Dubonos, I.V. Grigorieva, A.A. Firsov, Electric Field Effect in Atomically Thin Carbon Films, Science, 306 (2004) 666-669.

[70] A. Reina, X. Jia, J. Ho, D. Nezich, H. Son, V. Bulovic, M.S. Dresselhaus, J. Kong, Large Area, Few-Layer Graphene Films on Arbitrary Substrates by Chemical Vapor Deposition, Nano Letters, 9 (2009) 30-35.

[71] J. Moser, A. Barreiro, A. Bachtold, Current-induced cleaning of graphene, Applied Physics Letters, 91 (2007) 163513.

[72] C.N.R. Rao, A.K. Sood, K.S. Subrahmanyam, A. Govindaraj, Graphene: The New Two-Dimensional Nanomaterial, Angewandte Chemie International Edition, 48 (2009) 7752-7777.

[73] T.J. Echtermeyer, M.C. Lemme, M. Baus, B.N. Szafranek, A.K. Geim, H. Kurz, Nonvolatile Switching in Graphene Field-Effect Devices, Electron Device Letters, IEEE, 29 (2008) 952-954.

[74] X. Wang, L. Zhi, K. Müllen, Transparent, Conductive Graphene Electrodes for Dye-Sensitized Solar Cells, Nano Letters, 8 (2008) 323-327.

[75] G. Eda, G. Fanchini, M. Chhowalla, Large-area ultrathin films of reduced graphene oxide as a transparent and flexible electronic material, Nature Nanotechnology, 3 (2008) 270-274.

[76] M.D. Stoller, S. Park, Y. Zhu, J. An, R.S. Ruoff, Graphene-Based Ultracapacitors, Nano Letters, 8 (2008) 3498-3502.

[77] K.N. Kudin, B. Ozbas, H.C. Schniepp, R.K. Prud'homme, I.A. Aksay, R. Car, Raman Spectra of Graphite Oxide and Functionalized Graphene Sheets, Nano Letters, 8 (2008) 36-41.

[78] C. Faugeras, A. Nerrière, M. Potemski, A. Mahmood, E. Dujardin, C. Berger, W.A. de Heer, Few-layer graphene on SiC, pyrolitic graphite, and graphene: A Raman scattering study, Applied Physics Letters, 92 (2008) 011914.

[79] S.N. Yannopoulos, A. Siokou, N.K. Nasikas, V. Dracopoulos, F. Ravani, G.N. Papatheodorou, CO_2-Laser-Induced Growth of Epitaxial Graphene on 6H-SiC(0001), Advanced Functional Materials, 22 (2012) 113-120.

[80] L. Huang, Q.H. Chang, G.L. Guo, Y. Liu, Y.Q. Xie, T. Wang, B. Ling, H.F. Yang, Synthesis of high-quality graphene films on nickel foils by rapid thermal chemical vapor deposition, Carbon, 50 (2012) 551-556.

[81] H.J. Park, J. Meyer, S. Roth, V. Skákalová, Growth and properties of few-layer graphene prepared by chemical vapor deposition, Carbon, 48 (2010) 1088-1094.

[82] T.-o. Terasawa, K. Saiki, Growth of graphene on Cu by plasma enhanced chemical vapor deposition, Carbon, 50 (2012) 869-874.

[83] Y. Kim, W. Song, S.Y. Lee, C. Jeon, W. Jung, M. Kim, C.-Y. Park, Low-temperature synthesis of graphene on nickel foil by microwave plasma chemical vapor deposition, Applied Physics Letters, 98 (2011) 263106.

[84] X. Li, Y. Zhu, W. Cai, M. Borysiak, B. Han, D. Chen, R.D. Piner, L. Colombo, R.S. Ruoff, Transfer of Large-Area Graphene Films for High-Performance Transparent Conductive Electrodes, Nano Letters, 9 (2009) 4359-4363.

[85] E. Rollings, G.H. Gweon, S.Y. Zhou, B.S. Mun, J.L. McChesney, B.S. Hussain, A.V. Fedorov, P.N. First, W.A. de Heer, A. Lanzara, Synthesis and characterization of atomically thin graphite films on a silicon carbide substrate, Journal of Physics and Chemistry of Solids, 67 (2006) 2172-2177.

[86] C. Berger, Z. Song, T. Li, X. Li, A.Y. Ogbazghi, R. Feng, Z. Dai, A.N. Marchenkov, E.H. Conrad, P.N. First, W.A. de Heer, Ultrathin Epitaxial Graphite: 2D

Electron Gas Properties and a Route toward Graphene-based Nanoelectronics, The Journal of Physical Chemistry B, 108 (2004) 19912-19916.

[87] A. Charrier, A. Coati, T. Argunova, F. Thibaudau, Y. Garreau, R. Pinchaux, I. Forbeaux, J.-M. Debever, M. Sauvage-Simkin, J.-M. Themlin, Solid-state decomposition of silicon carbide for growing ultra-thin heteroepitaxial graphite films, Journal of Applied Physics, 92 (2002) 2479-2484.

[88] R. Hawaldar, P. Merino, M.R. Correia, I. Bdikin, J. Gracio, J. Mendez, J.A. Martin-Gago, M.K. Singh, Large area high-throughput synthesis of monolayer graphene sheet by hot filament thermal chemical vapor deposition, Scientific reports, 2 (2012) 682.

[89] Y.H. Zhang, Z.Y. Chen, B. Wang, Y.W. Wu, Z. Jin, X.Y. Liu, G.H. Yu, Controllable growth of millimeter-size graphene domains on Cufoil, Materials Letters, 96 (2013) 149-151.

[90] B.-J. Lee, T.-W. Lee, S. Park, H.-Y. Yu, J.-O. Lee, S.-H. Lim, G.-H. Jeong, Low-temperature synthesis of thin graphite sheets using plasma-assisted thermal chemical vapor deposition system, Materials Letters, 65 (2011) 1127-1130.

[91] E. Kim, H. An, H. Jang, W.-J. Cho, N. Lee, W.-G. Lee, J. Jung, Growth of Few-Layer Graphene on a Thin Cobalt Film on a Si/SiO_2 Substrate, Chemical Vapor Deposition, 17 (2011) 9-14.

[92] H. Ueta, M. Saida, C. Nakai, Y. Yamada, M. Sasaki, S. Yamamoto, Highly oriented monolayer graphite formation on Pt(1 1 1) by a supersonic methane beam, Surface Science, 560 (2004) 183-190.

[93] D.E. Starr, E.M. Pazhetnov, A.I. Stadnichenko, A.I. Boronin, S.K. Shaikhutdinov, Carbon films grown on Pt(1 1 1) as supports for model gold catalysts, Surface Science, 600 (2006) 2688-2695.

[94] P. Zeller, S. Dänhardt, S. Gsell, M. Schreck, J. Wintterlin, Scalable synthesis of graphene on single crystal Ir(111) films, Surface Science, 606 (2012) 1475-1480.

[95] S. Marchini, S. Günther, J. Wintterlin, Scanning tunneling microscopy of graphene on Ru(0001), Physical Review B, 76 (2007) 075429.

[96] W. Liu, H. Li, C. Xu, Y. Khatami, K. Banerjee, Synthesis of high-quality monolayer and bilayer graphene on copper using chemical vapor deposition, Carbon, 49 (2011) 4122-4130.

[97] Y.H. Wu, T. Yu, Z.X. Shen, Two-dimensional carbon nanostructures: Fundamental properties, synthesis, characterization, and potential applications, Journal of Applied Physics, 108 (2010) 071301.

[98] J. Wintterlin, M.L. Bocquet, Graphene on metal surfaces, Surface Science, 603 (2009) 1841-1852.

[99] Y. Gamo, A. Nagashima, M. Wakabayashi, M. Terai, C. Oshima, Atomic structure of monolayer graphite formed on Ni(111), Surface Science, 374 (1997) 61-64.

[100] T. Yamada, M. Ishihara, M. Hasegawa, Large area coating of graphene at low temperature using a roll-to-roll microwave plasma chemical vapor deposition, Thin Solid Films, 532 (2013) 89-93.

[101] D. Stojanović, N. Woehrl, V. Buck, Synthesis and characterization of graphene films by hot filament chemical vapor deposition, Physica Scripta, 2012 (2012) 014068.

[102] V.-M.F. Soler, J. Badia-Canal, C.C. Roca, E.P. Miralles, E.B. Serra, J.-L.A. Bella, Hot wire chemical vapor deposition of few layer graphene on copper substrates, Japanese Journal of Applied Physics, 52 (2013) 01AK02.

[103] M.J. Kim, Y. Jeong, S. Sohn, S.Y. Lee, Y.J. Kim, K. Lee, Y.H. Kahng, J.-H. Jang, Fast and low-temperature reduction of graphene oxide films using ammonia plasma, AIP Advances, 3 (2013) 012117.

[104] M. Nasrollahzadeh, F. Babaei, P. Fakhri, B. Jaleh, Synthesis, characterization, structural, optical properties and catalytic activity of reduced graphene oxide/copper nanocomposites, RSC Advances, 5 (2015) 10782-10789.

[105] Y. Hu, K. Wang, Q. Zhang, F. Li, T. Wu, L. Niu, Decorated graphene sheets for label-free DNA impedance biosensing, Biomaterials, 33 (2012) 1097-1106.

[106] A. Kumar, S. Patil, A. Joshi, V. Bhoraskar, S. Datar, P. Alegaonkar, Mixed phase, sp^2–sp^3 bonded, and disordered few layer graphene-like nanocarbon: Synthesis and characterizations, Applied Surface Science, 271 (2013) 86-92.

[107] D.W. Lee, J.W. Seo, sp^2/sp^3 Carbon Ratio in Graphite Oxide with Different Preparation Times, The Journal of Physical Chemistry C, 115 (2011) 2705-2708.

[108] F.A. Chowdhury, T. Morisaki, J. Otsuki, M.S. Alam, Optoelectronic properties of graphene oxide thin film processed by cost-effective route, Applied Surface Science, 259 (2012) 460-464.

[109] A. Mathkar, D. Tozier, P. Cox, P. Ong, C. Galande, K. Balakrishnan, A. Leela Mohana Reddy, P.M. Ajayan, Controlled, Stepwise Reduction and Band Gap Manipulation of Graphene Oxide, The Journal of Physical Chemistry Letters, 3 (2012) 986-991.

[110] B. Zhao, P. Liu, Y. Jiang, D. Pan, H. Tao, J. Song, T. Fang, W. Xu, Supercapacitor performances of thermally reduced graphene oxide, Journal of Power Sources, 198 (2012) 423-427.

[111] U.N. Maiti, J. Lim, K.E. Lee, W.J. Lee, S.O. Kim, Three-Dimensional Shape Engineered, Interfacial Gelation of Reduced Graphene Oxide for High Rate, Large Capacity Supercapacitors, Advanced Materials, 26 (2014) 615-619.

[112] L. Qiu, H. Zhang, W. Wang, Y. Chen, R. Wang, Effects of hydrazine hydrate treatment on the performance of reduced graphene oxide film as counter electrode in dye-sensitized solar cells, Applied Surface Science, 319 (2014) 339-343.

[113] S. Prezioso, F. Perrozzi, L. Giancaterini, C. Cantalini, E. Treossi, V. Palermo, M. Nardone, S. Santucci, L. Ottaviano, Graphene Oxide as a Practical Solution to High Sensitivity Gas Sensing, The Journal of Physical Chemistry C, 117 (2013) 10683-10690.

[114] I.-Y. Sohn, D.-J. Kim, J.-H. Jung, O.J. Yoon, T. Nguyen Thanh, T. Tran Quang, N.-E. Lee, pH sensing characteristics and biosensing application of solution-gated reduced graphene oxide field-effect transistors, Biosensors and Bioelectronics, 45 (2013) 70-76.

[115] D. Yang, A. Velamakanni, G. Bozoklu, S. Park, M. Stoller, R.D. Piner, S. Stankovich, I. Jung, D.A. Field, C.A. Ventrice Jr, R.S. Ruoff, Chemical analysis of graphene oxide films after heat and chemical treatments by X-ray photoelectron and Micro-Raman spectroscopy, Carbon, 47 (2009) 145-152.

[116] S.Y. Toh, K.S. Loh, S.K. Kamarudin, W.R.W. Daud, Graphene production via electrochemical reduction of graphene oxide: Synthesis and characterisation, Chemical Engineering Journal, 251 (2014) 422-434.

[117] J. Yang, Y. Zhou, L. Sun, N. Zhao, C. Zang, X. Cheng, Synthesis, characterization and optical property of graphene oxide films, Applied Surface Science, 258 (2012) 5056-5060.

[118] H.-J. Shin, K.K. Kim, A. Benayad, S.-M. Yoon, H.K. Park, I.-S. Jung, M.H. Jin, H.-K. Jeong, J.M. Kim, J.-Y. Choi, Y.H. Lee, Efficient Reduction of Graphite Oxide by Sodium Borohydride and Its Effect on Electrical Conductance, Advanced Functional Materials, 19 (2009) 1987-1992.

[119] S. Gilje, S. Han, M. Wang, K.L. Wang, R.B. Kaner, A Chemical Route to Graphene for Device Applications, Nano Letters, 7 (2007) 3394-3398.

[120] X. Fan, W. Peng, Y. Li, X. Li, S. Wang, G. Zhang, F. Zhang, Deoxygenation of Exfoliated Graphite Oxide under Alkaline Conditions: A Green Route to Graphene Preparation, Advanced Materials, 20 (2008) 4490-4493.

Chapter 2

Experimental Details

This chapter gives a brief description of the different methods used for the preparation of different allotropes of carbon such as diamond-like carbon (DLC), carbon nanoflakes (CNF), graphene and graphene oxide thin films. Different characterization techniques used for the analysis of different properties of materials are also described in this chapter.

2.1 Preparation of thin films

In the present thesis work, two different techniques are used for the preparation of thin films of different carbon nanomaterials. Diamond-like carbon, carbon nanoflakes and graphene thin films were prepared using hot filament chemical vapor deposition (HFCVD) method, whereas, chemically modified graphene (also known as graphene oxide (GO)) was prepared using chemical routes. The detail descriptions about these techniques are discussed in the next sections, whereas the parameters used for the preparation of different allotropes of carbon are given in beginning of each chapter presenting the studies on respective allotropes.

2.1.1 Hot filament chemical vapor deposition (HFCVD)

As discussed in chapter 1, the motivation behind the present thesis work is to understand the growth of different carbon nanomaterials: diamond like carbon, carbon nanoflakes, single and multi-layers graphene by HFCVD method and optimization of deposition parameters for the growth of these films. In order to achieve thin films of different carbon nanomaterials, films were deposited by varying process pressure (PP), substrate temperature (T_S), CH_4/H_2 gas flow rate, filament to substrate distance and also on different substrates such as corning 1737 glass, indium tin oxide (ITO) coated glass, crystalline silicon (c-Si) wafer and Ni foil. The details about the deposition parameters such as PP, T_S, CH_4/H_2 gas flow rate, etc. for the preparation of different carbon nanomaterials is described in the beginning of each chapter. Films were deposited using high purity (99.99%) methane (CH_4) and hydrogen (H_2). For each deposition, a new tungsten filament was used to avoid the formation of carbide on the filament to minimize the error in filament temperature. The diameter of the filament wire was 0.5 mm and four pieces of 7 cm long wires were used in parallel geometry to obtain filament temperature in the range of 2000 – 2200 ^oC. Substrates were heated using radiative heater placed at 0.5 mm above the substrate holder and substrate temperature was measured using K-type thermocouple attached with substrate holder. Prior to deposition, chamber was evacuated to a pressure less than 10^{-6} mbar using turbo molecular pump for 5 to 6 hours. The detail description about HFCVD system is discussed in next section.

2.1.1.i Description of HFCVD method

HFCVD is one of the most popular method for the fabrication of large area Si thin films for solar cell applications [1-3]. However, this method is relatively new for the preparation of carbon nanomaterials, especially for carbon nanoflakes [4] and graphene [5]. In this technique, the precursor gases are decomposed thermally and catalytically into different radicals while passing through high filament temperature, generally in the range of 2000 – 2200 ^oC [6-9]. This method is also known as catalytic CVD (Cat-CVD), due to catalytically decomposition of precursor gases [9-11]. Various metals such as tungsten, tantalum, molybdenum, etc. can be used as a filament [8, 10, 12, 13]. This method has several advantages such as low substrate temperature growth, high gas decomposition efficiency, large area deposition, absence of ion bombardment on growing films surface, etc. over other conventional plasma enhanced chemical vapor deposition (PECVD) technique [14]. Also, it is possible to vary the microstructure of the films from amorphous to nano/micro crystalline by tuning the deposition parameters in this method. Usually for the growth of different allotropes of carbon, different carbon source gases such as CH_4, C_2H_2, CF_4, C_2F_6 etc. can be used as a precursor in HFCVD method [4, 10]. In present thesis work, methane gas is used as a precursor for the synthesis of different type of carbon allotropes. Due to low decomposition efficiency of methane, high filament temperature is necessary for the growth of diamond like carbon and graphene thin films. Therefore, filament temperature in the range of 2000 – 2200 ^{o}C is used for the fabrication of carbon thin films [14, 15]. H_2 gas is used as carrier gas and also for the dilution leads to the formation of crystalline phase by reducing dangling carbon bonds.

Figure 2.1 shows the schematic of general HFCVD system and designed HFCVD system in our laboratory as shown in figure 2.2. The HFCVD system consist of two cylindrical chambers made of stainless steel (SS, 304 grade) separated by a gate valve. One of them is deposition chamber and other is load lock chamber. A high temperature water cooled substrate heater ($\leq$ 950 ^{o}C) is attached with the system. Fabrication system is designed in such a way that, there is flexibility in substrate heater for up and down movement to adjust the separation between filament and substrates. Filament as well as gas inlets are surrounded by SS gas confinement cup which facilitates the efficient dissociation of precursor gases.

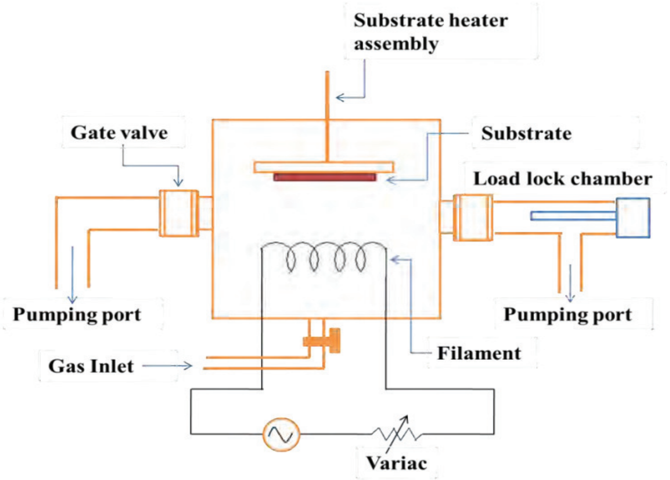

Figure 2.1: *Schematic of a general HFCVD system.*

Figure 2.2: *Designed HFCVD system with gas manifold in our laboratory (left) and HFCVD system during deposition of the films (right).*

2.1.2 Chemical routes

Graphene oxide films are prepared by chemical routes using modified Hummer's method. Thin films of graphene oxide are made by drop casting technique. The procedure for the preparation of graphene oxide and reduced graphene oxide (graphene like sheets) is given in details in the section of experimental details of chapter 6.

2.2 Characterization techniques

Thin films prepared by above mentioned methods are characterized using several different characterization techniques to study the structural, optical (linear/nonlinear) and electrical properties. The details about different characterization techniques are described below.

2.2.1 Structural characterizations

2.2.1.i Field emission scanning electron microscopy (FESEM)

Surface morphology of the films were characterized by field emission scanning electron microscopy (FESEM, model: ΣIGMA ZEISS) as shown in figure 2.3 (a). FESEM were operated with an accelerating voltage of 2 to 4 KeV and films were coated with very thin gold layer with plasma to avoid the charging effect during measurement. In this technique, a field emission cathode in electron gun provides high energy narrow electron beam which is focused on the sample and results in the improvement of resolution of image.

2.2.1.ii Atomic force microscopy (AFM)

Atomic force microscopy (AFM, model: Agilent, 5500 series), as shown in figure 2.3 (b), is used to get the surface morphology of the films. AFM is very important characterization technique to study the directional growth of different materials. The measurements were performed in acoustic (non-contact) mode using silicon cantilever with force constant 33 N/m and resonance frequency of 304 KHz. Roughness of the films is calculated using “Pico View’ software for the selected area of 2 μm x 2 μm.

2.2.1.iii X-ray diffraction (XRD)

X-ray diffraction pattern (XRD, model: Rigaku TTRAX-III), as shown in figure 2.3 (c), is used to characterize microstructural properties of the films. XRD measurements were performed using CuK$_\alpha$ ($\lambda = 1.54$ Å) radiation in thin film mode on Si/quartz substrates.

The mean crystallite size (d_{XRD}) of the films was calculated using Scherrer's formula as follows (equation 2.1).

$$d_{XRD} = \frac{0.9\,\lambda}{\beta cos\theta_{hkl}} \quad \ldots\ldots\ldots\ldots\ldots\ldots\ldots\ldots\ldots\ldots\ldots\ldots\ldots \text{(2.1)}$$

Where, λ is the wavelength of X-ray, β is the broadening (FWHM) and θ_{hkl} $(=\frac{1}{2}(2\theta_{hkl}))$ is the peak position corresponding to different (hkl) planes.

Figure 2.3: *Experimental setup of different characterization techniques: (a) Field emission scanning electron microscopy, (b) Atomic force microscopy, (c) X-ray diffraction, (d) Raman spectroscopy, (e) Fourier transform infrared spectroscopy, (f) transmission electron microscopy and (g) Stylus profilometer.*

2.2.1.iv Raman scattering

Raman scattering is inelastic scattering of photons with materials and used for analyzing the microstructure properties of different materials. It is a non-destructive technique. Among all other structural characterization techniques, Raman scattering is called backbone for the study of microstructure of carbon based materials. Raman spectra of all the samples were recorded using ‘Horiba JY LabRam HR800’ micro-Raman instruments, as shown in figure 2.3 (d), with excitation wavelength of either 488 nm, 514.53 nm of Ar^+ laser and 632.8 nm of He-Ne laser for different films. The spot size of the incident laser at the focus of the sample was around 1 μm.

2.2.1.v Fourier transform infrared (FTIR) spectroscopy

Fourier transform infrared (FTIR) spectroscopy is a non-destructive technique to analyze the chemical bonding of the materials. The basic principle of this technique is based on the fact that each molecular bond has its own distinct quantized vibrational levels whose frequency lie usually in the mid-infrared region of 200 – 4000 cm^{-1} and when the frequency of an incident infrared radiation matches with the frequency of molecular vibration modes, radiations are absorbed by the molecules. In the present thesis work, a single beam ‘Perkin Elmer BX’ FTIR spectrometer, as shown in figure 2.3 (e), is used to record the IR transmission spectra of the films deposited on undoped crystalline Si (100) wafer. The spectrometer is operated using normal incidence with a resolution of 4 cm^{-1} with twenty scans for each samples.

2.2.1.vi X-ray photoelectron spectroscopy (XPS)

Surface chemical compositions were analyzed using X-ray photoelectron spectroscopy (XPS) (from RRCAT, Indore). Typical XPS instrument consist of high vacuum chamber, an x-ray source, photoelectrons energy analyzer and electron detector. Sample is placed in high vacuum chamber and monochromatic x-ray beam from either synchrotron or a laboratory source is allowed to fall on the sample. In the present thesis work, angle integrated experimental station with AlK_α source (1486.6 eV) was used to measure binding energy of core level. Incident beam from the X-ray gun was at 45^o from the surface of the sample. The angle between incident beam and entrance slit of the analyzer was about 90^o. The aperture diameter of the entrance slit of the analyzer was 6 mm and exit aperture was 3 mm × 10 mm. The pass energy during detailed and quick survey XPS measurements was 30 and 50 eV respectively.

2.2.1.vii Transmission electron microscopy (TEM)

Transmission electron microscope (TEM, model: JEOL JEM 2100), as shown in figure 2.3 (f), is used to study the microstructure properties of different carbon nanostructures. For TEM measurements, films were deposited on carbon coated Cu mesh TEM grid. Here, an accelerating voltage of 200 KV was used during the operation of TEM. In case of HRTEM, spot size is varied from 20 – 200 nm and image was taken at a magnification of 10^5 to 10^6 X. During the observation of selected area electron diffraction (SAED) pattern, a field limited aperture was inserted. From SAED pattern, inter planar spacing is calculated using “Gatan digital micrograph’ software.

2.2.1.viii Stylus profilometer

Stylus profilometer (model: Veeco, Dektak 150), as shown in figure 2.3 (g), is used for measuring the thickness of the films for present study. It is capable to scan area of tens of millimeters with a vertical range starting from a few nanometers up to hundreds of microns. The main disadvantage of stylus profilometer is the contact mode, where tip is in contact with the surface of the films, which causes the error in thickness measurement in the case of very soft materials like organic thin films. However, in present thesis work, thickness measurements were performed 2 to 3 times at the same location and no fluctuation in the thickness of the films was observed.

2.2.2 Optical characterizations

2.2.2.1 UV-Vis-NIR spectroscopy

UV-Vis-NIR spectrometer is very important characterization technique to measure the transmittance / absorbance of the film. It records the fraction of light transmitted by the film and absorption due to the electronic transition from the ground state to an excited state. UV-Vis-NIR spectroscopy, as shown in figure 2.4, in the transmission mode was performed on the films deposited on corning 1737 glass / quartz substrates. Measurements were performed using ‘Shimadzu UV3101 PC’ dual beam spectrometer in the range of 250 – 2500 nm. For removing the effect of absorption of substrates, a bare substrate is used in the path of reference beam. The main advantage of UV-Vis-NIR spectroscopy is its ability to measure the properties of the films in large area of millimeter dimension (~ 5mm x 5mm or more).

Figure 2.4: *Experimental setup of UV-Vis-NIR spectroscopy.*

2.2.2.2 Single beam Z-scan technique

Third order optical nonlinear refractive index coefficient (n_2) of CNF was measured by single beam Z-scan using closed aperture configuration. Z-scan has become a popular method for the measurements of optical nonlinearities; nonlinear refractive index and nonlinear absorption [16-19]. When the medium is exposed to very high intensity of electromagnetic field (i.e. laser beam), polarization induced by electric field becomes nonlinear and it behaves as a nonlinear medium. Therefore increase or decrease in the refractive index (n_r) of the medium, results in the positive and negative nonlinear refractive index respectively. The expression relating the refractive index of nonlinear medium with intensity (I) of electromagnetic field is $n_r = n_0 \pm n_2 I$, where n_0 is linear refractive index and n_2 is the third order nonlinear refractive index coefficient [16, 17].

Optical nonlinearity of carbon nanoflakes and graphene was measured using single beam closed Z-scan technique. In Z-scan experiment, Gaussian beam of He-Ne laser (MELLES GRIOT 05-LHP-927, 632.8 nm) was used. The laser was focused onto the sample using convex lens with a focal length of 5 cm. The sample was translated along the optic axis across the focal plane. The intensity distribution of the transmitted beam through the sample was recorded by a CCD detector (PCO PixelFly). The experimental setup of single beam Z-scan technique and ray diagram are shown in figure 2.5.

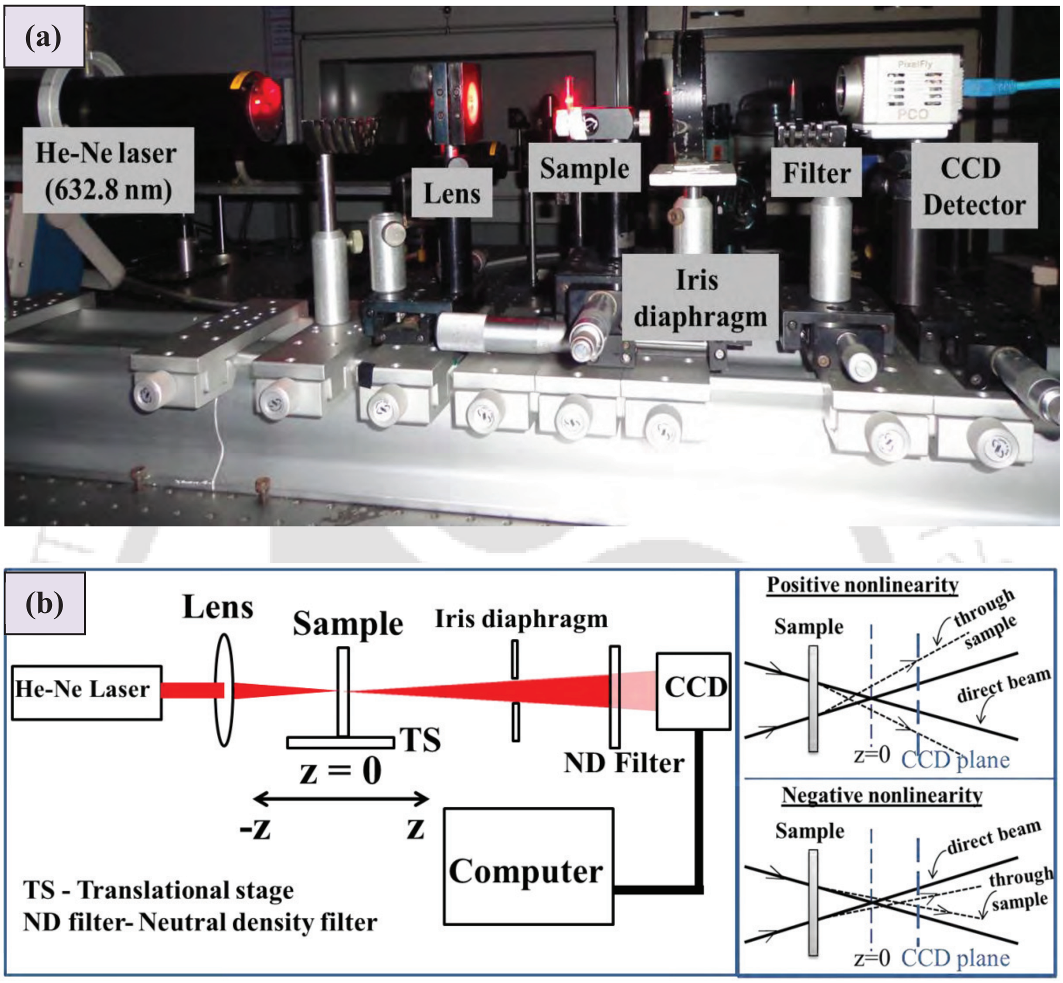

Figure 2.5: *(a) Experimental setup of single beam Z-scan technique and (b) ray diagram.*

2.2.3 Electrical characterization

2.2.3.1 Temperature dependent dark conductivity

Temperature dependent dark conductivity of different carbon nanomaterials are studied using two-probe coplanar geometry in high vacuum of the order of 10^{-5} mbar. The experimental setup of temperature dependent electrical conductivity is shown in figure 2.6. Samples were mounted on a stainless steel sample holder which was attached with the heater. A thin mica sheet, having high thermal conductivity, was placed between the sample and sample holder to maintain the electrical insulation between the electrodes and sample holder. Electrodes were made using high purity (99.99%) silver paste and measurements were done using Keithley 6430 source meter. Temperature of the films was measured on another substrate, placed parallel to the sample, with the help of platinum resistance thermometer (PT-100) and digital multimeter (Agilent, model: 34401A).

In case of coplanar geometry, conductivity (σ) of the film is given by (equation 2.2).

$$\sigma = \frac{Id_s}{Vlt} \qquad (2.2)$$

Where, l is the length of electrodes, d_s is the separation between the electrodes, V is the applied voltage, I is the measured current and t is the thickness of the films.

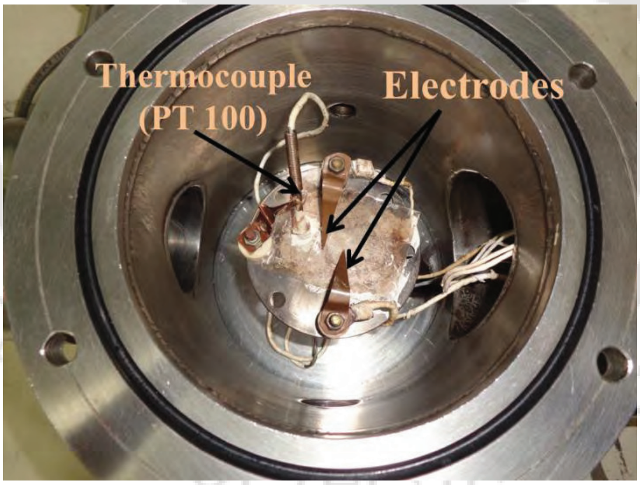

Figure 2.6: *Experimental setup of temperature dependent electrical conductivity.*

2.2.4 Field effect transistor (FET) characterization

To study the electrical transport properties of charge carriers in graphene, as fabricated graphene channel field effect transistor was characterized using pin contact (micro positioners) in air. Graphene channel FET were fabricated on SiO_2 coated (300 nm thick) heavely doped p-type Si substrates. It has three electrodes source (s), gate (g) and drain (d), which is made by thermal evaporation of Al. To avoid the scratching on Al electrodes, small dots of Ag paste is used on the electrodes. Measurements were done using Keithley 6430 and 2450 source meter.

2.3 References

[1] S.K. Soni, A. Phatak, R.O. Dusane, High deposition rate device quality a-Si:H films at low substrate temperature by HWCVD technique, Solar Energy Materials and Solar Cells, 94 (2010) 1512-1515.

[2] R.E.I. Schropp, Advances in solar cells made with hot wire chemical vapor deposition (HWCVD): superior films and devices at low equipment cost, Thin Solid Films, 403–404 (2002) 17-25.

[3] P. Gogoi, P. Agarwal, Structural and optical studies on hot wire chemical vapour deposited hydrogenated silicon films at low substrate temperature, Solar Energy Materials and Solar Cells, 93 (2009) 199-205.

[4] N.G. Shang, F.C.K. Au, X.M. Meng, C.S. Lee, I. Bello, S.T. Lee, Uniform carbon nanoflake films and their field emissions, Chemical Physics Letters, 358 (2002) 187-191.

[5] V.-M.F. Soler, J. Badia-Canal, C.C. Roca, E.P. Miralles, E.B. Serra, J.-L.A. Bella, Hot wire chemical vapor deposition of few layer graphene on copper substrates, Japanese Journal of Applied Physics, 52 (2013) 01AK02.

[6] M.M. Kamble, V.S. Waman, A.H. Mayabadi, S.S. Ghosh, B.B. Gabhale, S.R. Rondiya, A.V. Rokade, S.S. Khadtare, V.G. Sathe, T. Shripathi, H.M. Pathan, S.W. Gosavi, S.R. Jadkar, Hydrogenated Silicon Carbide Thin Films Prepared with High Deposition Rate by Hot Wire Chemical Vapor Deposition Method, Journal of Coatings (Hindawi Publishing Corporation), 2014 (2014) 905903 (http://dx.doi.org/905910.901155/902014/905903).

[7] X.T. Zhou, N. Wang, H.L. Lai, H.Y. Peng, I. Bello, N.B. Wong, C.S. Lee, S.T. Lee, β-SiC nanorods synthesized by hot filament chemical vapor deposition, Applied Physics Letters, 74 (1999) 3942-3944.

[8] T. Wang, H.W. Xin, Z.M. Zhang, Y.B. Dai, H.S. Shen, The fabrication of nanocrystalline diamond films using hot filament CVD, Diamond and Related Materials, 13 (2004) 6-13.

[9] D.S. Dandy, M.E. Coltrin, Effects of temperature and filament poisoning on diamond growth in hot-filament reactors, Journal of Applied Physics, 76 (1994) 3102-3113.

[10] T. Itoh, Synthesis of carbon nanowalls by hot-wire chemical vapor deposition, Thin Solid Films, 519 (2011) 4589-4593.

[11] T. Itoh, S. Shimabukuro, S. Kawamura, S. Nonomura, Preparation and electron field emission of carbon nanowall by Cat-CVD, Thin Solid Films, 501 (2006) 314-317.

[12] R.V. Godbole, M.A. More, A.S. Gupte, V.P. Godbole, New Method for Synthesis of Coatings of Molybdenum, Tungsten, Their Carbides and Composites, Open Journal of Synthesis Theory and Applications, 2 (2013) 78-85.

[13] D.M. Li, R. Hernberg, T. Mäntylä, Catalytic dissociation of hydrogen on a tantalum carbide filament in the HFCVD of diamond, Diamond and Related Materials, 7 (1998) 1709-1713.

[14] S. Seiji, H. Yuichi, T. Masanori, I. Takashi, N. Shuichi, Preparation of Carbon Nanowall by Hot-Wire Chemical Vapor Deposition and Effects of Substrate Heating Temperature and Filament Temperature, Japanese Journal of Applied Physics, 47 (2008) 8635.

[15] N. Lisi, R. Giorgi, M. Re, T. Dikonimos, L. Giorgi, E. Salernitano, S. Gagliardi, F. Tatti, Carbon nanowall growth on carbon paper by hot filament chemical vapour deposition and its microstructure, Carbon, 49 (2011) 2134-2140.

[16] F.W. Shi, X.J. Meng, G.S. Wang, J.L. Sun, T. Lin, J.H. Ma, Y.W. Li, J.H. Chu, The third-order optical nonlinearity of $Bi_{3.25}La_{0.75}Ti_3O_{12}$ ferroelectric thin film on quartz, Thin Solid Films, 496 (2006) 333-335.

[17] A.R. Sadrolhosseini, A.S.M. Noor, N. Faraji, A. Kharazmi, M. AdzirMahdi, Optical Nonlinear Refractive Index of Laser-Ablated Gold Nanoparticles Graphene Oxide Composite, Journal of Nanomaterials, 2014 (2014) 962917 (http://dx.doi.org/962910.961155/962014/962917).

[18] M. Sheik-bahae, A.A. Said, E.W. Van Stryland, High-sensitivity, single-beam n_2 measurements, Optics Letters, 14 (1989) 955-957.

[19] M. Sheik-Bahae, A.A. Said, T.H. Wei, D.J. Hagan, E.W. Van Stryland, Sensitive measurement of optical nonlinearities using a single beam, IEEE Journal of Quantum Electronics, 26 (1990) 760-769.

Chapter 3

Diamond like Carbon Thin Films

In this chapter, structural properties of diamond like carbon (DLC) thin films deposited by hot filament chemical vapor deposition (HFCVD) method and comparative study of growth of DLC films on two different substrates, p-type Si (resistivity, 0.001 – 0.006 ohm cm) and indium tin oxide (ITO) coated glass substrates, are discussed in detail. The change in microstructural properties of DLC thin films is studied by varying the concentration of methane (CH_4) at low substrate temperature (T_S). Microstructural properties of the films are studied using field emission scanning electron microscopy (FESEM), Atomic force microscopy (AFM), X-ray diffraction (XRD), Raman scattering and transmission electron microscopy (TEM). The motivation behind this chapter is to deposit diamond like carbon thin films with high density of sp^3 bonded carbon atoms on non-carbon affinity substrates.

3.1 Experimental details

To study the microstructural properties and comparative study of growth of DLC films on two different substrates, a series of films were deposited on heavily doped p-type Si (100) (resistivity, 0.001 – 0.006 ohm cm) and ITO coated glass substrates by HFCVD method using CH_4 and H_2 as precursor gases. Films were deposited on non-carbon affinity substrates, without any surface pretreatment, by varying CH_4 concentration from

13% to 66% at low T_S of 450 ^oC and at fixed process pressure of 2 mbar. Filament temperature and filament to substrate distance were kept at 2150±50 ^oC and 1 cm respectively. Other deposition parameters such as gas flow rate and deposition time are listed in table 3.1. For TEM study, one of the films was deposited at deposition time of 7 min on TEM grid (carbon coated Cu mesh).

Table 3.1: Deposition parameters for the growth of DLC thin films.

Samples	T_S (^oC)	CH_4 (sccm)	H_2 (sccm)	Deposition time (min)	$CH_4/(CH_4+H_2)$%	Thickness* (nm) (on Si)	Thickness* (nm) (on ITO)
HW116	450 ^oC	3	20	30	13	---	160±20
HW115		3	15	30	16	---	140±10
HW108#		5	15	7	25	---	---
HW109		5	15	20	25	---	---
HW113		5	10	20	33	---	---
HW112		7	10	20	41	40±10	---
HW114		10	5	20	66	90±10	---

* Thickness of the films was measured by stylus profilometer.

Film was deposited on TEM grid.

3.2 Structural properties of DLC thin films on Si substrate

3.2.i FESEM

Figure 3.1 shows the FESEM images of diamond like carbon thin films on Si substrate at different CH_4 concentration of 13%, 16%, 25%, 33% and 66%. FESEM images show the combined growth of nanodiamond and graphite, corresponding to sp^3 and sp^2 bonded carbon atoms, which can be identified as spherical particles and flakes type structure respectively. It is observed that, density of diamond particles is increased with increasing concentration of methane. The observed density of diamond nanoparticles in DLC thin films is 2.6 x $10^8/cm^2$ for the films deposited at methane concentration of 13% and it is increased to 8.4 x $10^9/cm^2$ for the films deposited at methane concentration of 66%.

However, with increasing concentration of methane, growth of carbon nanoflakes is also increased. Density of diamond nanoparticles is measured by counting the number of particles in a unit area [1, 2]. For calculating the density of diamond nanoparticles, FESEM image approximately in the dimension of 6µm x 6µm (large area) is used, whereas enlarged view of FESEM image are shown here to clearly view the diamond nanoparticles. Since as grown carbon nanoflakes are small in height, therefore for the identification of flake type structure, enlarged view of FESEM image are shown in the inset of each of figure 3.1. The growth mechanism of composite structure of diamond and graphitic carbon depends on the kinetic reactions in gaseous / vapor phase [3, 4]. The gaseous activation process depends on the different deposition parameters such as filament temperature, process pressure and filament to substrate distance [3, 5] which dissociate molecular hydrogen into atoms and react with dissociated hydrocarbon species and make a complex mixture of hydrocarbon species such as C_2H_2, CH_4, CH_2, CH, H, etc. including reactive carbon containing species. Hydrogen atoms created by gaseous activation process also extract hydrogen from C-H bonds and thereby creating carbon radical sites on the surface. These radical sites react with gaseous phase carbon containing radicals resulting in adsorption of carbon species and form different type of sp^1 or sp^2 hybridized bonded carbon atoms. The gas phase reaction of atomic hydrogen leads to react with any of sp^1 or sp^2 bonded carbon species and converting them into sp^3 bonded carbon atoms [6-9]. FESEM image shows that at low methane concentration, distribution of the particles are not uniform and lateral dimension of the particle is in the range of 20 – 150 nm for the films deposited at methane concentration of 25% and with increasing concentration of methane to 66%, lateral distribution of particle in the range of 80 – 120 nm is observed.

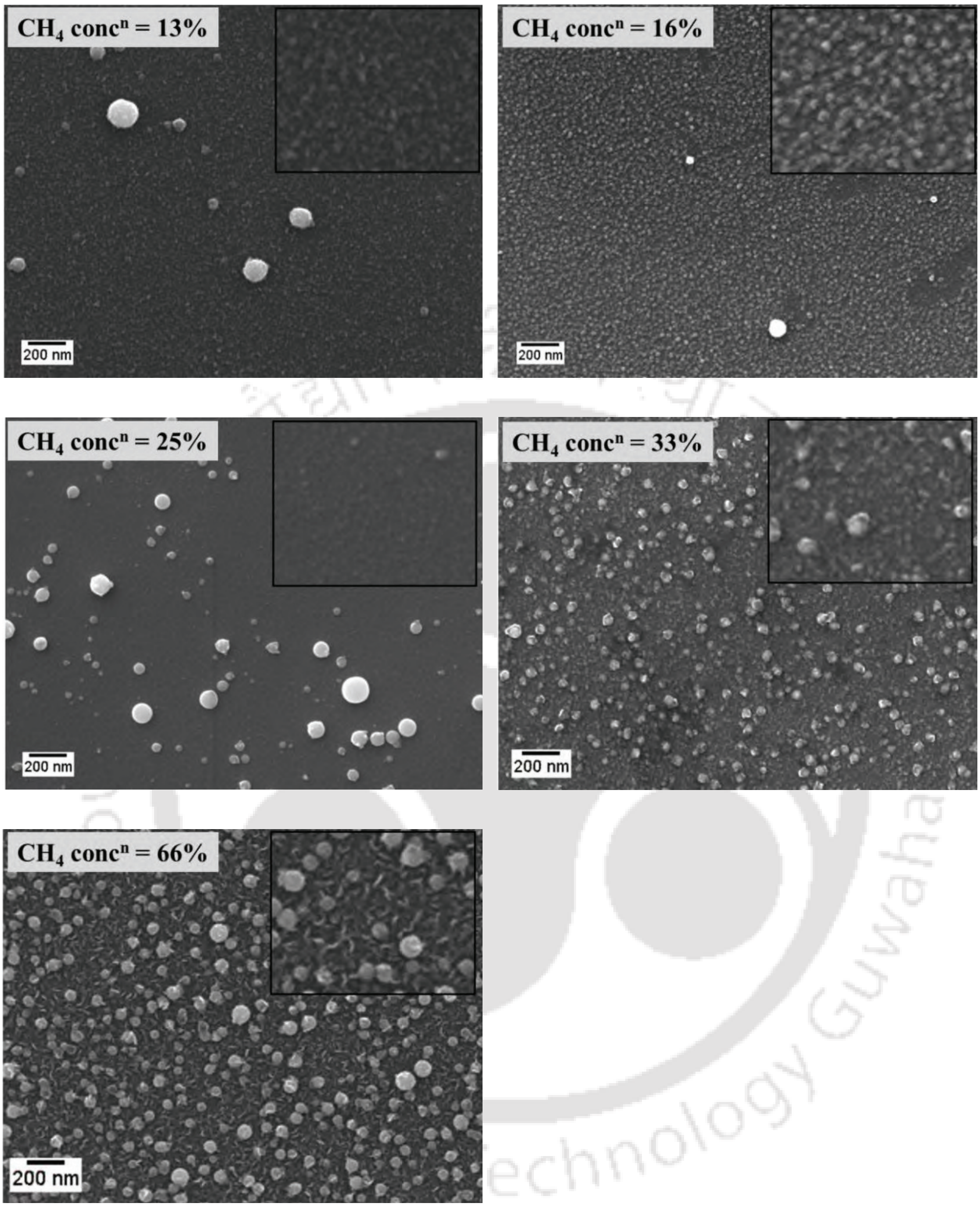

Figure 3.1: *FESEM image of DLC thin films on Si substrate at different* CH_4 *concentration of 13%, 16%, 25%, 33% and 66%.*

3.2.ii AFM

Figure 3.2 shows the AFM images of DLC thin films on Si substrate at different CH_4 concentration of 25% and 66%. Increase in nucleation density with increasing methane concentration is further confirmed by AFM image. The lateral dimension of the particles, as calculated from the surface height profile of AFM image, for the films deposited at methane concentration of 25% is in the range of 70 – 190 nm, whereas, dimension of the particles is in the range of 100 – 150 nm for the films deposited with methane concentration of 66%.

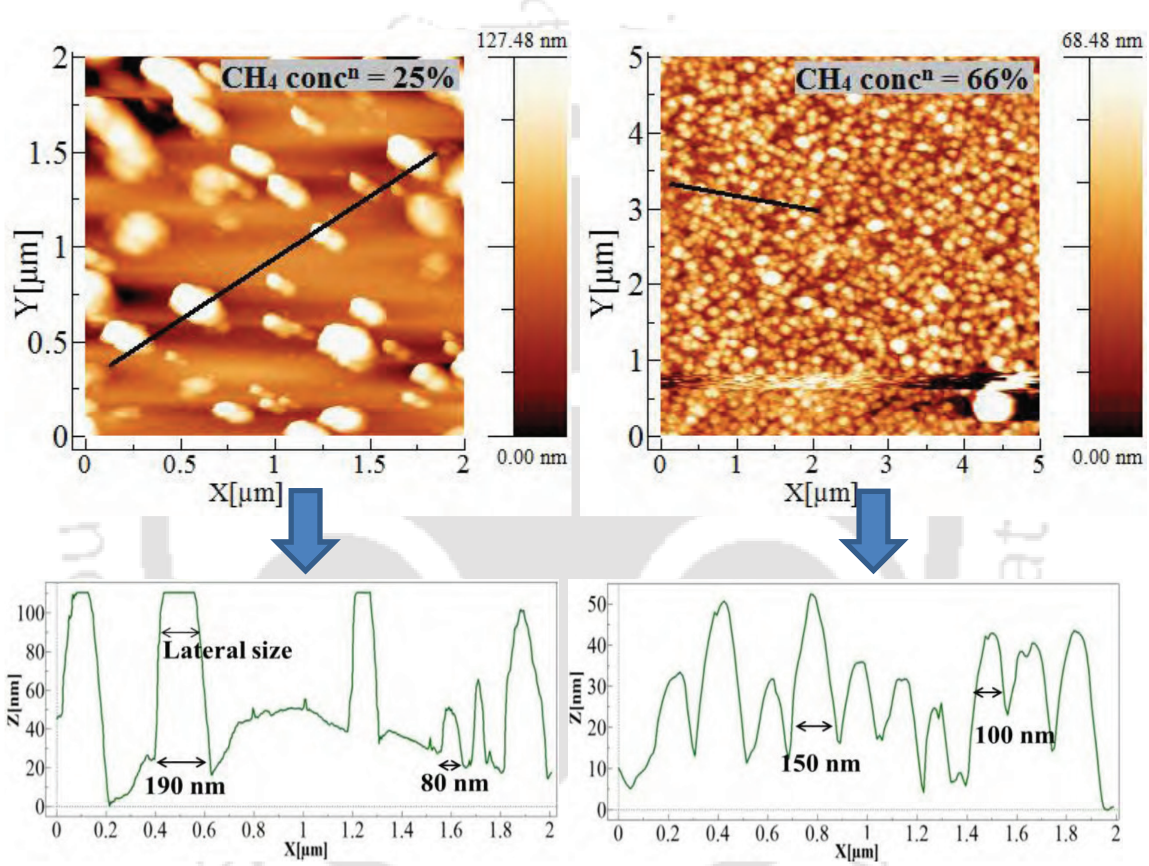

Figure 3.2: *AFM image and corresponding surface height profile of DLC thin films on Si substrate at different CH_4 concentration of 25% and 66%.*

3.2.iii X-ray Diffraction (XRD)

Figure 3.3 shows the X-ray diffraction pattern of DLC thin films on Si substrate (100) deposited with different methane concentration of 33%, 41% and 66%. From the spectra, it is clearly evident that films deposited with different methane concentrations show XRD peak at $2\theta = 44.5^{o}$ corresponding to (111) plane of cubic diamond. This peak is slightly shifted from the standard value of 43.9° [10-12]. The calculated interplanar spacing d_{111} of cubic diamond corresponding to 44.5° is 2.03 Å. The calculated value of interplanar spacing is slightly lower from the standard $d_{spacing}$ of 2.05 Å. The slight shift in peak position of (111) plane of cubic diamond is probably due to the mismatch between the orientation of substrate and growth direction of diamond, which can produce small strain in the films. In these spectra, no peak corresponding to graphitic phase is observed. The reason of absence of graphitic phase in these spectra could be due to very thin layer of graphitic flakes. The average crystallite size of diamond particles is calculated using full width at half maxima (FWHM) of peak at $2\theta = 44.5°$ using Scherrer's formula (mentioned in chapter 2) and is found to be 26.3, 27.1 and 23.6 nm respectively for the films deposited at different methane concentration of 33%, 41% and 66%.

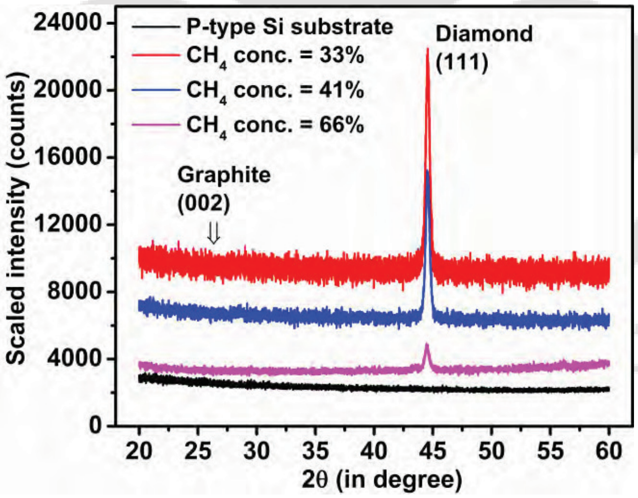

Figure 3.3: *X-ray diffraction pattern of DLC thin films on Si substrate at different CH_4 concentration of 33%, 41% and 66%.*

3.2.iv Raman scattering

Raman spectroscopy is the most important nondestructive characterization technique to identify the different atomic bonding states of sp^3 and sp^2 bonded carbon atoms [13-17].

Films were characterized by Raman spectroscopy with an excitation wavelength of 488 nm. Figure 3.4 shows the Raman spectra of DLC thin films on Si substrate with different CH_4 concentration of 13%, 16%, 25%, 41% and 66%. In order to find the different bonding modes between the carbon atoms in the films, all measured Raman spectra are deconvoluted using Lorentzian fit into five common peaks corresponding to different vibrational modes. The center peak position, Full width at half maxima (FWHM), peak intensity and integrated area of all the deconvoluted Raman spectra are listed in table 3.2. Different characteristic peaks of Raman spectra for DLC films are observed at approximately 1116 cm^{-1}, 1330 cm^{-1}, 1355 cm^{-1}, 1460 – 1500 cm^{-1} and 1596 cm^{-1}. Raman spectra of all the films show a broad and intense peak at ~ 1330 cm^{-1}, which corresponds to the formation of DLC. Another broad peak at ~1460 – 1500 cm^{-1}, corresponds to sp^2 carbon bonds at the grain boundary of sp^3 sites. Raman spectra also show a characteristic peak at ~1116 cm^{-1}, corresponding to the formation of nanocrystalline diamond (NCD / DLC) [13-15, 18, 19]. In addition, all the films show a sharp peak at ~ 1596 cm^{-1} (G band), which indicates the formation of graphitized structure. Another sharp peak at 1355 cm^{-1} (D band) corresponds to disorder induced phonon mode due to defects in hexagonal structure of graphite [14, 15]. Deconvoluted Raman spectra show broad FWHM of the peak centered at 1330 cm^{-1} in the range of 100 – 150 cm^{-1}, indicating the formation of sp^3 bonded carbon atoms. FWHM of G band is in the range of 50 – 60 cm^{-1}, which is larger as compared to that of pure crystalline graphite structure having FWHM in the range of 20 – 25 cm^{-1} [20]. The reason of large FWHM of G band could be due to the slightly amorphous nature of sp^2 bonded network of carbon atoms.

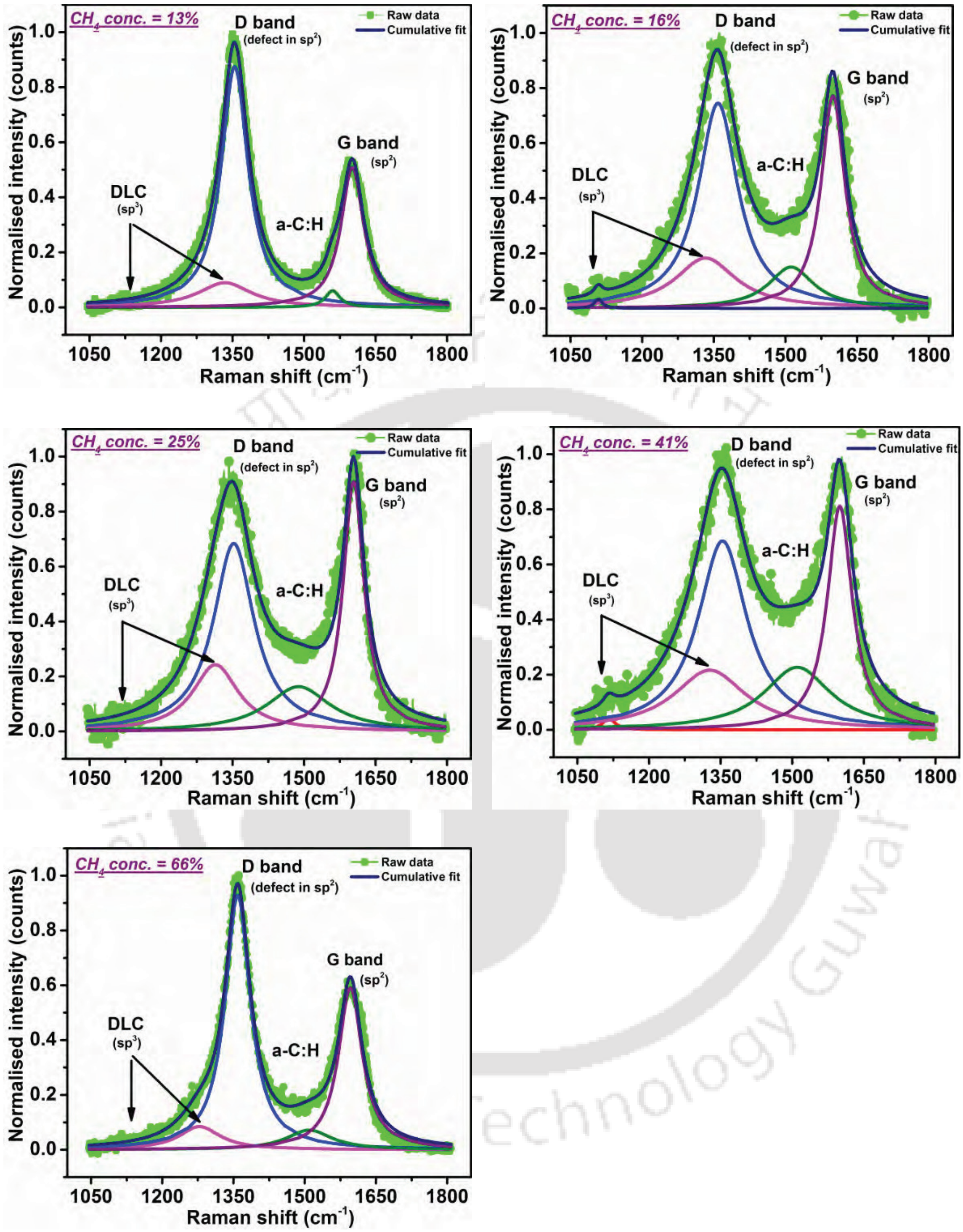

Figure 3.4: *Deconvoluted Raman spectra of DLC thin films on Si substrate at different CH$_4$ concentration of 13%, 16%, 25%, 41% and 66%.*

Raman spectra of all the films show that peak (at 1596 cm^{-1}) corresponding to sp^2 bonded carbon is more intense in comparison to those corresponding to sp^3 modes. This may lead one to believe that films are graphitic rich. However, larger intensity of the peaks corresponding to sp^2 bonded carbon is likely to be due to resonance effect of $\pi - \pi^*$ transition of sp^2 bonded carbon [5, 21, 22]. The sp^2 bonded carbon network exhibits resonance enhancement in the Raman cross-section as sp^2 bonded amorphous carbon has an energy gap of approximately 2 eV which is comparable to energy of incident photon (2.54 eV). The sp^3 bonded carbon atoms do not exhibit such resonance effect due to higher energy gap of approximately 5.5 eV [5, 21, 23, 24]. Therefore, Raman spectra obtained with visible excitation are completely dominated by sp^2 sites having 50 – 230 times larger cross-section than that of sp^3 sites [14, 17, 23, 25]. The relative fraction of sp^3 bonded carbon atoms is calculated using Raman spectra and the values are listed in table 3.2. The relative fraction of sp^3 is calculated using peak intensity as well as integrated area of the peak at 1116 and 1330 cm^{-1} corresponding to sp^3 mode and 1596 cm^{-1} corresponding to sp^2 mode. The relative fraction of sp^3 bonds is also calculated using 50% cross-section of sp^2 sites. The calculated fraction of sp^3 bonds using peak intensity is 13% for the films deposited at methane concentration of 13% and the fraction of sp^3 is increased with increasing concentration of methane and calculated value of sp^3 fraction is 23% for the films deposited at methane concentration of 41%. However, fraction of sp^3 bonded carbon atoms as calculated using integrated area of peaks is higher by ~ 15% than that calculated using intensity of peaks. The calculated values of sp^3 fractions using three different factors such as peak intensity, integrated area and fifty percent cross-section integrated area of sp^2 sites are listed in table 3.2. The fraction of sp^3 content could actually be much higher than this if 50 – 230 times larger cross-section of sp^2 mode is considered for calculating the relative fraction of sp^2 and sp^3 bonded carbon atoms. These results show that with increasing concentration of methane, the relative fraction of sp^3 bonded carbon atoms is increased, which results in the increase in density of nano-diamond particles. However, visible laser excitation wavelength gives only the approximate value of sp^3 bonded carbon due to higher bonding energy of sp^3 bonds. From the calculation of sp^3 fraction using Raman spectra, we have observed that relative fraction of sp^3 bonded carbon is decreased at methane concentration of 66%. The reason of decrease in sp^3 fraction for the films deposited at methane concentration of 66% is due to increase in growth of flakes type structure as well, which results in the enhancement of sp^2 sites in Raman spectra.

Table 3.2: FWHM, peak intensity and integrated area of the peaks and calculated relative fractions of sp^3 bonded carbon atoms for DLC films on Si substrate.

Samples	**DLC (sp^3) (~ 1116 cm^{-1}) (FWHM/peak intensity/Int. area*)**	**DLC (sp^3) (~ 1330 cm^{-1}) (FWHM/peak intensity/Int. area)**	**D band (~ 1355 cm^{-1}) (FWHM/peak intensity/Int. area)**	**G band (sp^2) (~ 1596 cm^{-1}) (FWHM/peak intensity/Int. area)**	**Sp^3/(sp^2+sp^3) % (using peak intensity)**	**Sp^3/(sp^2+sp^3) % (using Int. area)**	**Sp^3/(sp^2+sp^3)% (using Int. area) (50% cross-section of sp^2 sites)**
CH_4 conc^n = 13%	---	135/0.08 / 19	68/ 0.87 / 93	57/ 0.50 / 46	**13**	**29**	**45**
CH_4 conc^n = 16%	20/ 0.03 / 1	153/0.18 / 44	100/0.74 / 117	60/ 0.77 / 73	**21**	**38**	**55**
CH_4 conc^n = 25%	---	116/0.24 / 44	104/0.68 / 111	53/ 0.90 / 76	**21**	**36**	**53**
CH_4 conc^n = 41%	30/ 0.04 / 2	183/0.21 / 62	124/0.68 / 133	63/ 0.81 / 80	**23**	**44**	**61**
CH_4 conc^n = 66%	---	105/0.08 / 14	64/ 0.92 / 93	60/ 0.59 / 56	**12**	**20**	**33**

*Int. area = Integrated area

3.2.v Transmission electron microscopy (TEM)

Figure 3.5 shows the TEM image and selected area electron diffraction (SAED) pattern of DLC for the films deposited at methane concentration of 25% and deposition time of 7 min for study the orientation of lattice planes in mixed phase of diamond like carbon i.e. sp^3 and sp^2 bonded carbon atoms. TEM image shows the growth of nano-diamond particles of approximately equal lateral size in the range of ~30 – 40 nm. SAED pattern shows the polycrystalline nature of the films. Due to presence of both sp^3 and sp^2 phases of carbon bonded atoms, it is difficult to index the entire diffraction pattern. However, some bright rings can be distinguished with interplanar spacing of graphite and diamond. Interplanar $d_{spacing}$ is calculated using "Digital Gatan" software and compared with JCPDS (Joint Committee on Powder Diffraction Standards) data. Centre bright ring with interplanar spacing of 3.21 Å corresponds to (002) plane of graphite. As we move away from the center ring, the observed interplanar spacing are 1.81 Å corresponds to (111) plane of diamond / (102) plane of graphite and 1.37 Å corresponds to (220) plane of diamond / (104) plane of graphite [10].

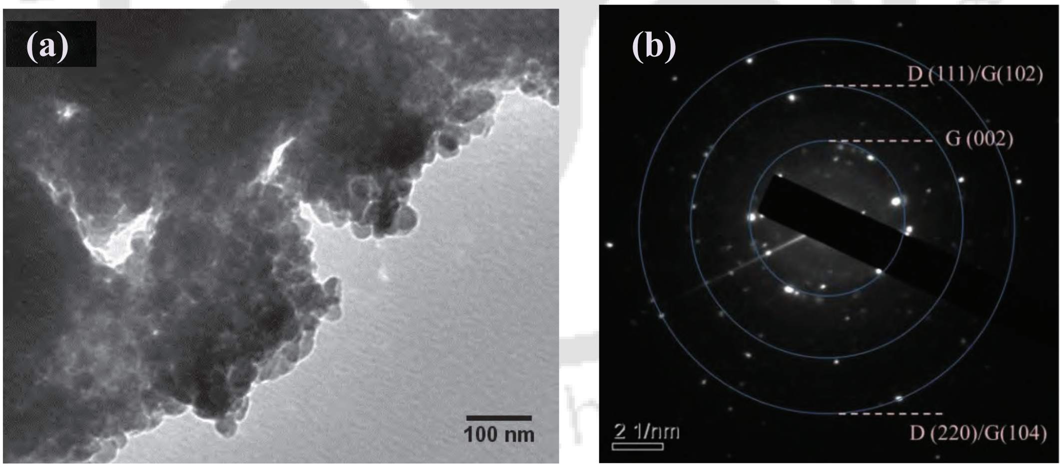

Figure 3.5: *(a) TEM image and (b) SAED pattern of DLC thin film.*

3.3 Structural properties of DLC thin films on ITO coated glass substrate

3.3.i FESEM

Figure 3.6 shows the FESEM images of diamond like carbon thin films on ITO coated glass substrate with different methane concentration of 16%, 25% and 33%. We have observed that, films deposited on ITO coated glass substrate have higher density of nano-diamond particles in comparison to films on Si substrate, which is further confirmed by Raman spectroscopy, as discussed in next section. The dimension of nano-diamond particles is in the range of 10 – 30 nm without having any spacing between them. This indicates that density of diamond particles is in the range of 10^{10} – 10^{11} /cm^2. High density of nano-diamond particles on ITO coated substrate indicate that metallic substrate acts as a catalyst for the growth of DLC films [26].

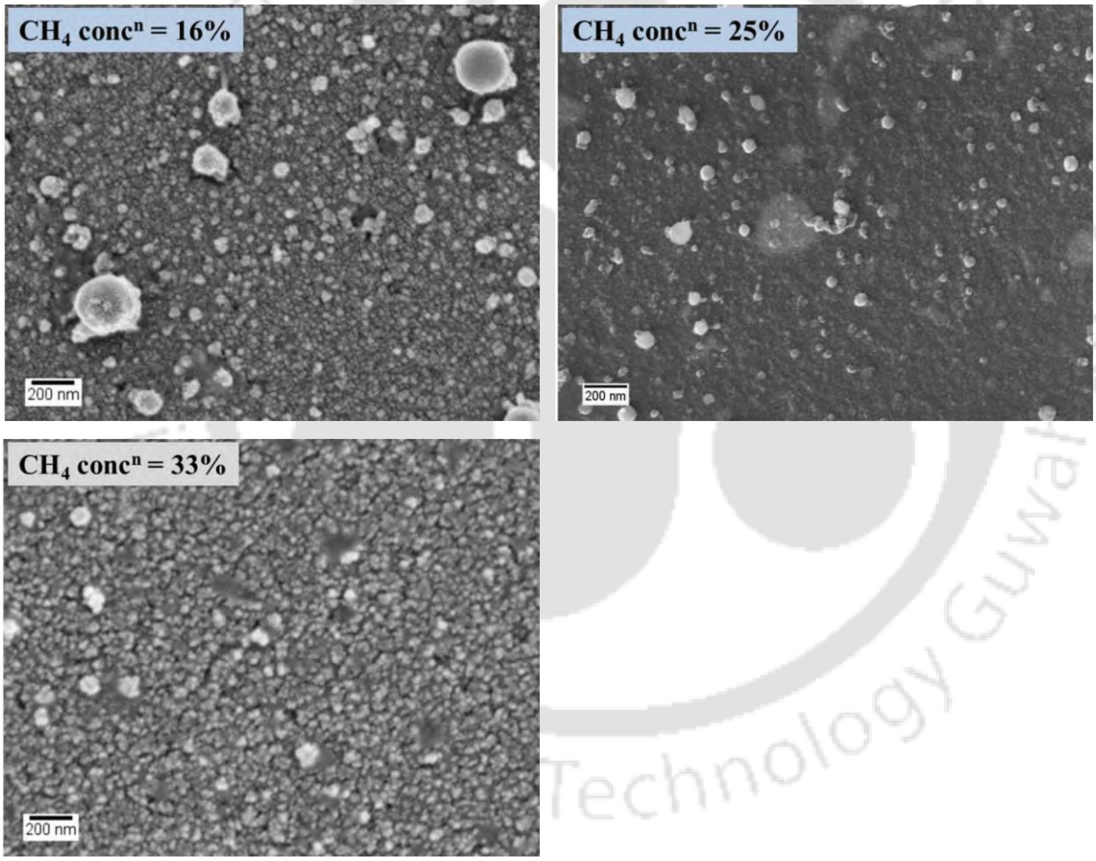

Figure 3.6: *FESEM image of DLC thin films on ITO coated glass substrate at different CH$_4$ concentration of 16%, 25% and 33%.*

3.3.ii Raman scattering

Figure 3.7 shows the Raman spectra of DLC thin films on ITO coated glass substrate with different methane concentration of 13%, 16%, 25%, 33%, 41% and 66%. Films were characterized with excitation laser wavelength of 488 nm. All measured Raman spectra are deconvoluted using Lorentzian fit into five common peaks and corresponding center peak position, FWHM, peak intensity and integrated area are listed in table 3.3. The characteristic of all the peaks are discussed in previous sections. Deconvoluted Raman spectra show that FWHM of the peak centered at 1330 cm^{-1} is in the range of 100 – 220 cm^{-1}. Large FWHM of the peak at 1330 cm^{-1} and improvement in the intensity of the peak at 1116 cm^{-1} indicate that films deposited on ITO coated glass substrate have higher density of sp^3 bonded carbon atoms in comparison to films on Si substrate [19, 27, 28]. The relative fractions of sp^3 bonded carbon atoms are calculated using peak intensity, integrated area and also after taking into account of 50% cross-section integrated area of sp^2 sites and the values are listed in table 3.3. The calculated value of sp^3 fraction, using 50% cross section of sp^2 sites, is in the range of 60 – 75%, which is ~ 10% higher as compared to films deposited on Si substrate. Figure 3.8 shows the fraction of sp^3 bonded carbon atoms as a function of methane concentration for films deposited on ITO coated glass and Si substrates.

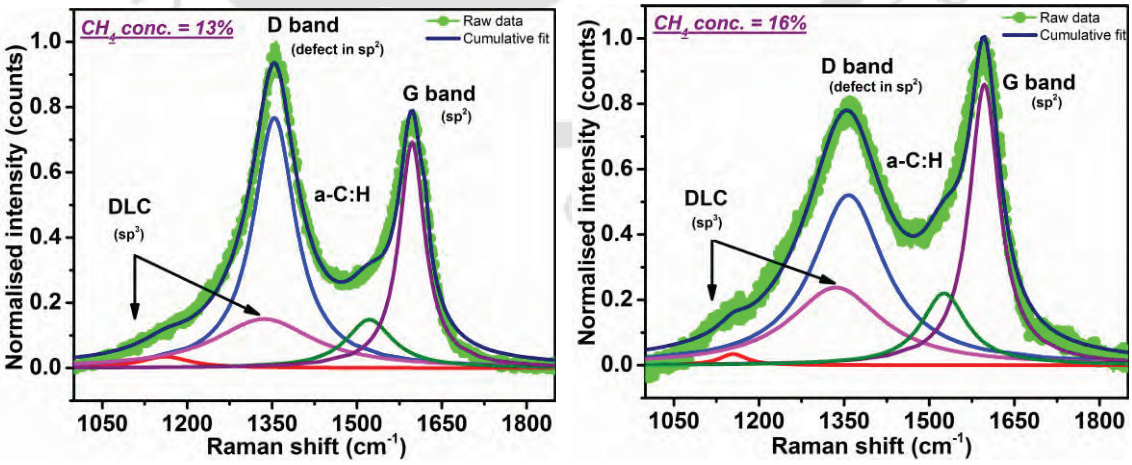

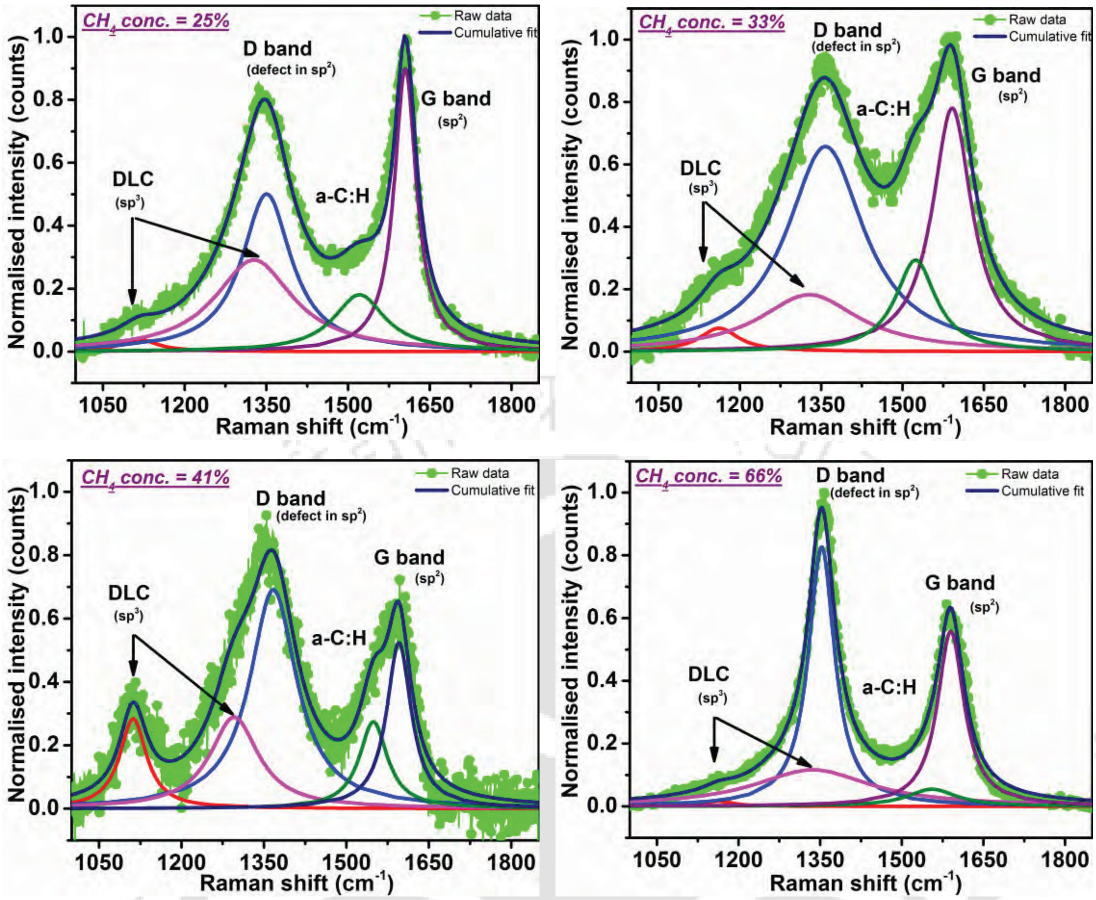

__Figure 3.7:__ Deconvoluted Raman spectra of DLC thin films on ITO coated glass substrate at different methane concentrations of 13%, 16%, 25%, 33%, 41% and 66%.

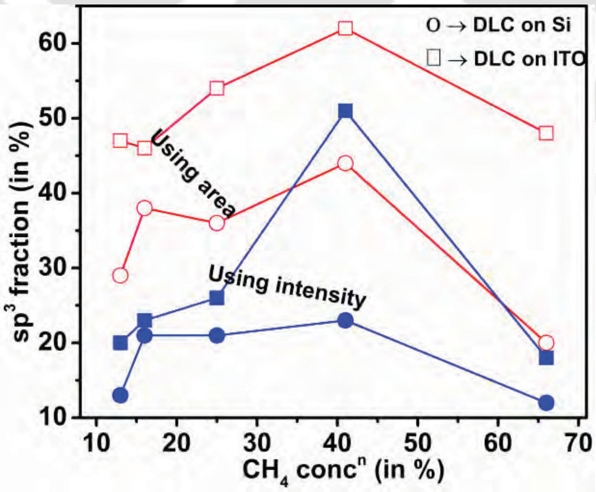

***Figure 3.8:** sp^3 fraction of carbon bonded atoms in DLC for the films deposited on heavily doped Si and ITO coated glass substrates (filled symbol for intensity and open symbol for area of the peak).*

Table 3.3: FWHM, peak intensity and integrated area of the peaks and calculated relative fractions of sp^3 bonded carbon atoms for DLC films on ITO coated glass substrate.

Samples	DLC (sp^3) (~ 1116 cm^{-1}) (FWHM/peak intensity/Int. area)*	DLC (sp^3) (~ 1330 cm^{-1}) (FWHM/peak intensity/Int. area)	D band (~ 1355 cm^{-1}) (FWHM/peak intensity/Int. area)	G band (sp^2) (~ 1596 cm^{-1}) (FWHM/peak intensity/Int. area)	Sp^3/(sp^2+sp^3) % (using peak intensity)	Sp^3/(sp^2+sp^3) % (using Int. area)	Sp^3/(sp^2+sp^3)% (using Int. area) (50% cross-section of sp^2 sites)
CH$_4$ conc^n = 13%	106/0.03 / 5	212/0.15 / 50	91/ 0.76 / 109	55/ 0.69 / 60	**20**	**47**	**64**
CH$_4$ conc^n = 16%	59/ 0.03 / 3	196/0.23 / 73	153/0.52 / 125	64/ 0.85 / 86	**23**	**46**	**63**
CH$_4$ conc^n = 25%	82/ 0.03/ 4	174/0.29 / 79	110/0.50 / 86	49/ 0.89 / 70	**26**	**54**	**70**
CH$_4$ conc^n = 33%	87 /0.07 / 10	223/0.18 / 63	173/0.65 / 178	88/ 0.77 / 108	**24**	**40**	**57**
CH$_4$ conc^n = 41%	59/ 0.28 / 26	107/0.28 / 48	103/0.69 / 112	54/ 0.52 / 44	**51**	**62**	**77**
CH$_4$ conc^n = 66%	66/ 0.01 / 1	260/0.11 / 47	58/ 0.82 / 76	59/ 0.55 / 52	**18**	**48**	**64**

* Int. area = Integrated area

3.4 Conclusion

Diamond like carbon thin films were deposited by HFCVD method on p-type Si and ITO coated glass substrates at low T$_S$ of 450 ^{o}C. This chapter presents the influence of methane concentration on the growth of sp^3 bonded carbon atoms. Structural properties of the films were investigated by FESEM, Raman scattering, XRD, AFM and TEM studies. We have observed that in case of DLC films on Si substrate, fraction of sp^3 bonded carbon atoms is increased from ~ 29% to 44% (from integrated area) with increase in methane concentration from 13 to 41%. However, at high methane concentration of 66%, growth of flakes type structure is also increased along with the formation of nano-diamond particles, which results in the enhancement of sp^2 sites in Raman spectra resulting in decrease in fraction of sp^3 bonded carbon atoms. In case of films deposited on ITO coated glass substrate, the fraction of sp^3 bonded carbon atoms is more by ~ 10% in comparison to films on Si substrate. These results suggest that metallic substrate acts as catalyst for the growth of diamond like carbon films. The increase in fraction of sp^3 bonded carbon is also confirmed by the increase in density of diamond nano-particles by FESEM image with increasing methane concentration.

3.5 References

[1] O.A. Williams, Nanocrystalline diamond, Diamond and Related Materials, 20 (2011) 621-640.

[2] S.T. Lee, Z. Lin, X. Jiang, CVD diamond films: nucleation and growth, Materials Science and Engineering: R: Reports, 25 (1999) 123-154.

[3] D.S. Dandy, M.E. Coltrin, Effects of temperature and filament poisoning on diamond growth in hot-filament reactors, Journal of Applied Physics, 76 (1994) 3102-3113.

[4] B.V. Spitsyn, L.L. Bouilov, B.V. Derjaguin, Vapor growth of diamond on diamond and other surfaces, Journal of Crystal Growth, 52, Part 1 (1981) 219-226.

[5] T. Wang, H.W. Xin, Z.M. Zhang, Y.B. Dai, H.S. Shen, The fabrication of nanocrystalline diamond films using hot filament CVD, Diamond and Related Materials, 13 (2004) 6-13.

[6] J.E. Butler, Y.A. Mankelevich, A. Cheesman, M. Jie, M.N.R. Ashfold, Understanding the chemical vapor deposition of diamond: recent progress, Journal of Physics: Condensed Matter, 21 (2009) 364201.

[7] B.N. Jariwala, C.V. Ciobanu, S. Agarwal, Atomic hydrogen interactions with amorphous carbon thin films, Journal of Applied Physics, 106 (2009) 073305.

[8] M. Schwander, K. Partes, A review of diamond synthesis by CVD processes, Diamond and Related Materials, 20 (2011) 1287-1301.

[9] H. Liu, D.S. Dandy, Studies on nucleation process in diamond CVD: an overview of recent developments, Diamond and Related Materials, 4 (1995) 1173-1188.

[10] T. Hao, H. Zhang, C. Shi, G. Han, Nano-crystalline diamond films synthesized at low temperature and low pressure by hot filament chemical vapor deposition, Surface and Coatings Technology, 201 (2006) 801-806.

[11] C. Popov, W. Kulisch, P.N. Gibson, G. Ceccone, M. Jelinek, Growth and characterization of nanocrystalline diamond/amorphous carbon composite films prepared by MWCVD, Diamond and Related Materials, 13 (2004) 1371-1376.

[12] J.E. Gerbi, J. Birrell, M. Sardela, J.A. Carlisle, Macrotexture and growth chemistry in ultrananocrystalline diamond thin films, Thin Solid Films, 473 (2005) 41-48.

[13] J. Birrell, J.E. Gerbi, O. Auciello, J.M. Gibson, J. Johnson, J.A. Carlisle, Interpretation of the Raman spectra of ultrananocrystalline diamond, Diamond and Related Materials, 14 (2005) 86-92.

[14] R.E. Shroder, R.J. Nemanich, J.T. Glass, Analysis of the composite structures in diamond thin films by Raman spectroscopy, Physical Review B, 41 (1990) 3738-3745.

[15] B. Marcus, L. Fayette, M. Mermoux, L. Abello, G. Lucazeau, Analysis of the structure of multi-component carbon films by resonant Raman scattering, Journal of Applied Physics, 76 (1994) 3463-3470.

[16] L.C. Nistor, J. Van Landuyt, V.G. Ralchenko, E.D. Obraztsova, A.A. Smolin, Nanocrystalline diamond films: transmission electron microscopy and Raman spectroscopy characterization, Diamond and Related Materials, 6 (1997) 159-168.

[17] R.J. Nemanich, J.T. Glass, G. Lucovsky, R.E. Shroder, Raman scattering characterization of carbon bonding in diamond and diamondlike thin films, Journal of Vacuum Science & Technology A, 6 (1988) 1783-1787.

[18] H. Kuzmany, R. Pfeiffer, N. Salk, B. Günther, The mystery of the 1140 cm^{-1} Raman line in nanocrystalline diamond films, Carbon, 42 (2004) 911-917.

[19] A. Grill, Diamond-like carbon: state of the art, Diamond and Related Materials, 8 (1999) 428-434.

[20] S. Sharma, G. Kalita, R. Hirano, Y. Hayashi, M. Tanemura, Influence of gas composition on the formation of graphene domain synthesized from camphor, Materials Letters, 93 (2013) 258-262.

[21] Z. Sun, J.R. Shi, B.K. Tay, S.P. Lau, UV Raman characteristics of nanocrystalline diamond films with different grain size, Diamond and Related Materials, 9 (2000) 1979-1983.

[22] K. Okada, Plasma-enhanced chemical vapor deposition of nanocrystalline diamond, Science and Technology of Advanced Materials, 8 (2007) 624-634.

[23] J. Robertson, Diamond-like amorphous carbon, Materials Science and Engineering: R: Reports, 37 (2002) 129-281.

[24] S. Prawer, K.W. Nugent, D.N. Jamieson, J.O. Orwa, L.A. Bursill, J.L. Peng, The Raman spectrum of nanocrystalline diamond, Chemical Physics Letters, 332 (2000) 93-97.

[25] S.R. Sails, D.J. Gardiner, M. Bowden, J. Savage, D. Rodway, Monitoring the quality of diamond films using Raman spectra excited at 514.5 nm and 633 nm, Diamond and Related Materials, 5 (1996) 589-591.

[26] C. Wei, J.-Y. Yen, Effect of film thickness and interlayer on the adhesion strength of diamond like carbon films on different substrates, Diamond and Related Materials, 16 (2007) 1325-1330.

[27] Y. Huang, Q. Wang, M. Wang, M. Li, Radio-frequency Power Graded Hydrogenated Amorphous Carbon Films on Diverse Substrates, International Journal of Material Science, 2 (2012) 10-14.

[28] M. Amaral, A.J.S. Fernandes, M. Vila, F.J. Oliveira, R.F. Silva, Growth rate improvements in the hot-filament CVD deposition of nanocrystalline diamond, Diamond and Related Materials, 15 (2006) 1822-1827.

Chapter 4

Vertically Aligned Carbon Nanoflakes Thin Films

In this chapter, structural, optical (linear/nonlinear) and electrical properties of vertically aligned carbon nanoflakes (CNF) thin films deposited by hot filament chemical vapor deposition (HFCVD) are studied in details. The changes in microstructural properties are studied by varying process pressure (PP) at different substrate temperature (T_S). Microstructural properties of the films are studied using field emission scanning electron microscopy (FESEM), atomic force microscopy (AFM), Raman scattering and transmission electron microscopy (TEM). Optical and electrical properties of the films are studied using UV-Vis-NIR spectroscopy (linear) / Z-scan (nonlinear) technique and I-V measurements using two probes respectively.

4.1 Experimental details

To study the microstructural properties, a series of films were deposited on p-type Si (100) substrate (resistivity, 0.001 – 0.006 ohm cm) by varying process pressure at two different substrate temperatures of 600 and 800 °C. To study the optical and electrical properties of CNF, films were deposited on corning 1737 glass substrate at low T_S of 400 °C and simultaneously on p-type Si (100) substrate for the comparison of microstructural properties on different substrates. Since corning 1737 glass substrate cannot sustain high temperature, therefore we have chosen low substrate temperature for the growth of CNF on corning glass substrate. Filament temperature and filament to substrate distance were kept at 2100±50 ^{o}C and 1.5 cm respectively during the deposition of the films. Filament temperature was measured using pyrometer by focusing at the center of tungsten filament. Other deposition parameters such as process pressure, CH_4/H_2 gas flow rate and deposition time (t_d) are listed in table 4.1. We have used nomenclature for the samples in the following manner; Subst._T_S_PP corresponding to films deposited on different substrates at different T_S and PP.

Table 4.1: Deposition parameters for the growth of CNF thin films.

Samples	Nomenclature (Subst.*_T_S_PP)	T_S (^{o}C)	PP (mbar)	CH_4 (sccm)	H_2 (sccm)	Deposition time (min)	CH_4 (%)	H_2 (%)
PP variation at T_S of 600 ^{o}C								
HW151	Si_600_1	600	1	15	5	10	75	25
HW153	Si_600_3	600	3	15	5	10	75	25
HW150	Si_600_5	600	5	15	5	10	75	25
HW154	Si_600_7	600	7	15	5	10	75	25
PP variation at T_S of 800 ^{o}C								
HW158	Si_800_1	800	1	15	5	5	75	25
HW159	Si_800_2	800	2	15	5	5	75	25
Substrate effect at T_S of 400 ^{o}C								
HW96_C	C_400_2	400	2	7	7	20	50	50
HW97_C	C_400_3	400	3	7	10	20	41	69
HW96_S	Si_400_2	400	2	7	7	20	50	50
HW97_S	Si_400_3	400	3	7	10	20	41	69

* Subst. = Substrates

4.2 Structural Properties of carbon nanoflakes thin films

4.2.1 Influence of process pressure at different T_S

To investigate the influence of process pressure on the growth of vertically aligned CNF, a series of films were deposited on p-type Si (100) substrate by varying process pressure at two different T_S of 600 and 800 ^{o}C. Microstructural properties of the films are studied using different characterization techniques in the following sections.

4.2.1.i FESEM

Figure 4.1 shows the FESEM images of vertically aligned CNF (front view) on Si substrate deposited at different PP of 3, 5 and 7 mbar at fixed T_S of 600 ^{o}C. The alignment of CNF in vertical direction is confirmed from cross-sectional view of FESEM image and three dimensional AFM image of CNF, as discussed in next section. From FESEM image, it is clear that alignment of flakes is more uniform for the films deposited at PP of 3 and 5 mbar in comparison to films at PP of 7 mbar. The lateral size of the flakes is in the range of 20 – 30 and 50 – 90 nm for the films deposited at PP of 3 and 5 mbar respectively. This indicates that with increasing process pressure, the lateral size of the flakes is increased. However, as the process pressure is increased to 7 mbar, the lateral size of the flakes is decreased to 10 – 30 nm. The reason of decrease in lateral size of the flakes at PP of 7 mbar could be due to the non-uniform orientation of the flakes caused by high density of island growth at the primary stage of nucleation [1-3]. There is no significant change in the width of the flakes with the variation of process pressure and it is in the range of 8 – 12 nm for all the films. The height of the flakes (i.e. thickness of the films) is not uniform throughout the surface of the films. Thickness of the films as measured by stylus profilometer is listed in table 4.2. Height of the flakes is slightly increased with increasing process pressure, but it is difficult to distinguish the height of the flakes for the films deposited at different process pressure due to low thickness of the films. The growth mechanism of vertically aligned CNF is proposed in the light of Stranski-Krastanov model [4]. In this growth model, a layer of nanoislands with dangling bonds nucleates on the substrate surface, which acts as nucleation sites for the growth of carbon nanoflakes. At these nucleation sites, carbon nanoflakes of smaller sizes would be nucleated, followed by two dimensional growth in a wall type structure. Among nucleated wall structures with random orientations, those standing almost vertically on the substrate surface, continue to grow faster in upward direction (i.e. along the strongly bonded planes of vertically aligned graphene sheets rather than weakly bonded stacking direction). Therefore, with the increase in time of deposition, the activated carbon species arrive at the top of the larger walls in comparison to smaller walls due to shadow effect. As a results, only larger walls grow further and vertically aligned carbon nanoflakes are formed [2, 5, 6].

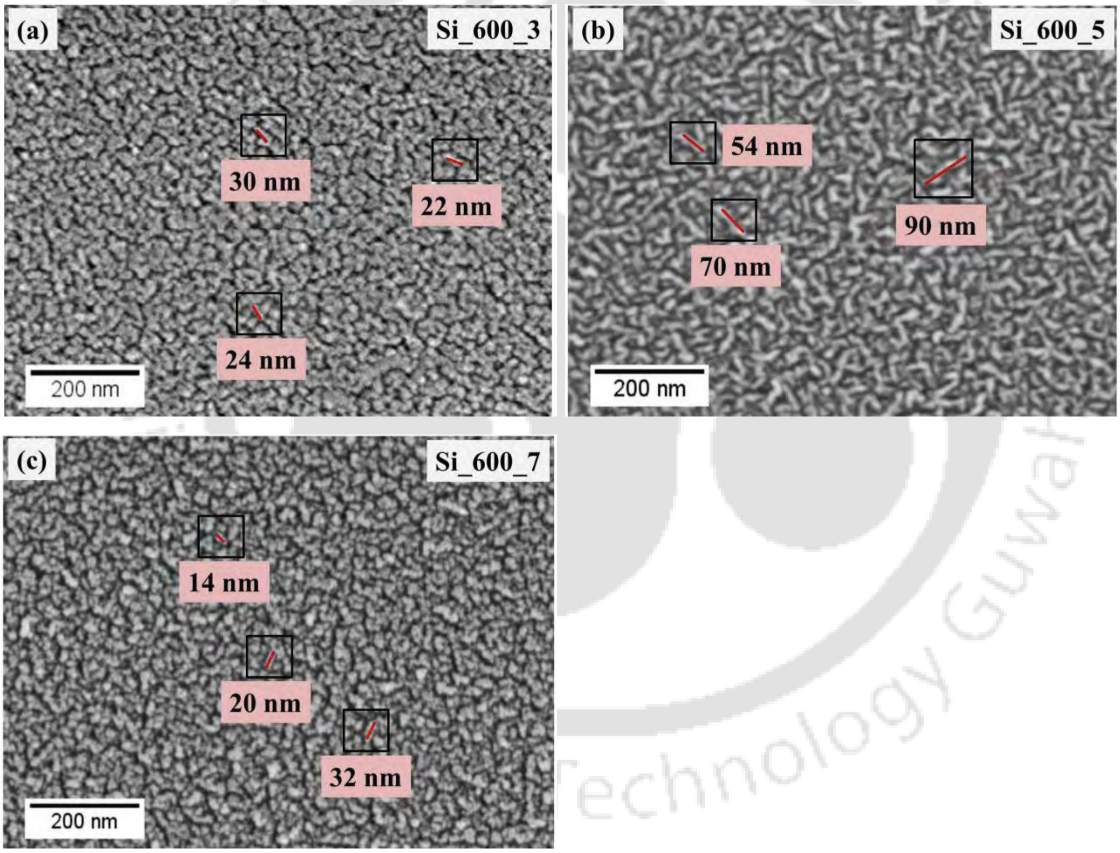

Figure 4.1: *FESEM image of CNF (front view) deposited on Si substrate at different PP of (a) 3 mbar, (b) 5 mbar and (c) 7 mbar at* T_S *of 600* ^oC.

Figure 4.2 shows the FESEM images of cross-sectional view of CNF as deposited on Si substrate at different PP of 5 and 7 mbar. Thickness of the films (i.e. height of the flakes) as measured from FESEM image is 35 nm and 75 nm for the films deposited at PP of 5 and 7 mbar respectively, which is also consistent with the measured thickness of the films using stylus profilometer as listed in table 4.2.

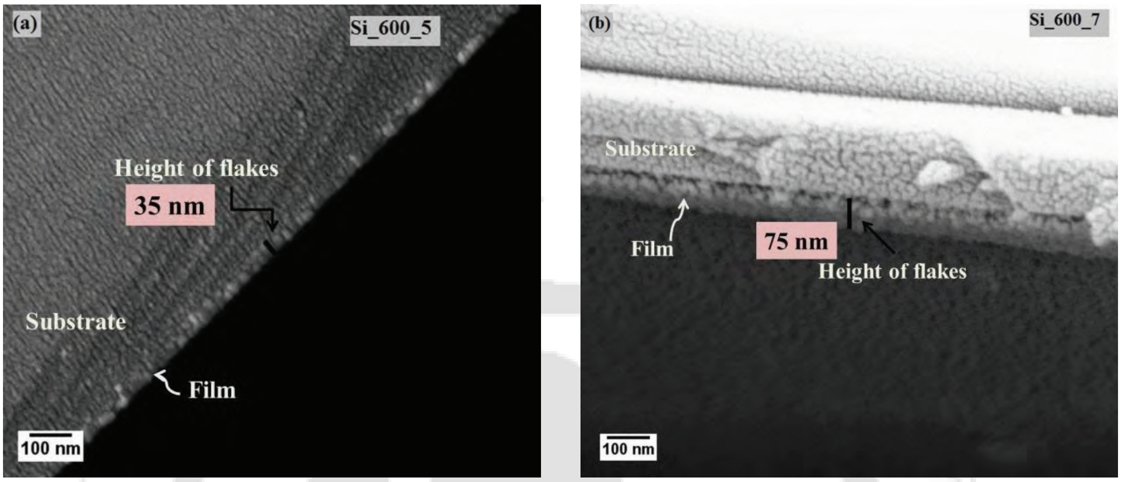

Figure 4.2: *FESEM image of CNF (cross-sectional view) deposited on Si substrate at different PP of (a) 5 mbar and (b) 7 mbar.*

Figure 4.3 shows the FESEM image of CNF, front and cross-sectional view, for the films deposited at PP of 2 mbar and T_S of 800 ^oC. The height of the flakes is approximately 60 ± 6 nm, as measured by stylus profilometer, which is consistent with the cross-sectional view of FESEM image. This shows that with increasing substrate temperature, height of the flakes is increased. The lateral size and width of the flakes are in the range of 15 – 30 nm and 5 – 10 nm. The increase in height of the flakes (i.e. thickness of the films) with increasing substrate temperature could be due to high surface energy which helps in the fast growth of nanoislands at the primary stage of nucleation, which results in the increase in growth rate of height of the flakes at T_S of 800 ^oC in comparison to 600 ^oC [7]. The increase in height of the flakes with increasing substrate temperature is also observed by Kim et al. [7] and Wang et al. [8] as reported in literature.

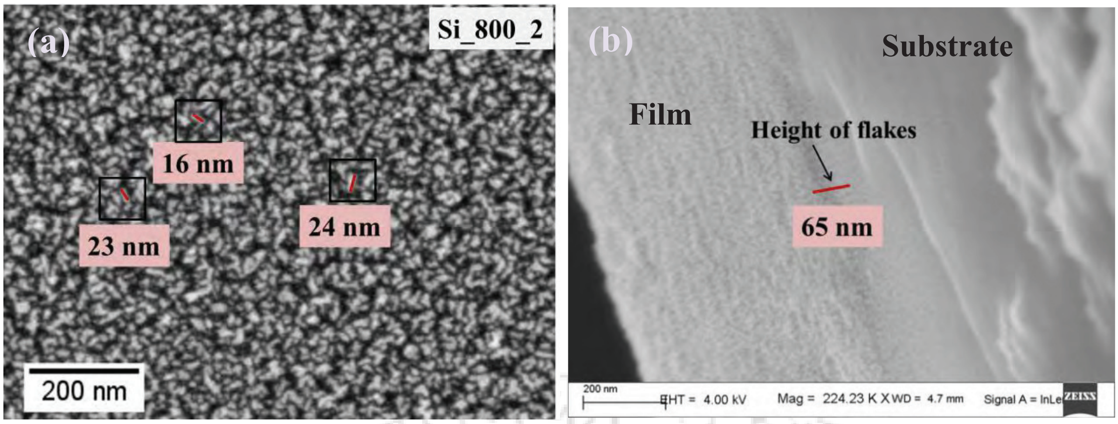

Figure 4.3: *FESEM image of CNF (a) front view and (b) cross-sectional view for the film deposited on Si substrate at PP of 2 mbar and* T_S *of 800* °*C.*

4.2.1.ii AFM

Figure 4.4 shows the AFM images and corresponding surface height profile of CNF on Si substrate at different PP of 3 and 7 mbar at fixed T_S of 600 °C.

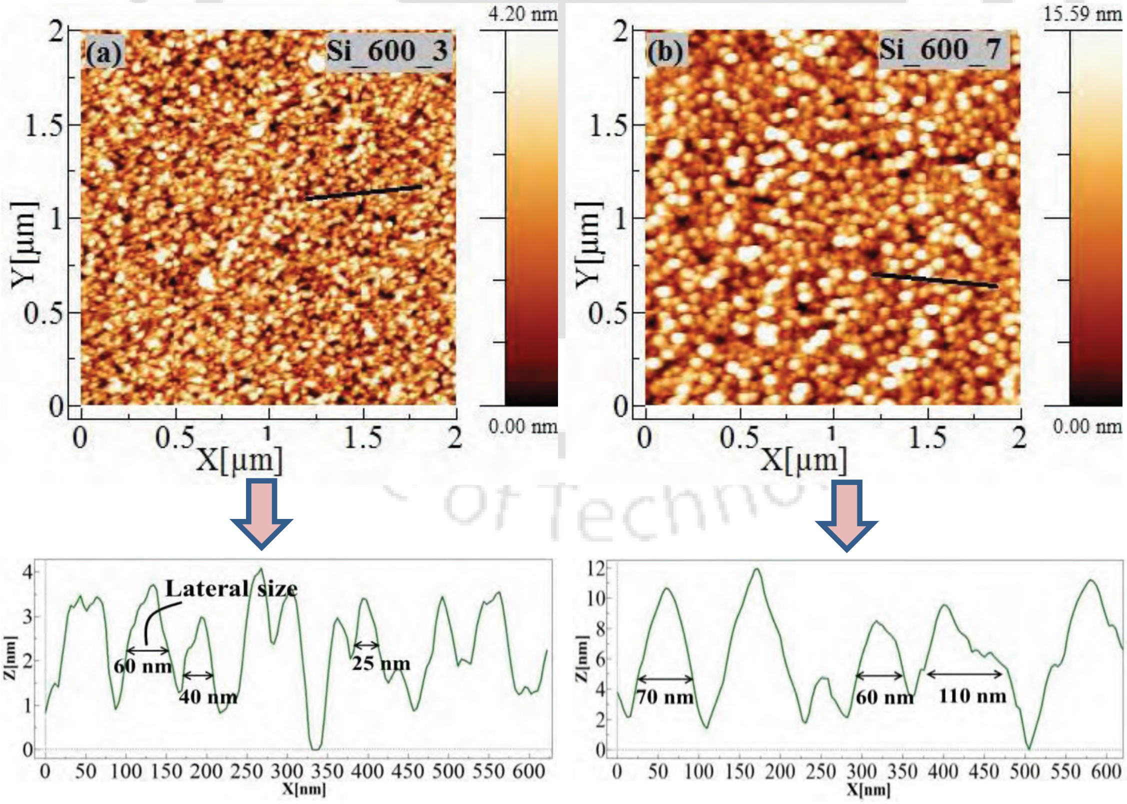

Figure 4.4: *AFM images and corresponding surface height profile of CNF on Si substrate at different PP of (a) 3 mbar and (b) 7 mbar at* T_S *of 600* °*C.*

AFM images show the uniform growth of high density carbon nanoflakes over entire area of the substrates. The average roughness of the films as measured from AFM image is 0.96 and 3.63 nm for the films deposited at different PP of 3 and 7 mbar respectively. AFM images also confirm the increase in lateral size of the flakes with increasing process pressure, as we can see from the surface height profile of AFM image. These surface height profiles show that lateral size of the flakes for the films deposited at PP of 3 mbar approximately is in the range of 25 – 60 nm and lateral size of the flakes is increased to approximately 60 – 110 nm with increase in process pressure to 7 mbar.

Figure 4.5 shows the AFM image and corresponding surface height profile of CNF on Si substrate at PP of 2 mbar and T_S of 800 °C.

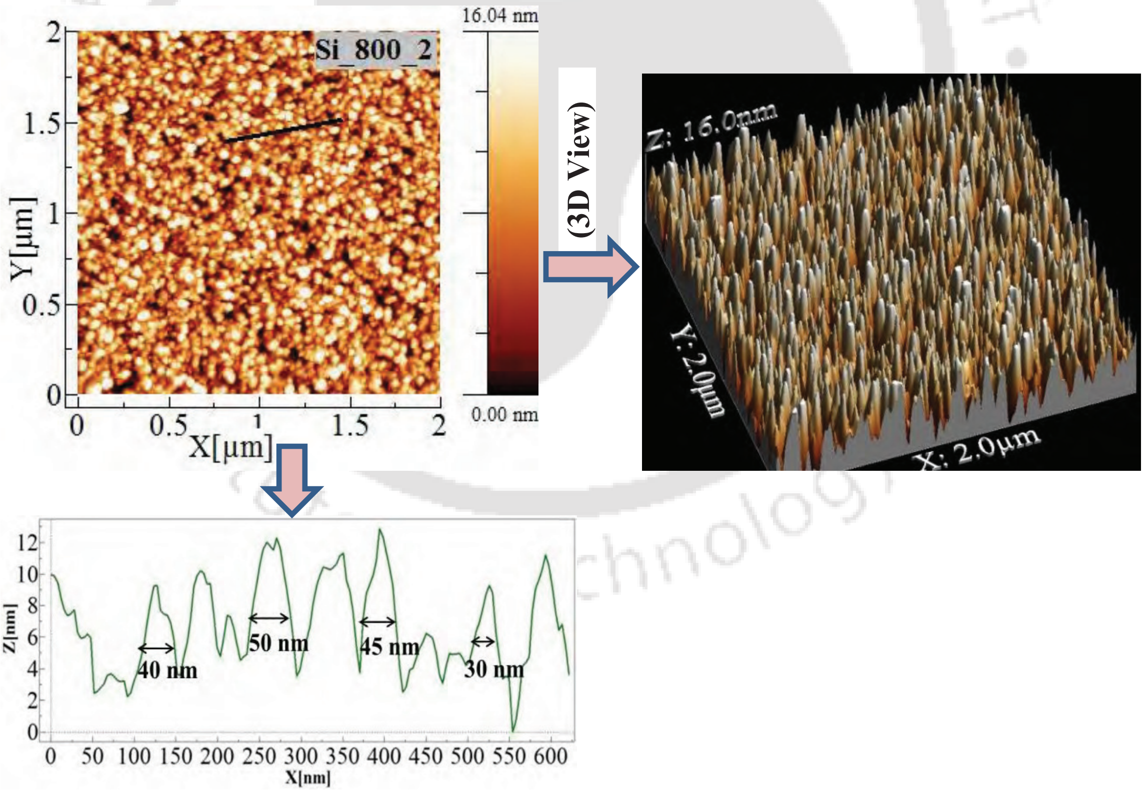

Figure 4.5: *AFM image and corresponding surface height profile of CNF deposited on Si substrate at PP of 2 mbar and T_S of 800 °C (3D view of AFM image is also shown here for the visualization of vertically aligned CNF).*

For the visualization of vertical growth of flakes, 3D view of the AFM image is also shown here. The lateral size of the flakes, from the surface height profile, is in the range of 30 – 50 nm. The average roughness of the film is 3.83 nm, which is significantly higher in comparison to films deposited at low T_S of 600 ^{o}C and different PP of 1 and 3 mbar. The increase in roughness at T_S of 800 ^{o}C indicates that height of the flakes is higher in comparison to films deposited at low T_S of 600 ^{o}C. These results indicate that growth rate of CNF for the films deposited at T_S of 800 ^{o}C are higher in comparison to films deposited at low T_S of 600 ^{o}C.

4.2.1.iii Raman scattering

Raman spectroscopy is an important nondestructive characterization technique for carbon based materials to determine the crystallinity, average grain size, defects, etc. Raman spectra of all the samples were recorded with an excitation wavelength of 514.53 nm. Figure 4.6 shows the Raman spectra of CNF on Si substrate at different PP of 1, 3, 5 and 7 mbar at fixed T_S of 600 ^{o}C. The prominent characteristic peaks are observed at approximately 1351 cm^{-1} (D band), 1603 cm^{-1} (G band), 2703 cm^{-1} (2D band), 2946 cm^{-1} (D+G band) and 3219 cm^{-1} (2D'/G+D' band). G band is Raman active for sp^{2} bonded carbon networks, whereas, D band represents the defect induced Raman features which is due to defects in hexagonal structure as well as from the edges of the flakes [9, 10].

In order to find the different bonding modes between the carbon atoms, Raman spectra are deconvoluted in the range of 1000 – 1900 cm^{-1} into five Lorentzian peaks including D and G band, as shown in figure 4.7. Two broad peaks with small intensity at 1200 and 1530 cm^{-1} could be due to the amorphous phase of the films [11, 12]. In addition, a weak D' band is also observed at 1620 cm^{-1} which appears in graphite like carbon such as nanocrystalline graphite with low disorder [8, 10, 13, 14].

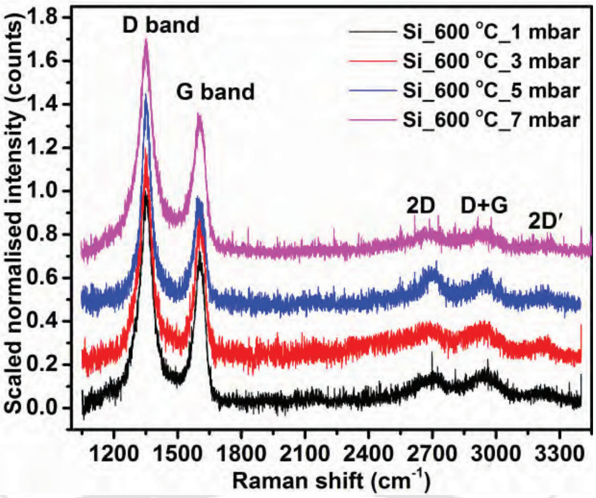

Figure 4.6: *Raman spectra of CNF on Si substrate at different PP of 1, 3, 5 and 7 mbar at* T_S *of 600 °C.*

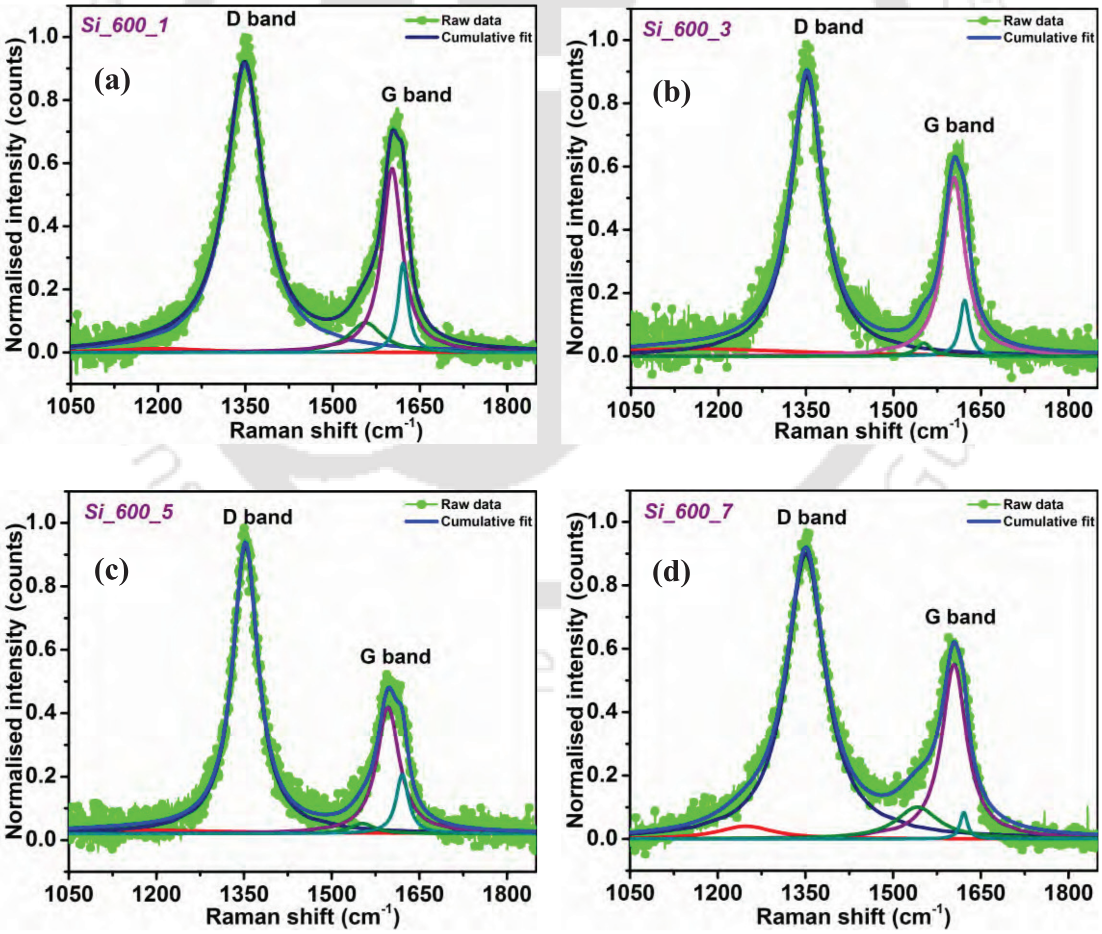

Figure 4.7: *Deconvoluted Raman spectra of CNF on Si substrate at different PP of (a) 1 mbar, (b) 3 mbar, (c) 5 mbar and (d) 7 mbar at* T_S *of 600 °C.*

The peak intensity ratio I_D/I_G and FWHM of D and G bands are widely used for determining the density, defects and average width of the flakes [6, 10, 13-16]. The peak intensity ratio I_D/I_G is 1.56, 1.58, 2.30 and 1.61 for the films deposited at different PP of 1, 3, 5 and 7 mbar respectively. The peak intensity ratio I_D/I_G is increasing with increasing PP from 1 to 5 mbar and with further increase in PP to 7 mbar, a decrease in peak intensity ratio I_D/I_G is observed. The increase in peak intensity ratio I_D/I_G is due to increases in number of edges (i.e. benzene rings separated by defects), in other words due to increase in the density of the flakes. Therefore, we have observed that with increasing process pressure, density of CNF is increased. The decrease in peak intensity ratio I_D/I_G at 7 mbar is probably due to non-uniform orientation of the flakes, which can be seen in figure 4.1(c) (section 4.2.1). The average flakes size is related to peak intensity ratio I_D/I_G [17-19] and is calculated using Tuinstra-Koenig empirical relation [20];

$$L_a = (2.4 \times 10^{-10})\lambda^4 \left(\frac{I_D}{I_G}\right)^{-1} \quad \ldots\ldots\ldots\ldots\ldots\ldots\ldots\ldots\ldots\ldots\ldots\ldots \quad (4.1)$$

λ (in nm) is the laser wavelength. L_a (in nm) represents the average width of the flakes for vertically aligned CNF. The average width of the flakes (calculated from Tuinstra-Koenig relation) is ~ 10.7, 10.6, 7.3, 10.4 nm for the films deposited at PP of 1, 3, 5 and 7 mbar respectively, which is consistent with the observed width of the flakes (~ 8 – 12 nm) from FESEM image. From the deconvoluted Raman spectra (figure 4.7), FWHM of D band is found to be 77, 67, 53 and 80 cm^{-1} for the films deposited at PP 1, 3, 5 and 7 mbar respectively, whereas, no significant change in FWHM of G band is observed. FWHM of G band is 41, 45, 46 and 51 cm^{-1} for the films deposited at PP 1, 3, 5 and 7 mbar respectively. The decrease in FWHM of D band with increasing PP from 1 to 5 mbar could be due to the increase in lateral size of the flakes with increasing PP and with further increase in PP to 7 mbar, decrease in FWHM of D band is due to the non-uniform growth of the flakes or in other words, decrease in lateral size of the flakes.

Figure 4.8 shows the deconvoluted Raman spectra of CNF on Si substrate at different PP of 1 and 2 mbar and fixed T_S of 800 °C. The peak intensity ratio I_D/I_G is 2.04, 2.06 for the films deposited at PP of 1 and 2 mbar respectively, which is higher in comparison to films deposited at T_S of 600 °C and at different PP of 1 and 3 mbar. This suggests that deposited carbon nanoflakes become more disordered with increasing substrate temperature. The average width of the flakes (calculated using Tuinstra-Koenig relation) is 8.2 and 8.1 nm for the films deposited at PP of 1 and 2 mbar. These results are consistent with the FESEM observations, where decrease in lateral size of the flakes is observed with increasing substrate temperature. The increase in disorder during the formation of the flakes with increasing substrate temperature is also observed by Shang et al. [1] and Wang et al. [8], as reported in literature. The decrease in average width of the flakes at T_S of 800 °C as compared to that of 600 °C could be due to faster growth of the flakes in vertical direction in comparison to planar growth after the island formation. From deconvoluted Raman spectra (figure 4.8), FWHM of D band is 59 and 61 cm^{-1} for the films deposited at PP of 1 and 2 mbar respectively, which is lower (corresponds to 77 cm^{-1}) as compared to films deposited at PP of 1 mbar at T_S 600 °C. FWHM of G band is 48 and 44 cm^{-1} for the films at PP of 1 and 2 mbar respectively. This shows that no significant change in the FWHM of G band is observed in comparison to films deposited at T_S of 600 °C. The peak intensity ratio I_D/I_G, FWHM of D and G band and average flakes size for all the films are listed in table 4.2.

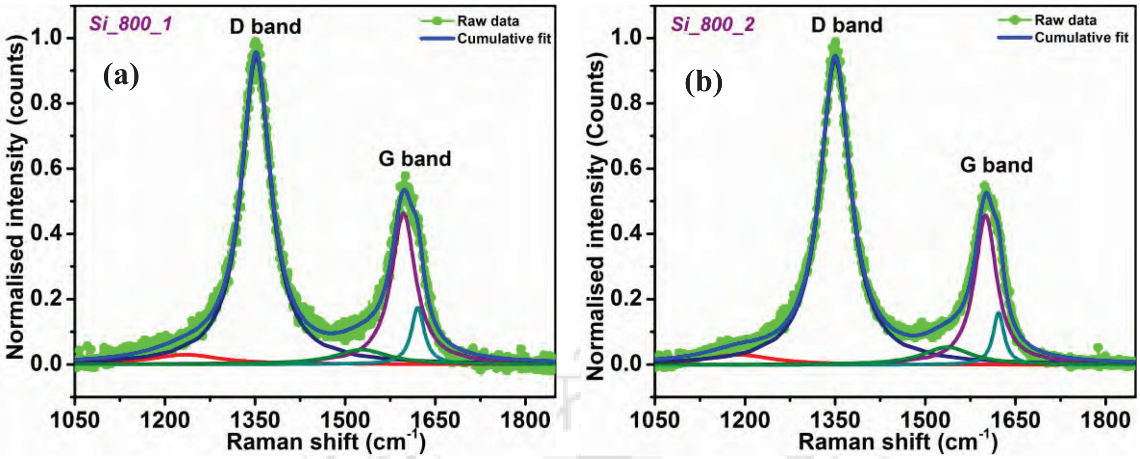

Figure 4.8: *Deconvoluted Raman spectra of CNF on Si substrate at different PP of (a) 1 mbar and (b) 2 mbar at* T_S *of 800* ^{o}C.

4.2.2 Influence of different substrates

For the analysis of growth of CNF on different substrates, films are deposited on corning 1737 glass and p-type Si (100) substrates at low T_S of 400 ^{o}C and at PP of 2 and 3 mbar. From the analysis of microstructural properties of CNF at different process pressure, we have observed that flakes are uniformly oriented in vertical direction at the intermediate PP of 3 to 5 mbar. Therefore, we have chosen 2 and 3 mbar process pressure for the growth of CNF at low T_S of 400 ^{o}C. We have also increased the concentration of H_2 for the removal of undesirable amorphous phase during the growth of films at low substrate temperature, leading to improved surface morphology and crystalline quality of the films. The growth rate of CNF is in the range of 3 – 7 nm/min for the films deposited on Si substrate at T_S of 600 ^{o}C. Therefore, to increase the thickness of the films, deposition time is increased for the films deposited at T_S of 400 ^{o}C.

4.2.2.i FESEM

Figure 4.9 shows the FESEM image of CNF deposited, on corning glass and Si substrates, at PP of 3 mbar and T_S of 400 ^{o}C. From FESEM image, it is clear that CNF can also be deposited on corning glass substrate by optimizing deposition parameter using HFCVD method. The height of the flakes (i.e. thickness of the films) is in the range of 20 – 30 nm and 45 – 55 nm for the films deposited on corning glass and Si substrates respectively, as measured by stylus profilometer.

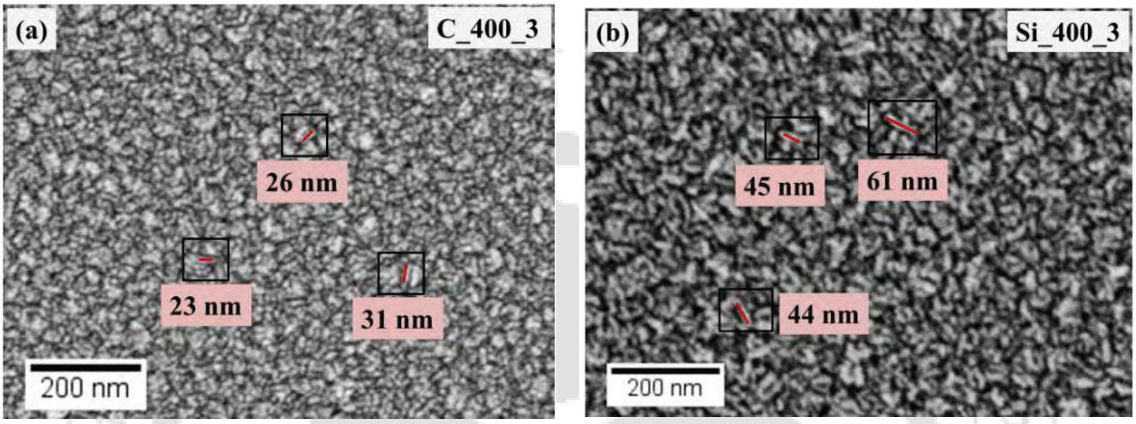

Figure 4.9: *FESEM images of CNF deposited on (a) corning glass and (b) Si substrates at PP of 3 mbar and* T_S *of 400* ^oC*.*

From FESEM image, it is clear that lateral size of the flakes for the films deposited on corning glass substrate are smaller in comparison to films deposited on Si substrate. The reason of comparatively lower growth rate and smaller flake size for the films on corning glass substrate could be the amorphous and insulating nature of substrate which does not favor the nucleation phenomena and delays the process of primary stage of nucleation.

4.2.2.ii AFM

Figure 4.10 shows the AFM image and corresponding surface height profile of CNF on corning glass substrate at PP of 2 and 3 mbar. AFM images also confirm the uniform growth of vertically aligned CNF on corning glass substrate. The average roughness as measured from AFM image is 2.58 and 1.92 nm for the films deposited on corning glass substrate at PP of 2 and 3 mbar respectively. The surface height profiles show that lateral size of the flakes for the films deposited at PP of 2 mbar in the range of 30 – 40 nm which increases to 45 – 70 nm with increase in process pressure to 3 mbar.

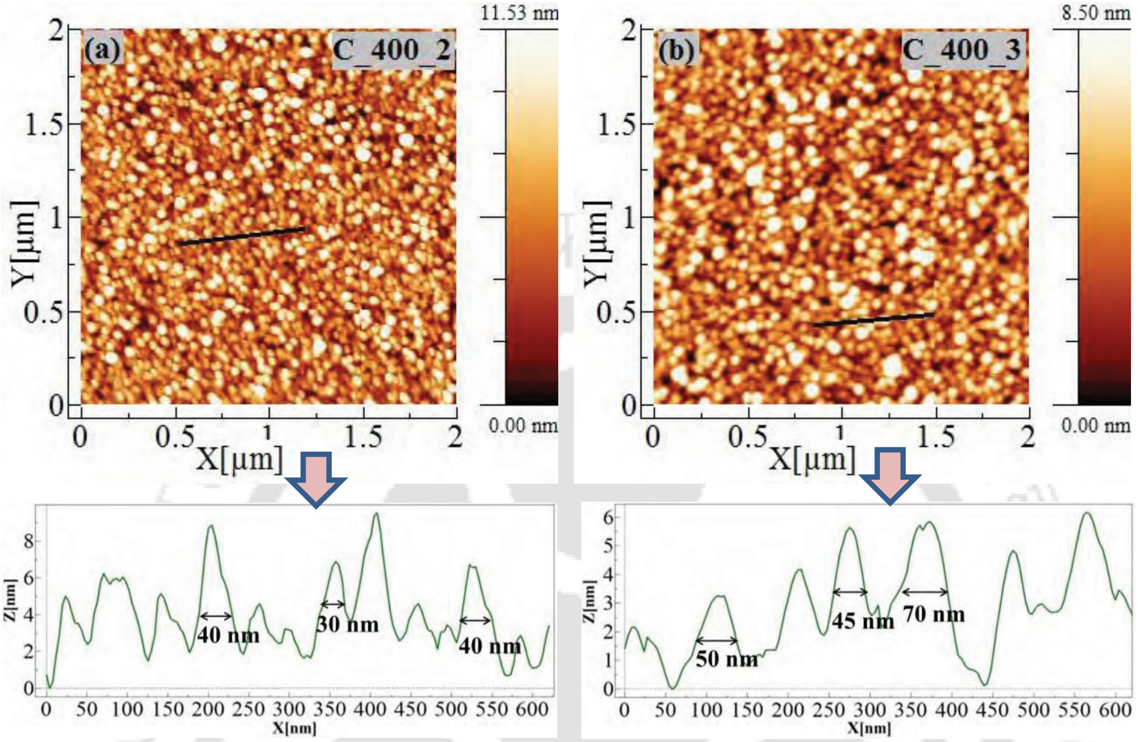

Figure 4.10: *AFM images and corresponding surface height profile of CNF deposited on corning glass substrate at different PP of (a) 2 mbar and (b) 3 mbar at T_S of 400 ^oC.*

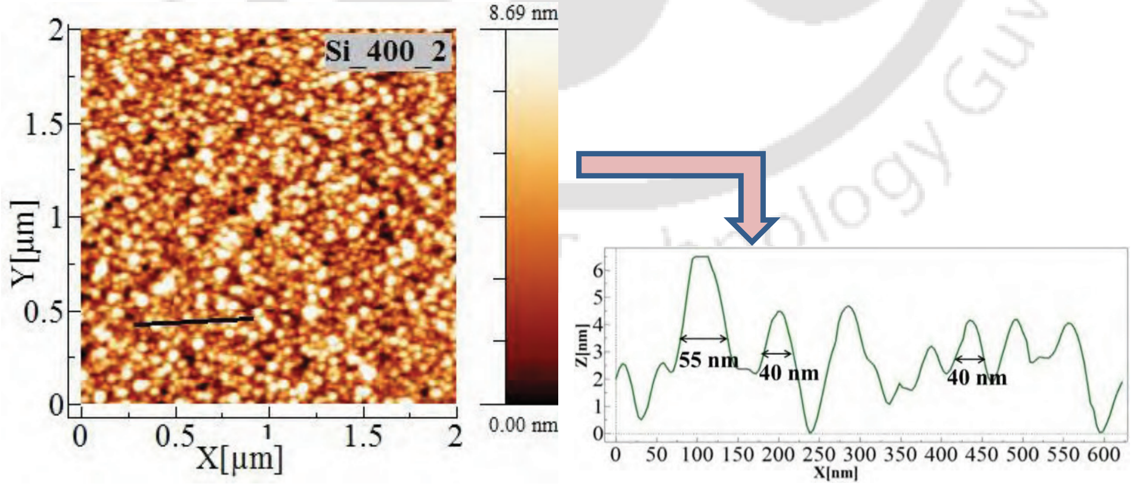

Figure 4.11: *AFM image and corresponding surface height profile of CNF deposited on Si substrate at PP of 2 mbar and T_S of 400 ^oC.*

Figure 4.11 shows the AFM image of CNF and corresponding surface height profile on Si substrate at PP of 2 mbar. The average roughness of films is 2.02 nm for the films deposited at PP of 2 mbar on Si substrate, which is slightly lower in comparison to 2.58 nm for the films deposited at PP of 2 mbar on glass substrate.

4.2.2.iii Raman scattering

Figure 4.12 shows the Raman spectra of CNF on corning glass and Si substrates at different PP of 1 and 2 mbar and at fixed T_S of 400 ^oC. All the characteristics peaks such as D band (1351 cm^{-1}), G band (1603 cm^{-1}), 2D band (2703 cm^{-1}), D+G band (2946 cm^{-1}) and 2D' band (3219 cm^{-1}) are observed in Raman spectra of CNF for the films on both substrates; corning glass as well as Si. Figure 4.13 shows the deconvoluted Raman spectra of CNF in the range of 1000 – 1900 cm^{-1} on corning glass and Si substrates at PP of 2 and 3 mbar. The peak intensity ratio I_D/I_G is 1.16 and 1.29 for the films on corning glass substrate, whereas 1.44 and 1.85 for the films on Si substrate at PP of 2 and 3 mbar respectively. The decrease in peak intensity ratio I_D/I_G for the films on corning glass substrate in comparison to Si could be due to non-uniform orientation of nanoflakes on corning glass substrate, which affects the average width of CNF [21].

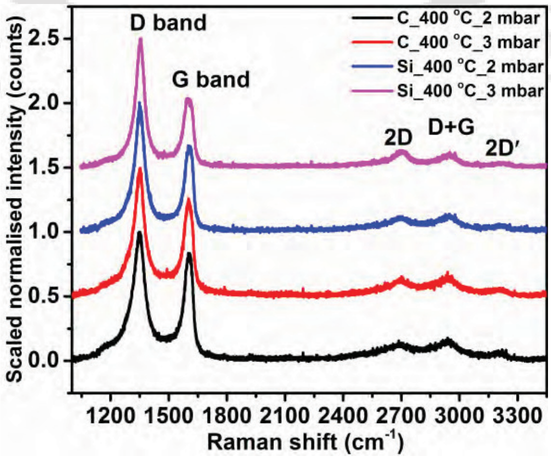

Figure 4.12: *Raman spectra of CNF on corning glass and Si substrates at different PP of 2 and 3 mbar at fixed* T_S *of 400* ^oC.

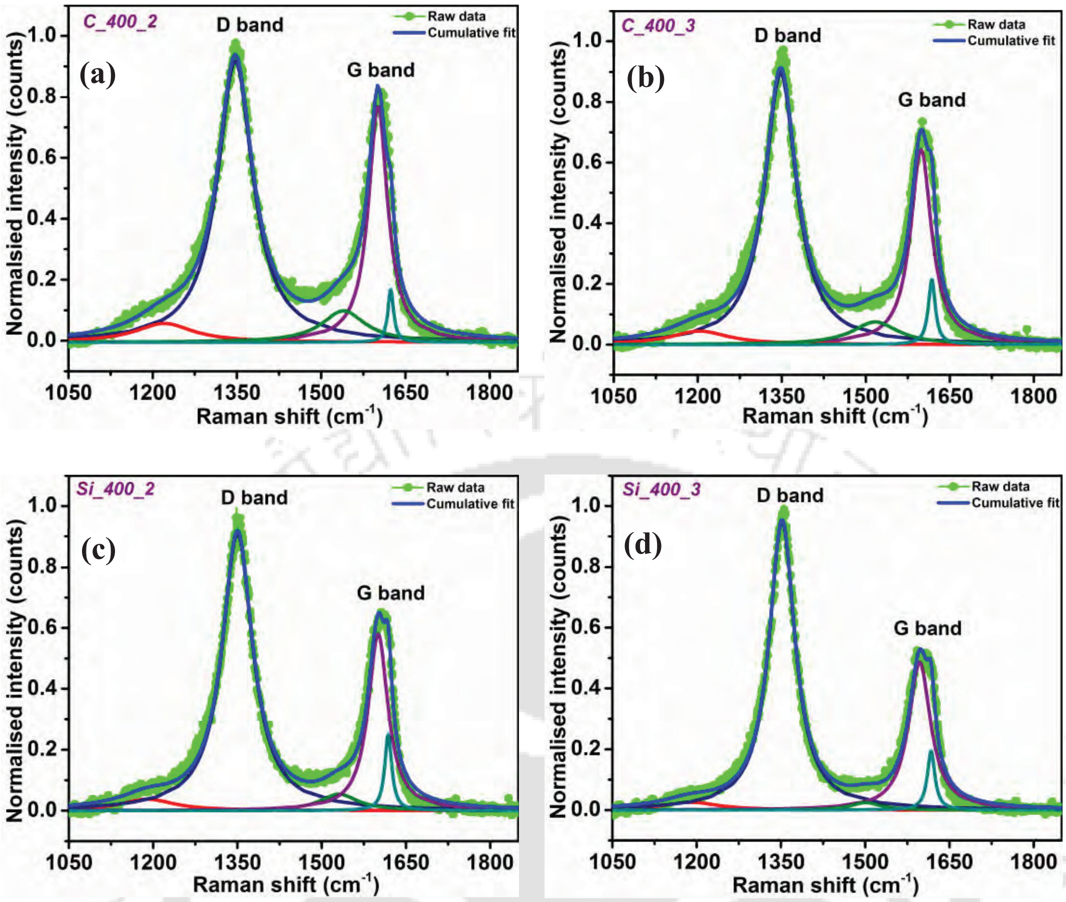

Figure 4.13: *Deconvoluted Raman spectra of CNF (a, b) on corning glass and (c, d) on Si substrates at different PP of 2 and 3 mbar respectively.*

The average width of the flakes (L_a in nm) is 14.5, 13.0 nm for films on corning glass substrate and 11.6, 9.1 nm for the films on Si substrate at PP of 2 and 3 mbar respectively, as calculated using peak intensity ratio I_D/I_G. From the deconvoluted Raman spectra (figure 4.13), FWHM of D band is 76 and 68 cm^{-1} for the films on corning glass substrate, whereas 65 and 55 cm^{-1} for the films on Si substrate at PP of 2 and 3 mbar respectively. However, there is no significant change in the FWHM of G band for the films on corning glass as well as on Si substrates. FWHM of G band is 41, 45 cm^{-1} for the films on corning glass substrate and 42, 47 cm^{-1} for the films on Si substrate at PP of 2 and 3 mbar respectively. The reason of increase in FWHM of D band for the films on corning glass in comparison to Si substrate is probably due to formation of nucleation sites with large number of defects. When a film forming radicals reaches a surface of c-Si, it easily finds a nucleation sites. However on corning glass substrate, the films tend to be amorphous rather than having a periodic crystalline structure.

Table 4.2: Peak intensity ratio I_D/I_G, FWHM of D and G bands of CNF and thickness for the films deposited at different deposition parameters.

Samples (Nomenclature)	**I_D/I_G**	**FWHM (cm^{-1}) (D band)**	**FWHM (cm^{-1}) (G band)**	**L_a (nm)* (using Raman)**	**Thickness (nm)$^{\#}$**	**Growth rate (nm/min)**
			PP variation at T_S of 600 ^{o}C			
Si_600_1	1.56	77	41	10.7	35±6	~ 3-4
Si_600_3	1.58	67	45	10.6	---	
Si_600_5	2.30	53	46	7.3	---	
Si_600_7	1.61	80	51	10.4	70±8	~ 7
			PP variation at T_S of 800 ^{o}C			
Si_800_1	2.04	59	48	8.2	40±6	~ 8
Si_800_2	2.06	61	44	8.1	60±6	~ 12
			Substrate effect at T_S of 400 ^{o}C			
C_400_2	1.16	76	41	14.5	18±6	~ 1
C_400_3	1.29	68	45	13.0	25±5	~ 1
Si_400_2	1.44	65	42	11.6	30±7	~ 1-2
Si_400_3	1.85	55	47	9.1	50±5	~ 2-3

* L_a is the average width of the flakes.

Thickness of the films is measured by stylus profilometer.

4.2.2.iv TEM

Figure 4.14 shows the TEM image and selected area electron diffraction (SAED) pattern of CNF deposited on Cu mesh TEM grid at PP of 3 mbar and T_S of 400 ^{o}C. TEM image further confirms the growth of high density of the flakes connected with each other [10, 12].

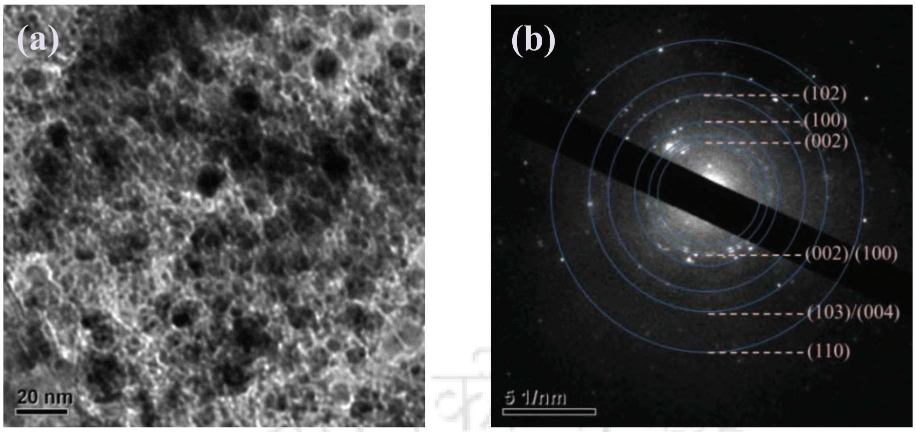

Figure 4.14: *(a) TEM image and (b) SAED pattern of CNF deposited at PP of 3 mbar and* T_S *of 400* ^oC.

SAED pattern shows the high crystallinty of the flakes. From the SAED pattern, the interplanar $d_{spacing}$ is calculated using "Digital Gatan" software and compared with the JCPDS data. We have observed that measured interplanar $d_{spacing}$ is in agreement with the standard $d_{spacing}$ of 3.35 Å, as reported in literature [8, 11, 12]. The center ring with an interplanar spacing 3.46 Å corresponds to (002) plane of graphite. As we move further from the center ring, interplanar spacing are 3.09, 2.52, 1.85, 1.50 and 1.20 Å corresponding to (002)/(100), (100), (102), (103)/(004) and (110) plane of graphitic carbon.

4.3 Optical properties of CNF on glass substrate

4.3.1 UV-Vis-NIR transmittance

Films were characterized by UV-Vis-NIR spectroscopy for the analysis of optical properties of CNF. Figure 4.15 shows UV-Vis-NIR transmission spectra of the films on corning glass substrate at PP of 2 and 3 mbar. Transmission spectra were recorded using blank corning 1737 glass substrates in the path of reference beam. The film deposited at PP of 2 mbar shows approximately 85% transparency in the visible region at 550 nm, whereas transparency of the film is decreased to 55% at PP of 3 mbar. The slightly lower transparency of the films at PP of 3 mbar could be due to the higher thickness of the films in comparison to films deposited at PP of 2 mbar. The transmission spectra of both the films show the maximum absorption at 254 nm corresponding to π → π* transitions of aromatic C-C/C=C bonds [21-23].

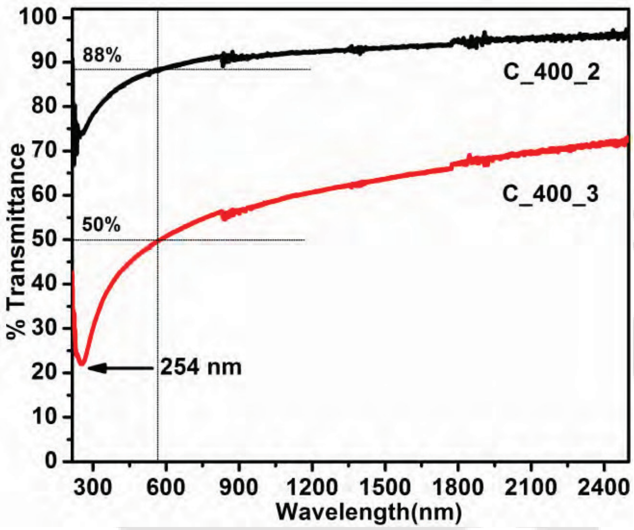

Figure 4.15: *UV-Vis-NIR transmission spectra of CNF on corning glass substrate at PP of 2 and 3 mbar.*

4.3.2 Third order optical nonlinear refractive index coefficient

Third order optical nonlinear refractive index coefficient (n_2) of CNF was measured by closed aperture configuration using single beam Z-scan technique. When the medium is exposed to very high intensity of electromagnetic field (i.e. laser beam), polarization induced by electric field becomes nonlinear and it behaves as nonlinear medium. Therefore, increase or decrease in the refractive index (n_r) of medium, results in the positive and negative nonlinear refractive index respectively. The expression relating the refractive index of nonlinear medium with intensity (I) of electromagnetic field is $n_r = n_0 \pm n_2 I$, where n_0 is linear refractive index and n_2 is the third order nonlinear refractive index coefficient [24-26]. Figure 4.16 shows the normalized transmission spectra of the films, deposited at PP of 2 and 3 mbar, with respect to sample position (± z-axis). The appearance of valley followed by the peak indicates positive nonlinearity of CNF. The increase in refractive index of the medium is explained as follows; as the sample moves toward focus ($z = 0$) from -ve z axis, the decrease in transmittance is observed. Similarly, increase in transmittance is observed towards $z = 0$ in +ve z direction. The decrease and increase in transmittance near the focus ($z = 0$) is due to the decrease and increase in number of photons to the detector plane respectively, resulting in positive nonlinear refractive index of the medium. The ray diagrams of positive and negative nonlinearity are shown in chapter 2 (section 2.2.2). In a closed aperture configuration, an aperture blocks a portion of transmitted light so that only on-axis portion of the beam is collected. The transmittance profile as a function of on axis sample position (± z-axis) in the closed aperture Z-scan is given by equation 4.2 [27-30];

$$T(z,\Delta\phi) = 1 + \frac{4x\Delta\phi}{(x^2+1)(x^2+9)}, where\ x = \frac{z}{z_0} \quad \ldots\ldots\ldots\ldots\ldots\ldots\ldots (4.2)$$

Nonlinear phase shift ($\Delta\phi$) is determined by $\Delta\phi = 2\pi n_2 I_0 L_{eff}/\lambda$

Where, I_0 (=7.46 x 10^3 W/cm^2) is the light intensity on the sample at the focus ($z = 0$) and L_{eff} is the effective thickness of the sample. Since thickness of the films is very small, therefore, using the approximation $Leff = L$, equation (4.2) can be simplified as

$$T(z) = 1 + \frac{az}{(1+bz^2)(9+bz^2)} \ldots\ldots\ldots\ldots\ldots\ldots\ldots\ldots\ldots\ldots\ldots (4.3)$$

Where $a = 4\Delta\phi/z_0 = 1.1845 \times 10^{10} n_2 L_{eff}$ and $b = 1/z_0^2$

z_0 (= 2.5 mm) is the Rayleigh length of laser beam.

Nonlinear refractive index coefficient (n_2) of the films was found to be 6.09 x 10^{-5} and 7.22 x 10^{-5} cm^2/W for the films deposited at PP of 2 and 3 mbar respectively. The slightly increased nonlinearity of the medium for the films at PP of 3 mbar could be due to higher thickness of the films (which can also be seen from the lower transparency of the films at PP of 3 mbar) in comparison to film deposited at PP of 2 mbar.

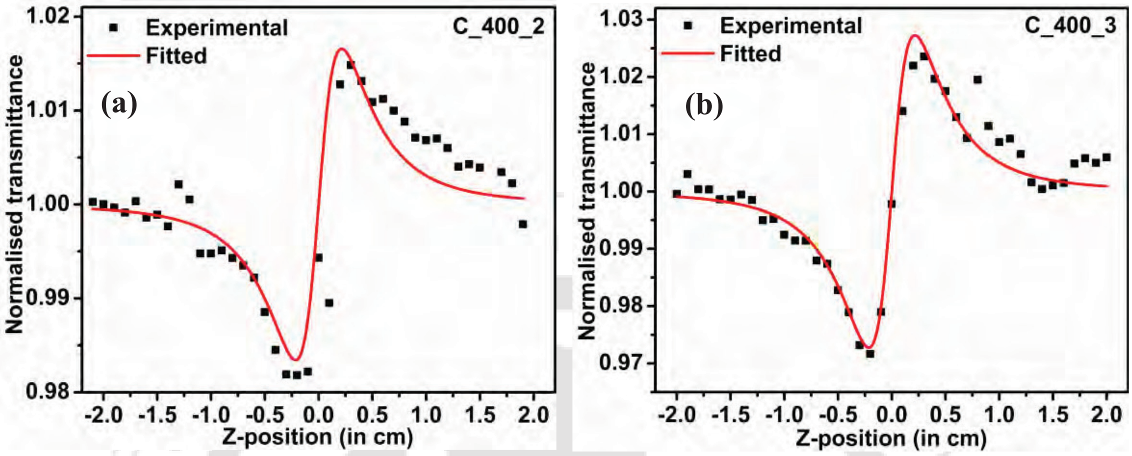

Figure 4.16: *Nonlinear transmission spectra of CNF deposited on corning glass substrate at PP of (a) 2 mbar and (b) 3 mbar.*

4.4 Electrical properties of carbon nanoflakes

4.4.1 Temperature dependent electrical conductivity

Figure 4.17 shows the temperature dependent electrical conductivity of the films deposited on corning glass substrate at PP of 2 and 3 mbar. Electrical conductivity was measured in the temperature range 300 – 480 K using coplanar geometry with approximately 0.6 mm of electrode separation. Room temperature electrical conductivity of the films was 26 and 21 S/cm for the films deposited at 2 and 3 mbar respectively. The conductivity of the films was found to increase almost linearly with increasing temperature and the measured value of conductivity at 480 K was 32 and 24 S/cm for the films deposited at 2 and 3 mbar respectively. These observations suggest that the electrical conductivity of CNF has week temperature dependence [3, 16, 31]. The higher conductivity for the films deposited at PP of 2 mbar could be due to the smaller lateral size of the flakes at PP of 2 mbar in comparison to 3 mbar, as shown in surface height profile of AFM image (figure 4.10), which results in the increase in effective conduction path length for the charge carriers.

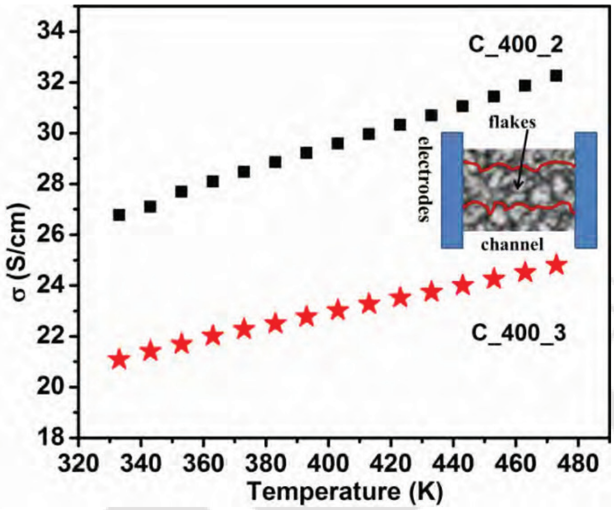

Figure 4.17: *Temperature dependent electrical conductivity of CNF on corning glass substrate at PP of 2 and 3 mbar.*

An inhomogeneity in the films could result in to actual path being zigzag rather than straight as shown in inset of figure 4.17, which is different than the separation between the electrodes used for calculating the conductivity of the films. The temperature coefficient of resistance (i.e. (dR/dT)/R) is $-1.21\text{x}10^{-3}$/K and $-1.07\text{x}10^{-3}$/K for the films deposited at PP 2 and 3 mbar respectively, which is in good agreement with the temperature coefficient of resistance of graphene [32]. Negative value of temperature coefficient of resistance shows the semiconducting behavior of carbon nanoflakes.

4.5 Conclusion

Vertically aligned CNF were successfully deposited by HFCVD method on p-type Si substrate. Influence of different deposition parameters such as process pressure and substrate temperature on structural properties of the films were characterized by FESEM, AFM and Raman scattering study. We have observed that with increasing PP from 1 to 5 mbar, lateral size of the flakes is increased and with further increase in PP to 7 mbar, the orientation of the flakes is not completely vertical. We have also observed that with increasing substrate temperature, the average width of the flakes is decreased. This indicates that at high substrate temperature, CNF grow faster in upward direction in comparison to planar growth. We have studied the growth of CNF on different substrates and observed that CNF can also be deposited on corning glass substrate, similar to that on Si substrate. Growth rate of CNF is slightly lower on corning glass substrate in comparison to Si substrate. However, further investigation is needed for the study of change in microstructural properties by the influence of substrate temperature. Electrical conductivity of CNF has weak temperature dependence and the negative temperature coefficient of resistance shows the semiconducting behavior of CNF. Nonlinear refractive index coefficient of the films was 6.09×10^{-5} and 7.22×10^{-5} cm^2/W at a laser wavelength of 632.8 nm for the films deposited at PP of 2 and 3 mbar respectively. The observed third order nonlinear refractive index coefficient of the order of 10^{-5} cm^2/W suggests that, like graphite and CNT, CNF may also be used as nonlinear medium in the field of nonlinear photonics.

4.6 References

[1] N.G. Shang, F.C.K. Au, X.M. Meng, C.S. Lee, I. Bello, S.T. Lee, Uniform carbon nanoflake films and their field emissions, Chemical Physics Letters, 358 (2002) 187-191.

[2] S. Kondo, S. Kawai, W. Takeuchi, K. Yamakawa, S. Den, H. Kano, M. Hiramatsu, M. Hori, Initial growth process of carbon nanowalls synthesized by radical injection plasma-enhanced chemical vapor deposition, Journal of Applied Physics, 106 (2009) 094302.

[3] H.J. Cho, H. Kondo, K. Ishikawa, M. Sekine, M. Hiramatsu, M. Hori, Density control of carbon nanowalls grown by CH_4/H_2 plasma and their electrical properties, in: Carbon, 2014, pp. 380-388.

[4] M. Ohring, Materials Science of Thin Film; Second edition, (2006) Page No: 358.

[5] M. Hiramatsu, K. Shiji, H. Amano, M. Hori, Fabrication of vertically aligned carbon nanowalls using capacitively coupled plasma-enhanced chemical vapor deposition assisted by hydrogen radical injection, Applied Physics Letters, 84 (2004) 4708-4710.

[6] T. Itoh, Synthesis of carbon nanowalls by hot-wire chemical vapor deposition, Thin Solid Films, 519 (2011) 4589-4593.

[7] S.Y. Kim, W.S. Choi, J.-H. Lee, B. Hong, Substrate temperature effect on the growth of carbon nanowalls synthesized via microwave PECVD, Materials Research Bulletin, 58 (2014) 112-116.

[8] J. Wang, M. Zhu, R.A. Outlaw, X. Zhao, D.M. Manos, B.C. Holloway, Synthesis of carbon nanosheets by inductively coupled radio-frequency plasma enhanced chemical vapor deposition, Carbon, 42 (2004) 2867-2872.

[9] S. Shimabukuro, Y. Hatakeyama, M. Takeuchi, T. Itoh, S. Nonomura, Preparation of Carbon Nanowall by Hot-Wire Chemical Vapor Deposition and Effects of Substrate Heating Temperature and Filament Temperature, Japanese Journal of Applied Physics, 47 (2008) 8635.

[10] K. Davami, M. Shaygan, N. Kheirabi, J. Zhao, D.A. Kovalenko, M.H. Rümmeli, J. Opitz, G. Cuniberti, J.-S. Lee, M. Meyyappan, Synthesis and characterization of carbon nanowalls on different substrates by radio frequency plasma enhanced chemical vapor deposition, Carbon, 72 (2014) 372-380.

[11] J.J. Wang, M.Y. Zhu, R.A. Outlaw, X. Zhao, D.M. Manos, B.C. Holloway, V.P. Mammana, Free-standing subnanometer graphite sheets, Applied Physics Letters, 85 (2004) 1265-1267.

[12] C.-H. Tu, W. Chen, H.-C. Fang, Y. Tzeng, C.-P. Liu, Heteroepitaxial nucleation and growth of graphene nanowalls on silicon, Carbon, 54 (2013) 234-240.

[13] S. Kurita, A. Yoshimura, H. Kawamoto, T. Uchida, K. Kojima, M. Tachibana, P. Molina-Morales, H. Nakai, Raman spectra of carbon nanowalls grown by plasma-enhanced chemical vapor deposition, Journal of Applied Physics, 97 (2005) 104320.

[14] S. Shimabukuro, Y. Hatakeyama, M. Takeuchi, T. Itoh, S. Nonomura, Effect of hydrogen dilution in preparation of carbon nanowall by hot-wire CVD, Thin Solid Films, 516 (2008) 710-713.

[15] K. Yu, Z. Bo, G. Lu, S. Mao, S. Cui, Y. Zhu, X. Chen, R. Ruoff, J. Chen, Growth of carbon nanowalls at atmospheric pressure for one-step gas sensor fabrication, Nanoscale Research Letters, 6 (2011) 202.

[16] K. Teii, S. Shimada, M. Nakashima, A.T.H. Chuang, Synthesis and electrical characterization of n-type carbon nanowalls, Journal of Applied Physics, 106 (2009) 084303.

[17] M.S. Dresselhaus, A. Jorio, A.G. Souza Filho, R. Saito, Defect characterization in graphene and carbon nanotubes using Raman spectroscopy, Philosophical Transactions of the Royal Society of London A: Mathematical, Physical and Engineering Sciences, 368 (2010) 5355-5377.

[18] R. Beams, L.G. Cançado, L. Novotny, Raman characterization of defects and dopants in graphene, Journal of Physics: Condensed Matter, 27 (2015) 083002.

[19] T. Yamada, M. Ishihara, M. Hasegawa, Large area coating of graphene at low temperature using a roll-to-roll microwave plasma chemical vapor deposition, Thin Solid Films, 532 (2013) 89-93.

[20] F. Tuinstra, J.L. Koenig, Raman Spectrum of Graphite, The Journal of Chemical Physics, 53 (1970) 1126-1130.

[21] K. Sung Yun, J. Yeun Ho, C. Won Seok, Growth properties of carbon nanowalls on glass substrates by a microwave plasma-enhanced chemical vapor deposition, Japanese Journal of Applied Physics, 53 (2014) 05FD09.

[22] J. Kim, M. Ishihara, Y. Koga, K. Tsugawa, M. Hasegawa, S. Iijima, Low-temperature synthesis of large-area graphene-based transparent conductive films using surface wave plasma chemical vapor deposition, Applied Physics Letters, 98 (2011) 091502.

[23] S. Saxena, T.A. Tyson, S. Shukla, E. Negusse, H. Chen, J. Bai, Investigation of structural and electronic properties of graphene oxide, Applied Physics Letters, 99 (2011) 013104.

[24] G.V. Prakash, M. Cazzanelli, Z. Gaburro, L. Pavesi, F. Iacona, G. FranzÒ, F. Priolo, Linear and nonlinear optical properties of plasma-enhanced chemical-vapour deposition grown silicon nanocrystals, Journal of Modern Optics, 49 (2002) 719-730.

[25] F.W. Shi, X.J. Meng, G.S. Wang, J.L. Sun, T. Lin, J.H. Ma, Y.W. Li, J.H. Chu, The third-order optical nonlinearity of $Bi_{3.2}5La_{0.75}Ti_3O_{12}$ ferroelectric thin film on quartz, Thin Solid Films, 496 (2006) 333-335.

[26] R. del Coso, J. Solis, Relation between nonlinear refractive index and third-order susceptibility in absorbing media, J. Opt. Soc. Am. B, 21 (2004) 640-644.

[27] H. Zhang, S. Virally, Q. Bao, L. Kian Ping, S. Massar, N. Godbout, P. Kockaert, Z-scan measurement of the nonlinear refractive index of graphene, Opt. Lett., 37 (2012) 1856-1858.

[28] M. Sheik-bahae, A.A. Said, E.W. Van Stryland, High-sensitivity, single-beam n_2 measurements, Opt. Lett., 14 (1989) 955-957.

[29] m. Sheik-Bahae, A.A. Said, T.-H. Wei, D.J. Hagan, E.W.V. Stryland, Sensitive Measurement of Optical Nonlinearities using a single beam, IEEE Journal of Quantum Electronics, 26 (1990) 760 - 769.

[30] G.V. Prakash, M. Cazzanelli, Z. Gaburro, L. Pavesi, F. Iacona, G. Franzò, F. Priolo, Nonlinear optical properties of silicon nanocrystals grown by plasma-enhanced chemical vapor deposition, Journal of Applied Physics, 91 (2002) 4607-4610.

[31] T. Itoh, Y. Nakanishi, T. Ito, A. Vetushka, M. Ledinský, A. Fejfar, J. Kočka, S. Nonomura, Electrical properties of carbon nanowall films, Journal of Non-Crystalline Solids, 358 (2012) 2548-2551.

[32] K.S. Vasu, B. Chakraborty, S. Sampath, A.K. Sood, Probing top-gated field effect transistor of reduced graphene oxide monolayer made by dielectrophoresis, Solid State Communications, 150 (2010) 1295-1298.

Chapter 5

Single and Multi-layers Graphene Thin Films

In this chapter, structural, optical (linear/nonlinear) and electrical properties of single and multi-layers graphene thin films deposited by hot filament chemical vapor deposition (HFCVD) are studied in detail. Graphene films were deposited on Ni foil by varying different deposition parameters such as process pressure (PP), substrate temperature (T_S), deposition time (t_d) and precursors gases (CH_4, H_2, N_2) flow rates. Further, graphene films were transferred on different substrates such as quartz and Si using chemical etching process for the analysis of different properties of the films. Structural properties of graphene films are studied using Raman scattering with different excitation wavelength, field emission scanning electron microscopy (FESEM), atomic force microscopy (AFM) and transmission electron microscopy (TEM). Optical and electrical properties of the films are studied using UV-Vis-NIR spectroscopy (linear), Z-scan technique (nonlinear) and I-V measurement with two probes respectively.

5.1 Experimental details

5.1.1 Deposition parameters

Graphene films were deposited on Ni foil (125 μm thick, 99.9% purity) by HFCVD method using CH_4, H_2 and N_2 precursor gases. Films were deposited by varying process pressure, deposition time and $CH_4/H_2/N_2$ gas flow rates. Deposition parameters for the growth of graphene films are divided into three series; influence of process pressure at T_S of 600 °C, Influence of deposition time at T_S of 700 °C and influence of H_2/N_2 dilution at T_S of 700 °C. Deposition parameters such as substrate temperature, process pressure, deposition time and $CH_4/H_2/N_2$ gas flow rate are listed in table 5.1. Other deposition parameters such as filament temperature and filament to substrate distance were kept at 2050±50 °C and 1.5 cm respectively for all the films. Filament temperature was measured using pyrometer by focusing it at the center of tungsten filament. We have used nomenclature to identify the samples in the following manner; series I_PP_t_d, series II_PP_t_d and series III_H_2/N_2 flow rate_t_d corresponding to three different series of deposition parameters. After deposition, films deposited in series II and III were further annealed at high temperature as mentioned in table 5.1 followed by cooling rate of 10 °C/min before taking these out of HFCVD system.

5.1.2 Transfer process of graphene on different substrates

Graphene films as deposited on Ni foil were transferred on quartz and Si substrates by chemical etching process using the method described in literature [1, 2]. Transfer process involves several steps; first, poly methyl methacrylate (PMMA) was dissolved into tetrahydrofuran (THF) solvent (5 mg/ml) and a drop of PMMA was poured on the top of graphene films. After coating PMMA, etching of Ni was done by $FeCl_3$ 1M solution. Complete Ni was etched after 12 h and graphene was found as floating in $FeCl_3$ solution with the support of PMMA. The floated graphene films were transferred on different substrates such as quartz and Si. After graphene was transferred to the desired substrates, acetone was used for the removal of PMMA. Graphene films were subsequently washed with de-ionised water. The transfer process of graphene films on arbitrary substrates are shown in figure 5.1 and graphene films floating in acetone are also shown in the right hand side of figure 5.1.

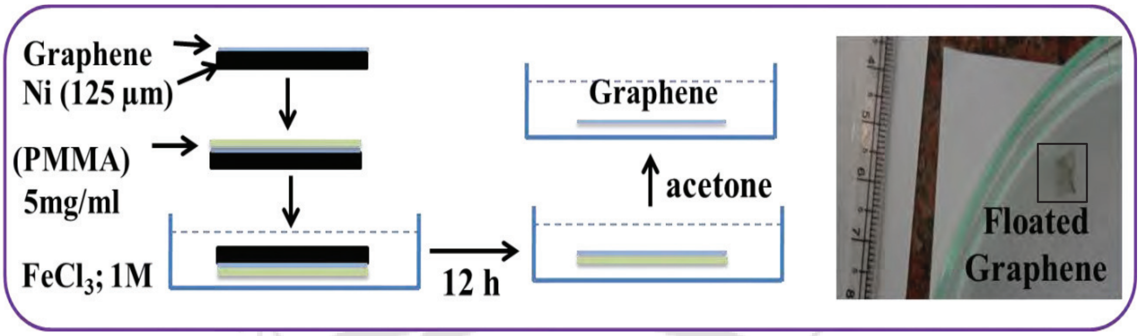

Figure 5.1: *Schematic of transfer process of graphene films on different substrates.*

Table 5.1: Deposition parameters for the growth of single and multi-layers graphene films.

Samples	Nomenclature	T_S (°C)	PP (mbar)	CH_4 (sccm)	H_2 (sccm)	Deposition time (min)
	(I_A_PP_t_d)	**Series I_A: PP variation at t_d 10 min**				
HW152	I_A_1_10 min	600	1	15	5	10
HW149	I_A_2_10 min	600	2	15	5	10
HW153	I_A_3_10 min	600	3	15	5	10
HW150	I_A_5_10 min	600	5	15	5	10
		Series I_B: PP variation at t_d 5 min				
HW155	I_B_1_5 min	600	1	15	5	5
HW156	I_B_2_5 min	600	2	15	5	5
HW157	I_B_3_5 min	600	3	15	5	5
	(II_PP_t_d)	**Series II: deposition time variation** (after deposition annealed at 700 °C for 10 min)				
HW197	II_1.5_10 min	700	1.5	5	20	10
HW191	II_1.5_20 min	700	1.5	5	20	20
HW198	II_1.5_30 min	700	1.5	5	20	30
HW195	II_1_10 min	700	1	5	20	10
	(III_H_2/N_2 flow rate)	**Series III: H_2/N_2 dilution at T_S 700 °C** (after deposition annealed at 800 °C for 1h)				
					H_2/N_2	
HW260	III_H_2/N_2:30/0	700	1	5	30/0	10
HW264	III_H_2/N_2:40/0	700	1	5	40/0	10
HW259	III_H_2/N_2:30/3	700	1	5	30/3	10

5.2 Structural properties of single and multi-layers graphene films

5.2.1 Series I_A: Influence of PP at fixed t_d of 10 min and T_S of 600 ^oC

5.2.1.i FESEM

Figure 5.2 shows the FESEM image of as deposited graphene film on Ni foil and transferred graphene films on quartz and TEM grid for the films deposited at PP of 2 mbar and t_d of 10 min.

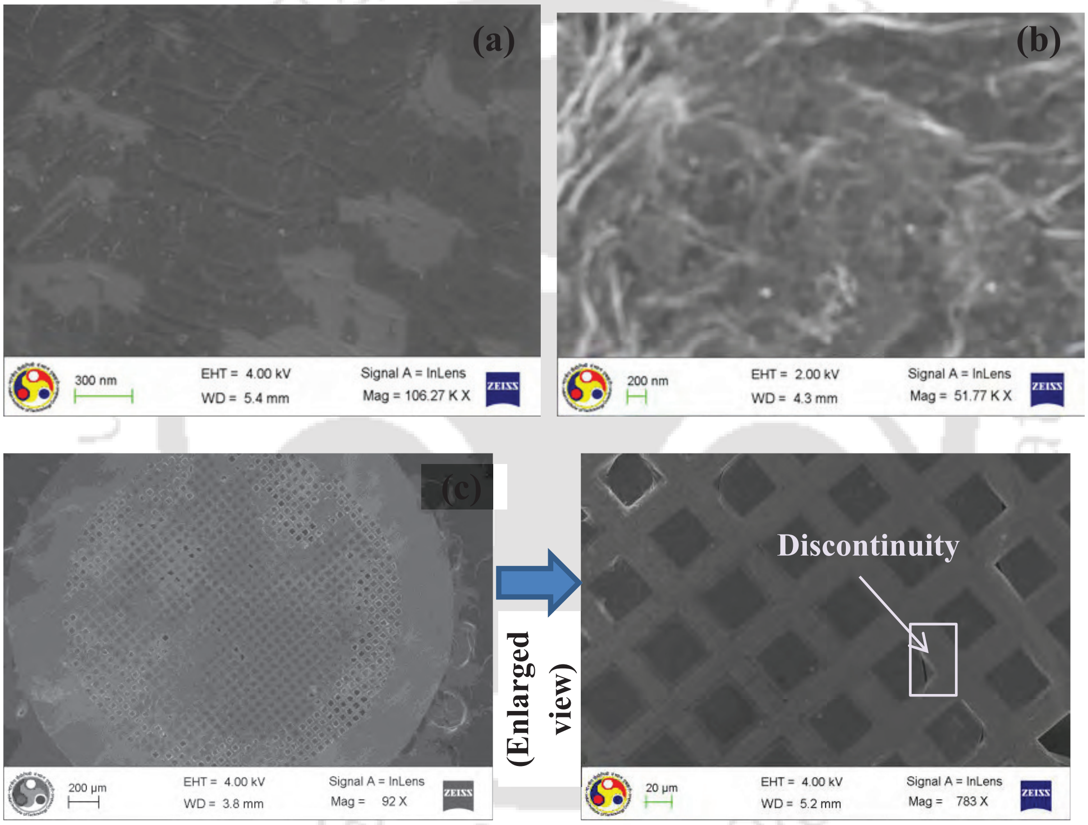

Figure 5.2: *FESEM image of graphene for the films deposited at PP of 2 mbar and t_d of 10 min and at fixed T_S of 600 ^oC (a) as deposited on Ni foil (b) transferred films on quartz substrate and (c) transferred films on TEM grid.*

FESEM images show that graphene films are successfully transferred on different substrates. As deposited films on Ni foil show some wrinkles at the surface of graphene. The formation of wrinkles is probably due to small compression in Ni foil during cooling after deposition [3-5]. From FESEM images of transferred graphene films, we can see that films have mixed with different number of layers, which can be identified from the different contrast at several locations of the films. Dark portions show slightly less number of graphene layers in comparison to bright portion of the films. Enlarged view of graphene films transferred on TEM grid shows that the films are uniform in large area (~ in the dimension of the order of 100 µm).

5.2.1.ii Raman scattering

Raman spectroscopy is an important characterization technique to distinguish the graphene from graphite, identify the defects and number of graphene layers. Figure 5.3 shows the Raman spectra of graphene films as deposited on Ni foil and transferred films on different substrates for the films deposited at different PP of 1, 2, 3 and 5 mbar and at fixed t_d of 10 min. Raman spectra of the films were recorded with excitation wavelength 514.53 nm. Raman spectra of the films show prominent characteristic peaks at approximately 1350 cm^{-1} (D band), 1582 cm^{-1} (G band), 1624 cm^{-1} (D' band), 2450 cm^{-1}, 2690 cm^{-1} (2D band), 2950 cm^{-1} (D+G band) and 3245 cm^{-1} (2D'/G+D' band). First order Raman peak in graphene, known as G band, is due to the in-plane sp^2 C-C stretching (in plane transverse optical phonon) mode which is originated from phonon at the Γ point in the center of first Brillouin zone [6-9]. The defect induced D band is due to defects in hexagonal structure and at the edges of graphene which is originated from in-plane breathing-like (in plane longitudinal optical phonon) mode, which is associated at near K-point in the first Brillouin zone [10-12]. D' band is also associated with disorder, which appears in nano-crystalline graphite [6, 13]. Symmetry of peak, full width at half maxima (FWHM) and peak position of second order 2D band is very sensitive to the number of graphene layers. However, Raman spectra can be used to distinguish approximately up to 20 layers, beyond that there is no difference between Raman spectra of graphite and these multi-layers graphene films [10, 14, 15]. The peak intensity ratio of G and 2D band (I_G/I_{2D}) is widely used for determining the number of layers in graphene films, whereas peak intensity ratio of D and G band (I_D/I_G) is used for the determination of defects in the films [4, 10, 16, 17].

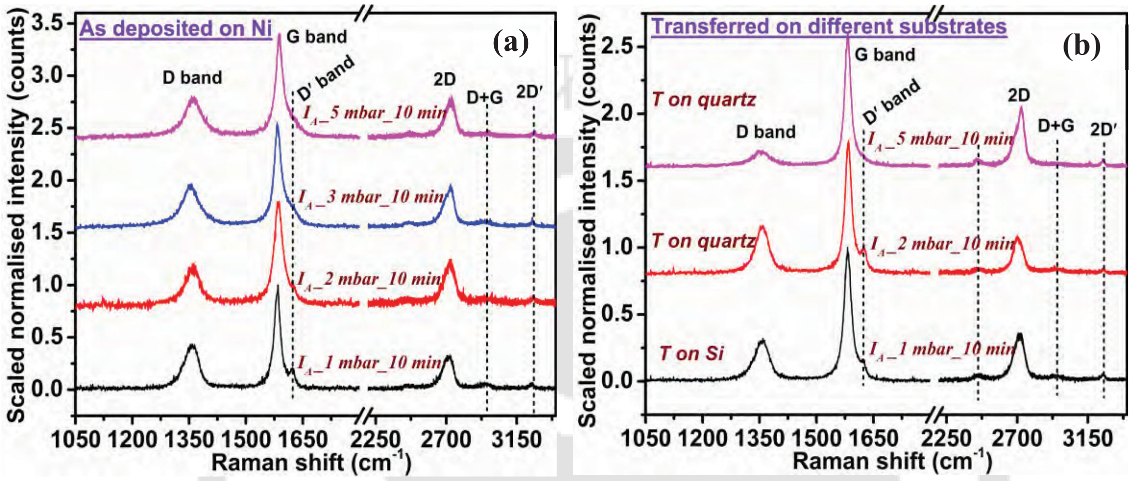

Figure 5.3: *Raman spectra of graphene (a) as deposited on Ni foil and (b) transferred films on different substrates for the films deposited at different process pressure at fixed* t_d *of 10 min.*

In order to determine the defects and number of layers in graphene films, measured Raman spectra are deconvoluted using Lorentzian peak fit in the range 1100 – 2900 cm^{-1} corresponding to different vibrational modes, as shown in figure 5.4. Peak position, FWHM, peak intensity ratio I_D/I_G and I_G/I_{2D} for the deconvoluted Raman spectra are listed in table 5.2. Deconvoluted Raman spectra show that FWHM of G band is in the range of 20 – 27 cm^{-1} and peak intensity ratio I_D/I_G for all the as deposited films is less than one, which indicate highly crystalline nature of the films in terms of highly oriented honeycomb structure of graphene. Deconvoluted Raman spectra show the asymmetry in 2D band with large FWHM in the range of 70 – 80 cm^{-1}, which can be deconvoluted into two different peaks $2D_1$ and $2D_2$. The peak intensity ratio I_G/I_{2D} in the range of 2.5 – 3.1

and large FWHM of 2D band indicate that all the as deposited films are graphitic in nature.

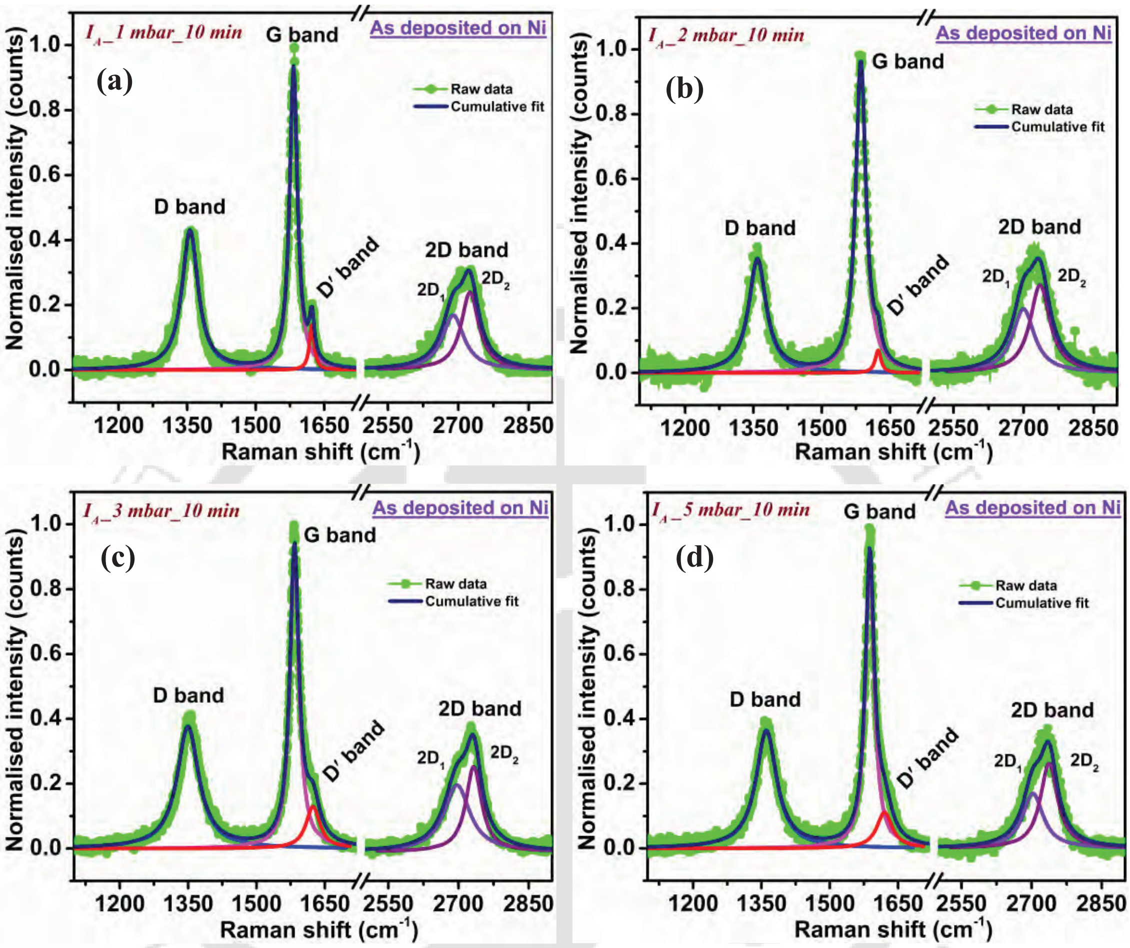

***Figure 5.4:** Deconvoluted Raman spectra of graphene as deposited on Ni foil for the films deposited at different PP of (a) 1 mbar, (b) 2 mbar, (c) 3 mbar and (d) 5 mbar at fixed t_d of 10 min.*

5.2.1.iii TEM

To determine the crystallinity of the films in terms of orientation of carbon atoms into a honeycomb structure, films were further characterized by transmission electron microscopy. Figure 5.5 shows the selected area electron diffraction (SAED) pattern and high resolution transmission electron microscope (HRTEM) image of graphitic thin films transferred on TEM grid (Cu mesh) for the films deposited at PP of 2 mbar and t_d of 10 min. SAED pattern shows the well oriented honeycomb structure of multi-layers graphene. From SAED pattern, the observed interplanar spacing are 3.69, 2.06 and 1.42 Å corresponding to (002), (101) and (004) plane of multi-layers graphene. Interplanar spacing corresponding to (002) plane of multi-layers graphene is 3.1Å as measured from HRTEM image, which is in agreement with the standard interlayer spacing 3.35Å of graphite as reported in literature [5, 17].

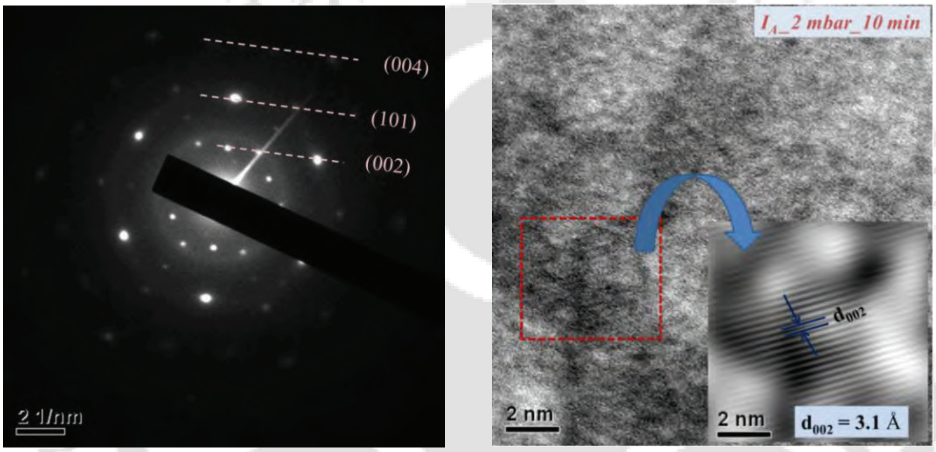

Figure 5.5: *SAED pattern (left) and HRTEM image (right) of graphene film transferred on TEM grid (Cu mesh) for the films deposited at PP of 2 mbar and t_d of 10 min.*

5.2.2 Series I_B: Influence of PP at fixed t_d of 5 min and T_S of 600 °C

As we have observed (in section 5.2.1) that all the films show graphitic nature. Therefore, for the next series of deposition, deposition time was decreased to 5 min in order to obtain single layer graphene films.

5.2.2.i FESEM

Figure 5.6 shows the FESEM image of graphene film as deposited on Ni foil and transferred on Si substrate for the films deposited at PP of 3 mbar at fixed t_d of 5 min and T_S of 600 °C. FESEM image shows that graphene films are uniformly grown on Ni foil (figure 5.6 a). The confirmation of growth of graphene can be clearly seen from the wrinkles on the surface of the films. In order to have a clear view of graphene films on Ni foil and further transfer of large area graphene films on different substrates, images are shown here in different scale. FESEM image of transferred films on Si substrate (figure 5.6 b) shows the mixing of different layer of graphene, similar to transferred films on quartz substrate (section 5.2.1).

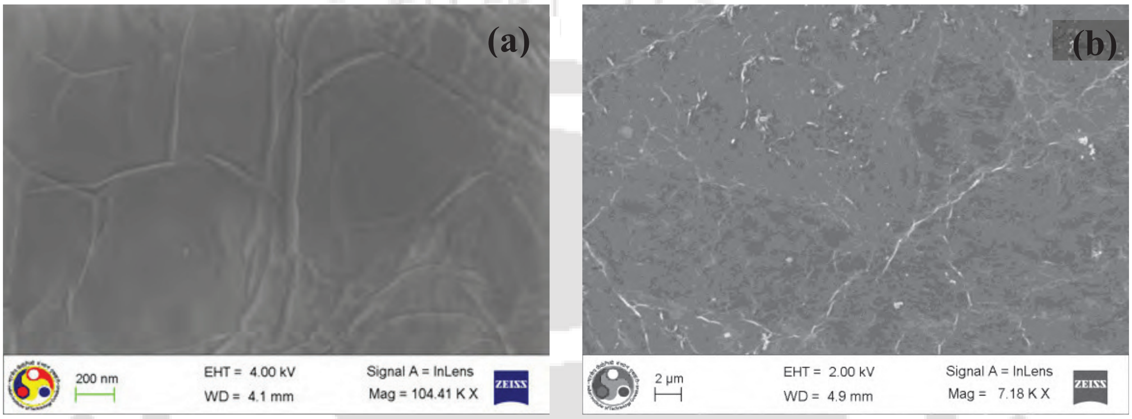

Figure 5.6: *FESEM image of graphene (a) as deposited on Ni foil and (b) transferred film on Si substrate for the films deposited at PP of 3 mbar and t_d of 5 min.*

5.2.2.ii Raman scattering

Figure 5.7 shows the Raman spectra of as deposited graphene films on Ni foil and transferred graphene films on Si substrate for the films deposited at different PP of 1, 2 and 3 mbar at fixed t_d of 5 min. Raman spectra were recorded with an excitation wavelength of 514.53 nm. Raman spectra of as deposited graphene films, figure 5.7 (a), show all the characteristic peaks such as D band, G band, etc. as mentioned in section 5.2.1. Raman spectra of transferred graphene films, figure 5.7 (b), also show almost similar characteristic features with slightly more defects in comparison to as deposited films on Ni foil. This shows that graphene films are successfully transferred on Si substrate. In order to determine the defects and number of graphene layers, Raman spectra are deconvoluted using Lorentzian peak fit in the range 1100 – 2900 cm^{-1}, as shown in figure 5.8. Peak position, FWHM and peak intensity ratio I_D/I_G and I_G/I_{2D} for the deconvoluted spectra corresponding to different PP of 1, 2 and 3 mbar are listed in table 5.2. Deconvoluted Raman spectra show that FWHM of G band is in the range of 25 – 28 cm^{-1} and peak intensity ratio I_D/I_G is less than one. This shows that high quality films are deposited with very low defects [2, 3, 18]. FWHM of deconvoluted Raman spectra of 2D band and peak intensity ratio I_G/I_{2D} are in the range of 70 – 80 cm^{-1} and 2.5 – 3.1 respectively, which again indicates the formation of graphitic thin films.

Table 5.2: Peak position, FWHM and peak intensity ratio of D, G and 2D bands for the films deposited at different process pressure at fixed T_S of 600 °C.

Samples	FWHM (D band) (cm^{-1})	FWHM (G band) (cm^{-1})	FWHM (D' band) (cm^{-1})	Peak Pos./ FWHM (2D band) (cm^{-1})			I_D/I_G (using peak intensity)	I_G/I_{2D} (using peak intensity)	No. of layers (n)	Grain size (L_a, nm)
Series I_A: PP variation at fixed t_d of 10 min and T_S of 600 °C										
				2D	**$2D_1$**	**$2D_2$**				
***I_A_1_ 10 min**	42	20	12	74	2689 /56	2724 /45	0.46	3.1	≥20	36.5
I_A_2_ 10 min	46	27	15	77	2699 /56	2735 /51	0.36	2.6	≥20	46.7
I_A_3_ 10 min	57	23	36	75	2696 /66	2732 /40	0.40	2.5	≥20	42.0
I_A_5_ 10 min	55	23	41	75	2702 /53	2737 /44	0.40	2.7	≥20	42.0
Series I_B: PP variation at fixed t_d of 5 min and T_S of 600 °C										
I_B_1_ 5 min	61	27	38	79	2697 /57	2730 /50	0.37	2.5	≥20	45.4
I_B_2_ 5 min	73	28	36	77	2699 /60	2734 /48	0.44	2.9	≥20	38.2
I_B_3_ 5 min	48	25	22	75	2689 /60	2724 /56	0.25	3.1	≥20	67.2

*I_1_10 min: I_1 mbar_10 min, similarly others

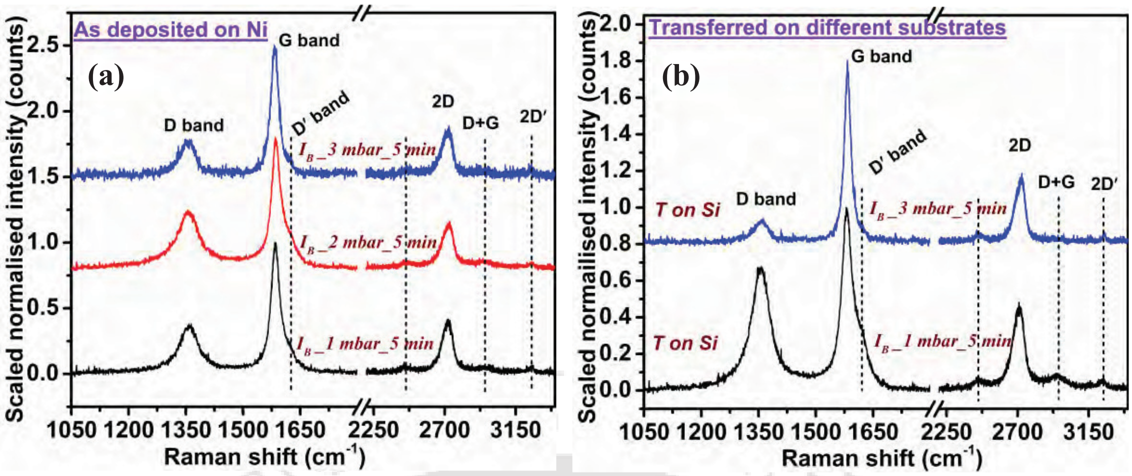

Figure 5.7: *Raman spectra of graphene (a) as deposited on Ni foil and (b) transferred on different substrates for the films deposited at different process pressure at fixed t_d of 5 min.*

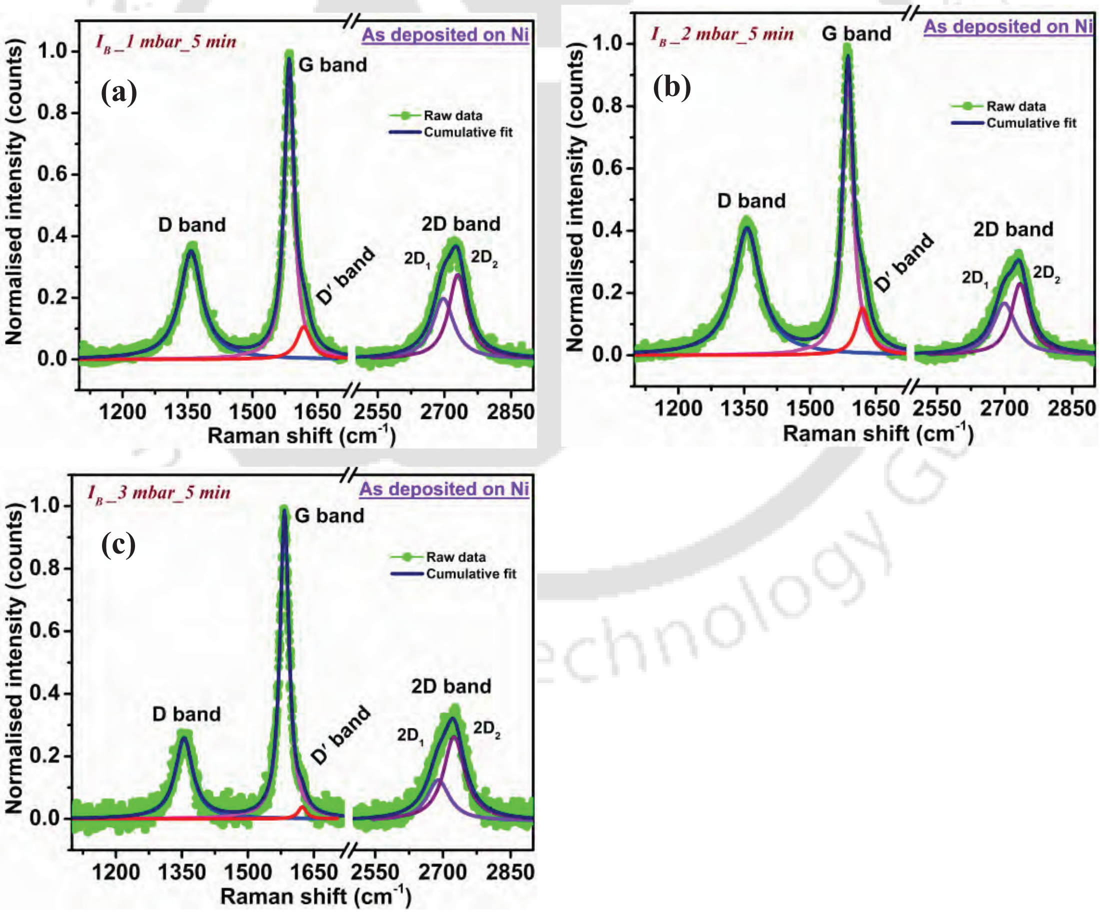

Figure 5.8: *Deconvoluted Raman spectra of graphene films as deposited on Ni foil at different PP of (a) 1 mbar, (b) 2 mbar and (c) 3 mbar at fixed t_d of 5 min.*

We have observed that with decrease in deposition time, FWHM of defect induced D bands are increased to the range of 48 – 73 cm^{-1} in comparison to the films deposited with 10 min deposition time (as mentioned in section 5.2.1.ii) having FWHM of D band in the range of 46 – 57 cm^{-1}. Thus, from these results we can conclude that the chosen parameters are suitable for the uniform growth of thin graphitic films with low defects over large area of the substrate. The reason of obtaining graphitic films could be due to high concentration of methane and also due to low T_S of 600 ^oC. Since at this low temperature, the diffusivity of carbon species into the bulk Ni is very less [19], therefore all the carbon atoms reside only on the surface of substrate and hence graphitic nature of the films are observed.

5.2.3 Series II: Influence of deposition time at fixed T_S of 700 ^oC

As we have observed in section 5.2.2, all the as deposited films show graphitic nature even with decrease in deposition time to 5 min. Therefore, in next series of deposition, films were deposited at high substrate temperature, low process pressure and comparatively low methane concentration. The reason of choosing these parameters for the growth of single layer graphene is to reduce the concentration of methane as well as to increase the diffusivity of carbon atoms into bulk Ni. Since diffusivity of carbon atoms in bulk Ni is comparatively more at higher temperature, therefore deposition time needs to be optimized for the growth of single or a few layer graphene films.

5.2.3.i Raman scattering

Figure 5.9 shows the Raman spectra of graphene films as deposited on Ni foil for the films deposited at different t_d of 10, 20 and 30 min. Raman spectra of the films were recorded with an excitation wavelength 514.53 nm. In this series, films were deposited at fixed T_S of 700 ^oC and followed by subsequent annealing at the same temperature for 10 min after deposition. Other deposition parameters such as CH_4/H_2 gas flow rate and process pressure are listed in table 5.1. We have observed that, with increasing substrate temperature and decrease in methane concentration, Raman spectra of as deposited graphene films show different features for the films deposited at different deposition time. The most important point in the Raman spectra is that all the films have very less defects (i.e. almost defect free) confirmed from the peak intensity ratio I_D/I_G. This shows that low methane concentration and low process pressure is the key parameter for the growth of high quality graphene films. All the films show FWHM of G band in the range of 21 – 23 cm^{-1}, peak intensity ratio I_D/I_G in the range of ~0 – 0.15 and the absence of D' band which indicate the highly crystalline defect free graphene films. Peak position, FWHM and peak intensity ratio I_D/I_G and I_G/I_{2D} for all the films deposited at different deposition time are listed in table 5.3.

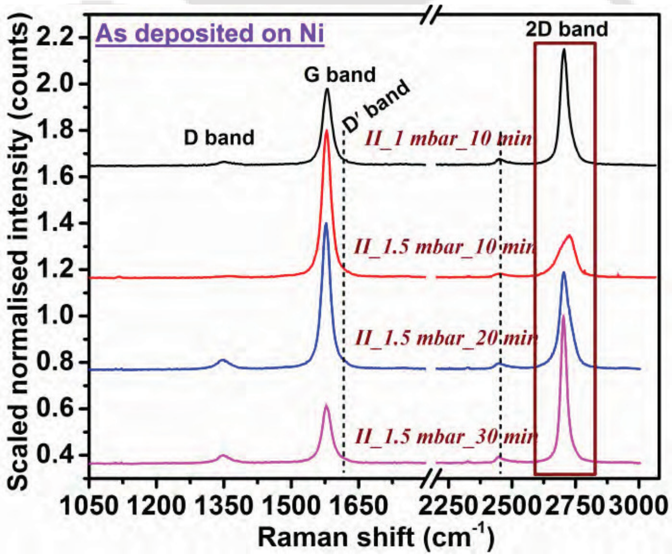

Figure 5.9: *Raman spectra of graphene films as deposited on Ni foil at different t_d of 10, 20 and 30 min at fixed T_S of 700 ^oC for the films deposited at PP of 1 and 1.5 mbar.*

Raman spectra show that FWHM of 2D band and peak intensity ratio I_G/I_{2D} is decreased from 73 to 27 cm^{-1} and 3.5 to 0.4 respectively with increasing deposition time from 10 to

30 min. The decrease in FWHM of 2D band and peak intensity ratio I_G/I_{2D} indicate the formation of graphene films towards single layer from the graphitic thin films with grain size in the range of 100 nm to a few µm, which is much larger in comparison to films deposited at low T_S 600 ^oC (section 5.2.1 and 5.2.2). The average grain size (L_a, in nm) is calculated using Tuinstra – Koenig empirical relation [12, 20-22]. The FWHM and peak intensity ratio I_G/I_{2D} are 35 cm^{-1} and 0.7 respectively for the films deposited at slightly lower PP of 1 mbar and at fixed t_d of 10 min. This indicates that bi-layer graphene films are observed at some locations in the films. However, slight variations in number of layers at some places are also observed in each deposited films. The reason of variation in number of layers at different positions for a particular deposition condition could be the non-uniform arrival rate of carbon atoms on the surface and also possibly due to lateral diffusion of carbon atoms on the substrate as well [4, 5].

Table 5.3: Peak position, FWHM and peak intensity ratio of D, G and 2D bands for the films deposited at different deposition time at fixed T_S of 700 ^oC.

Samples	**FWHM (D band) (cm^{-1})**	**FWHM (G band) (cm^{-1})**	**FWHM (D' band) (cm^{-1})**	**Peak Pos./ FWHM (2D band) (cm^{-1})**			**I_D/I_G (using peak intensity)**	**I_G/I_{2D} (using peak intensity)**	**No. of layers (n)**	**Grain size (L_a, nm)**
Series II: deposition time variation at fixed T_S of 700 ^oC										
				2D	**$2D_1$**	**$2D_2$**				
***II_1.5 _10 min**	---	21	---	2724 /73	2696 /54	2730 /40	~ 0 **(defect free)**	3.5	≥ 20	~µm (inf)
II_1.5_ 20 min	34	21	---	2704 /45	2703 /34	2730 /34	0.06	1.5	6 - 7	280
II_1.5_ 30 min	32	23	---	2700 /27	---	---	0.15	0.4	1	112
II_1_10 min	42	22	---	2705 /35	2704 /30	2734 /28	0.04	0.7	2	420

*II_1.5_10 min: II_1.5 mbar_10 min, similarly others

Raman spectra (figure 5.9) show that, symmetrical 2D band is observed for single layer graphene, whereas it becomes asymmetrical towards higher wavenumber as the number of layer is increased (peak position shifted from 2700 cm^{-1} for single layer to 2724 cm^{-1} for ≥ 20 layers) [10, 15, 23]. The asymmetrical line shape of 2D band is further deconvoluted into two Lorentzian peaks $2D_1$ and $2D_2$, as shown in figure 5.10. The deconvoluted Raman spectra of 2D band show that, $2D_2$ peak is absent for single layer graphene; whereas with increasing number of layers, intensity of $2D_2$ band is increased. The FWHM of $2D_1$ and $2D_2$ bands are also increased with increasing number of graphene layers. Peak position and FWHM of $2D_1$ and $2D_2$ bands are listed in table 5.3.

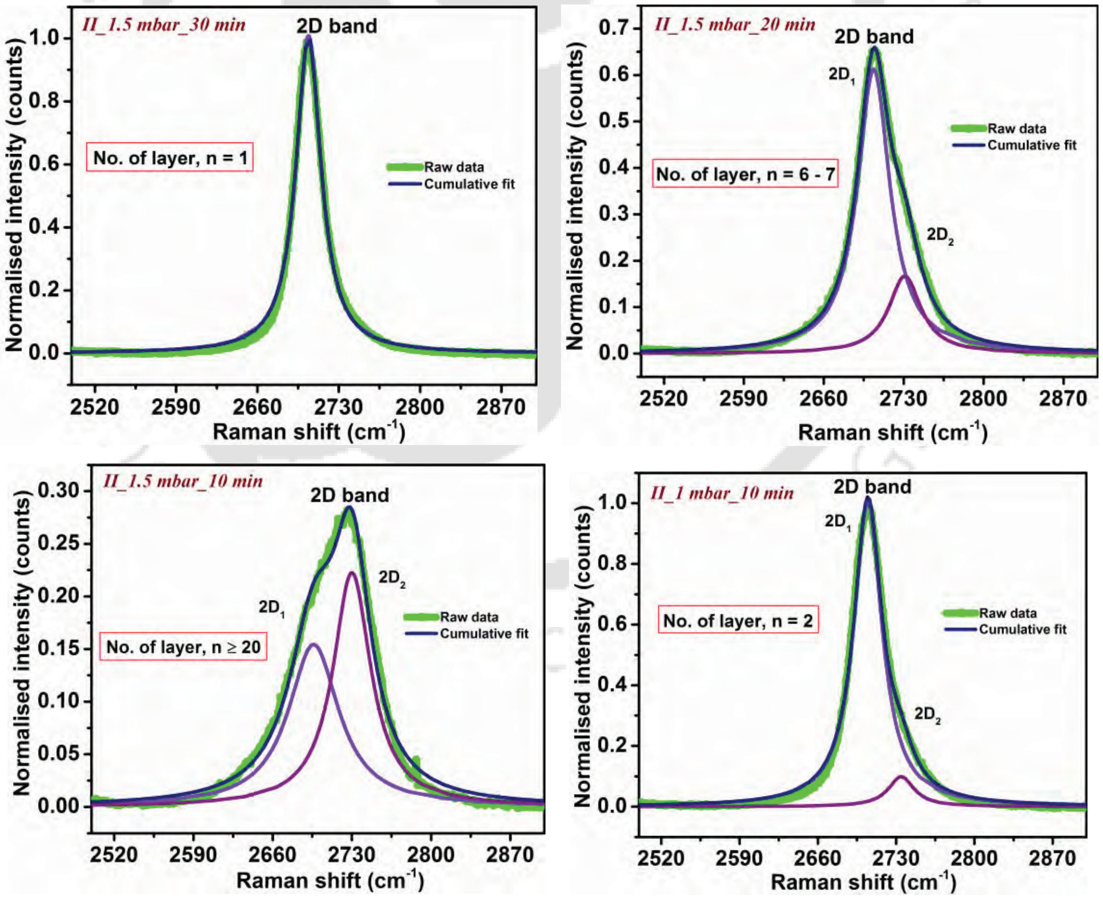

Figure 5.10: *Deconvoluted Raman spectra of 2D band with different number of layers at different* t_d *of 10, 20 and 30 min at fixed* T_S *of 700* ^oC *for the films deposited at PP of 1 and 1.5 mbar.*

5.2.3.ii TEM

Figure 5.11 shows SAED pattern and HRTEM image of graphene films transferred on TEM grid for the films deposited at PP of 1.5 mbar with different t_d of 20 and 30 min.

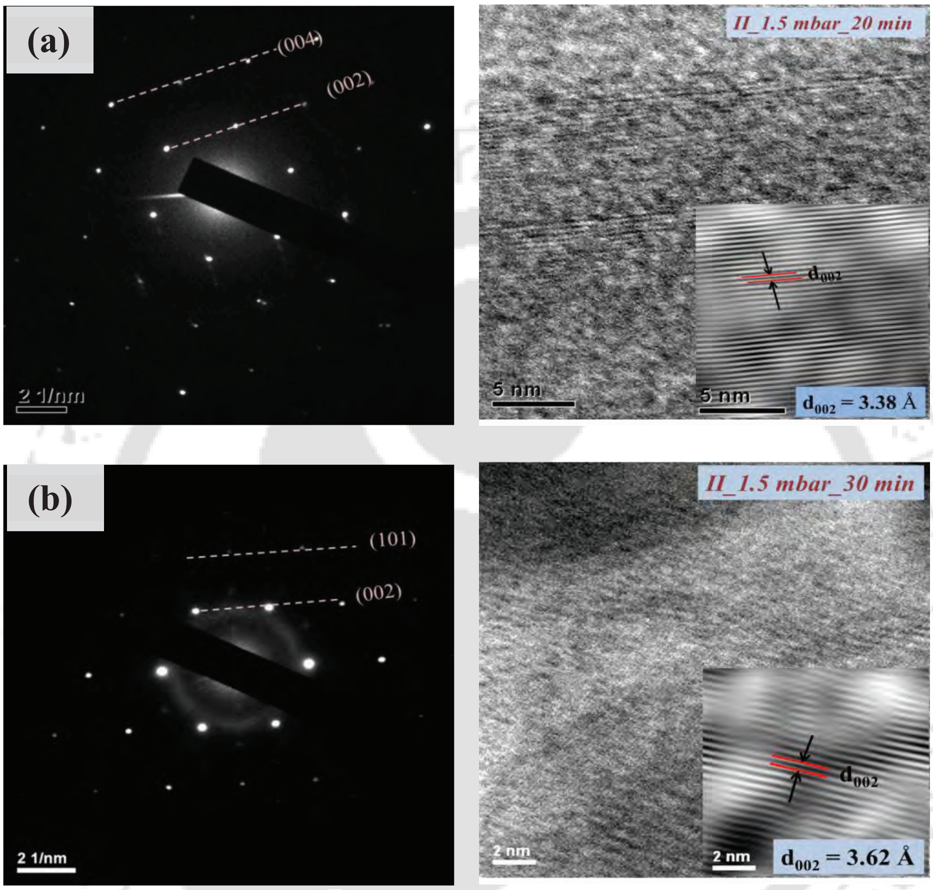

Figure 5.11: *SAED pattern (left) and HRTEM image (right) of graphene films transferred on TEM grid (Cu mesh) for the films deposited at different* t_d *of (a) 20 min and (b) 30 min at fixed PP of 1.5 mbar.*

SAED pattern of both the films shows well-oriented honeycomb structure of a few layer graphene films. The observed interplanar spacing, from SAED pattern, are 3.52, 1.94 and 1.64 Å corresponding to (002), (101) and (004) plane of graphite. From HRTEM image, we are able to see the well oriented (002) plane of graphite. HRTEM images also confirm the formation of on an average 6 to 10 layers of graphene for the films deposited at 20 min and slightly less number of layers, i.e. approximately less than 5 layers for the films deposited at 30 min. These results are also in agreement with the number of layers measured from Raman spectra. Interlayer spacing of a few layer graphene films is 3.38 Å and 3.62 Å for the films deposited at 20 and 30 min respectively, as measured from HRTEM image. However, slight variations in interlayer spacing could arise due to the twisting in graphene during transfer of the films [5, 16, 24].

5.2.4 Series III: Influence of H_2/N_2 dilution at T_S of 700 ^oC

With the optimization of deposition parameters, we are able to deposit high quality single layer graphene having large grain size (~ in µm) at several locations in the films, which is not completely uniform throughout the area of substrate. As we have observed in previous sections, low process pressure and low methane concentration are the key parameters for the growth of graphene films from multi-layers towards single layer. Therefore, in the next series of deposition for the growth of single layer graphene in large area, films were deposited at low PP of 1 mbar and comparatively low methane concentration by increasing H_2 gas flow rate. In this series, films were deposited using H_2 gas flow rate of 30 and 40 sccm and subsequent annealing at T_S of 800 ^oC for 1h after deposition for sufficient diffusion of carbon atoms into the bulk Ni foil. To study the influence of nitrogen in the growth of graphene, a few films were also deposited in the presence of N_2 gas.

5.2.4.i Raman scattering

Figure 5.12 shows the Raman spectra of graphene as deposited on Ni foil for the films deposited at different H_2/N_2 gas flow rate of 30/0, 40/0 and 30/3 sccm at fixed PP of 1 mbar. All the characteristic features such as D band, G band, D' band, 2D band, D+G band and 2D' band (discussed in section 5.2.1.ii) are observed in the Raman spectra of the films. The measured Raman spectra are deconvoluted using Lorentzian peak fit, as shown in figure 5.13. Peak position, FWHM, peak intensity ratio I_D/I_G and I_G/I_{2D} of deconvoluted Raman spectra are listed in table 5.4.

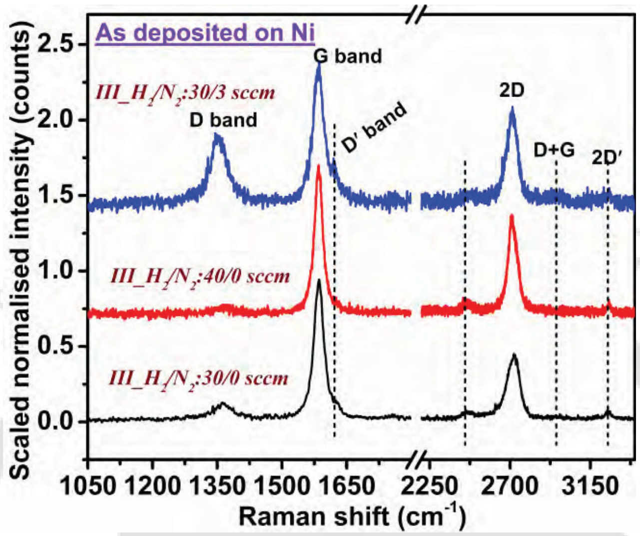

Figure 5.12: *Raman spectra of as deposited graphene on Ni foil for the films deposited at different H_2/N_2 gas flow rate of 30/0, 40/0 and 30/3 sccm at fixed PP of 1mbar.*

The deconvoluted Raman spectra show that peak intensity ratio I_G/I_{2D} is 2.11, for the films deposited at H_2 flow rate 30 sccm and it is decreased to 1.55 with increasing H_2 flow rate to 40 sccm at several locations in the films. The comparatively low value of observed peak intensity ratio I_G/I_{2D} for the films deposited at high H_2 gas flow rate in comparison to thin graphitic films (I_G/I_{2D} ~ 3 to 3.5 [2, 5] in the case of graphitic thin films) indicates that films have 5 – 10 layers of graphene throughout the deposited area with grain size in the range of 200 – 300 nm. The peak intensity ratio I_D/I_G is 0.1 and 0.06 for the films deposited at H_2 gas flow rate 30 and 40 sccm respectively. The low value of I_D/I_G indicates that graphene films have very less defects. Further, for films deposited in the presence of N_2, the peak intensity ratio I_D/I_G and FWHM of D' band are increased in comparison to films deposited in the absence of N_2. These results indicate that N atoms are incorporated with C atoms in the chain of benzene rings. This shows that it is possible to dope graphene films in order to open the band gap, which is applicable for electronic devices [25].

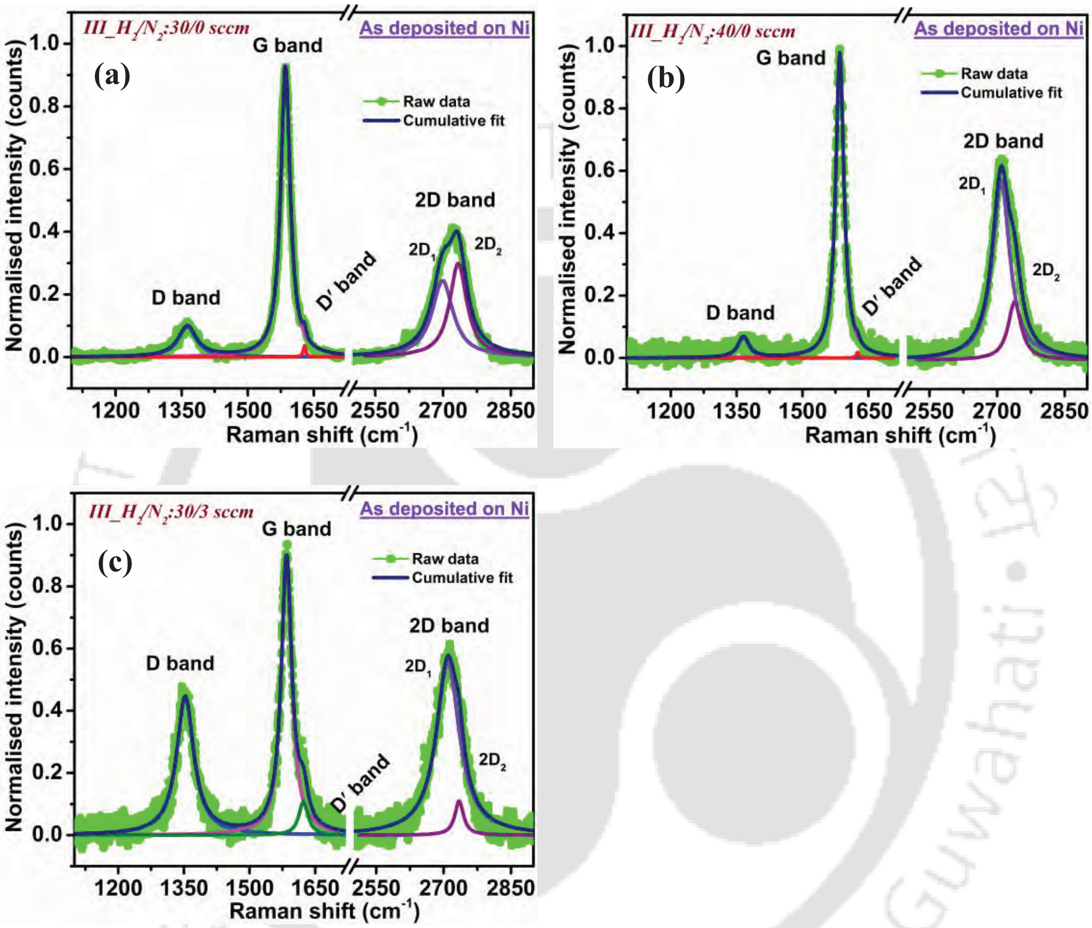

Figure 5.13: *Deconvoluted Raman spectra of as deposited graphene films on Ni foil for the films deposited at different H_2/N_2 gas flow rate of (a) 30/0 sccm, (b) 40/0 sccm and (c) 30/3 sccm at fixed PP of 1mbar.*

Further, it is observed in the Raman spectra that as deposited graphene films on Ni foil at PP of 1 mbar and H_2 gas flow rate of 20 sccm (section 5.2.3) show bi-layer graphene at some locations in the films, whereas as deposited graphene films at H_2 gas flow rate of 30 and 40 sccm (5.2.4) show on an average 5 – 10 layers of graphene in large area. These results show that with increasing H_2 concentration, the area of a few layers graphene is increased. The slight variations in number of layers at the same deposition parameters could be possibly due to other factors such as non-uniform diffusion and segregation of carbon atoms, slight variations in filament temperature, etc.

In order to obtain single layer graphene, films were transferred on quartz substrate and then sonicated for 20 min. We have observed that transparency of the films is increased after sonication. The increase in transparency of the films after sonication could be due to removal of unbonded carbon atoms resulting in single layer graphene films (on an average 1 to 5 layer) over large area, which is confirmed by Raman, AFM and UV-Vis-NIR transmission spectroscopy. Figure 5.14 shows the Raman spectra of graphene films transferred on quartz substrate followed by sonication for the films deposited at different H_2/N_2 gas flow rate of 30/0, 40/0 and 30/3 sccm at fixed PP of 1 mbar. The measured value of FWHM, peak intensity ratio I_D/I_G and I_G/I_{2D} obtained from deconvoluted Raman spectra (figure 5.15) are listed in table 5.4.

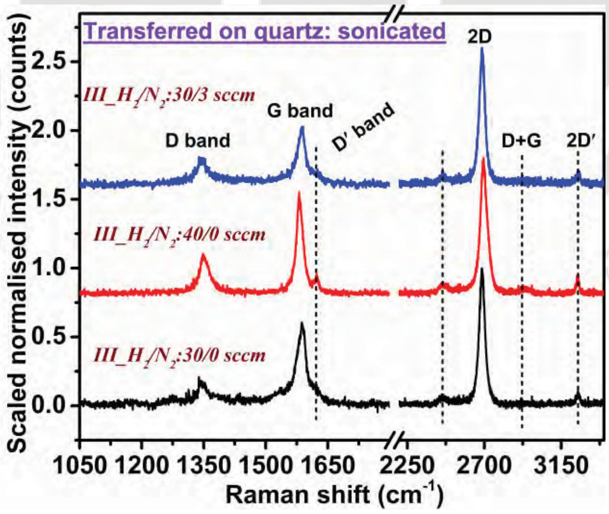

Figure 5.14: *Raman spectra of graphene films transferred on quartz substrate followed by sonication for the films deposited at different* H_2/N_2 *gas flow rate of 30/0, 40/0 and 30/3 sccm at fixed PP of 1 mbar.*

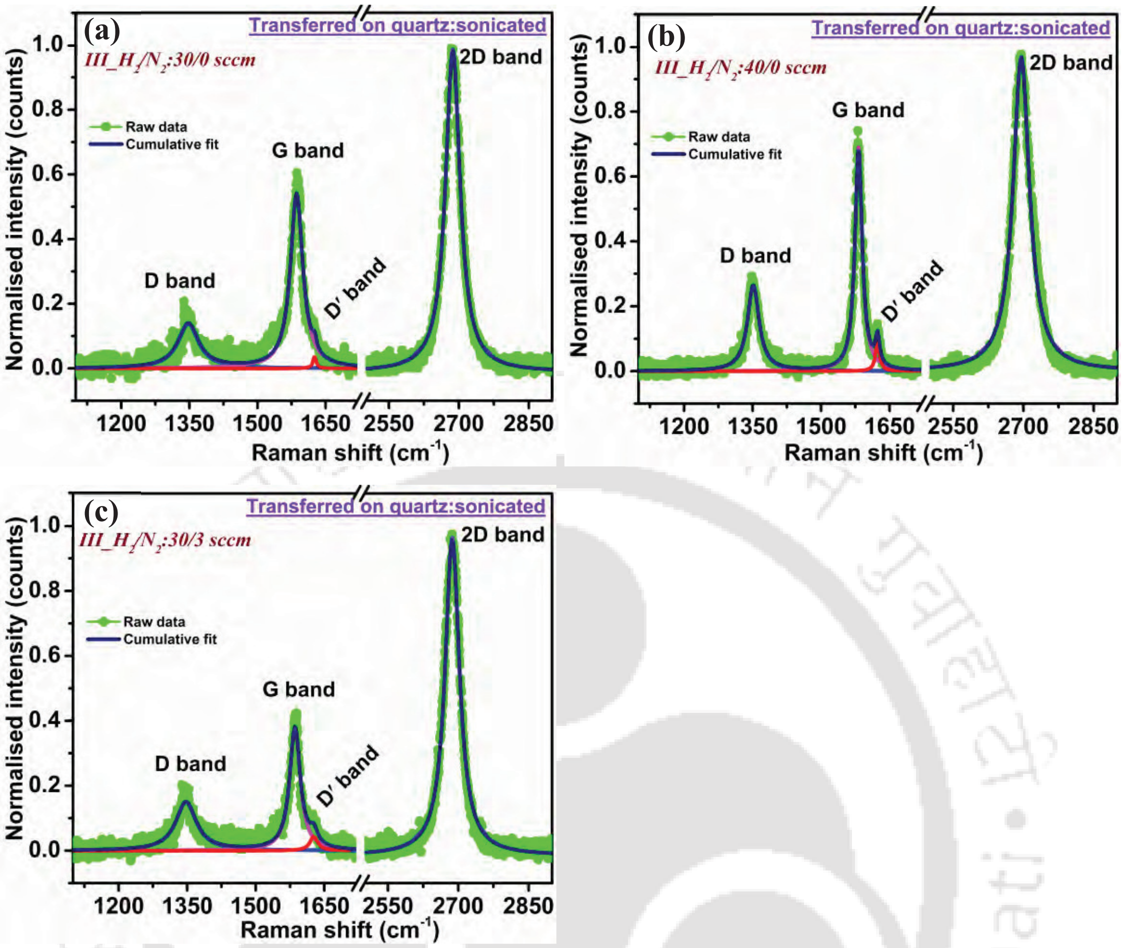

Figure 5.15: *Deconvoluted Raman spectra of graphene films transferred on quartz substrate followed by sonication for the films deposited at different H_2/N_2 gas flow rate of (a) 30/0 sccm, (b) 40/0 sccm and (c) 30/3 sccm at fixed PP of 1 mbar.*

The peak intensity ratio I_G/I_{2D} and FWHM of 2D band of graphene films transferred on quartz substrate are in the range of 0.4 – 0.7 and 37 – 42 respectively, which indicates the presence of 1 to 2 layers of graphene in all sonicated films. However, a slight increase in peak intensity ratio I_D/I_G is observed after sonication. This indicates that some defects are produced in the films during sonication and as a result grain size of single and bi-layer graphene films is reduced to 40 – 70 nm.

Table 5.4: Peak position, FWHM and peak intensity ratio of D, G and 2D bands for the films deposited at different H_2/N_2 dilution at fixed T_S of 700 ^oC.

Samples	**FWHM (D band) (cm^{-1})**	**FWHM (G band) (cm^{-1})**	**FWHM (D' band) (cm^{-1})**	**Peak Pos./ FWHM (2D band) (cm^{-1})**			**I_D/I_G (using peak intensity)**	**I_G/I_{2D} (using peak intensity)**	**No. of layers (n)**	**Grain size (L_a, nm)**
Series III: H_2/N_2 dilution at T_S of 700 ^oC										
Graphene films as deposited on Ni										
				2D	**$2D_1$**	**$2D_2$**				
III_H_2 /N_2:30/0	49	25	7	2718 /76	2698 /56	2733 /46	0.10	2.11	~8-10	168
III_H_2/ N_2:40/0	31	22	7	2713 /56	2708 /46	2738 /35	0.06	1.55	~5-7	280
III_H_2/ N_2:30/3	47	28	25	2711 /66	2709 /61	2734 /23	0.49	1.47	~5-7	34
Graphene films transferred on quartz and sonicated										
III_H_2/ N_2:30/0	55	32	9	2687 /37	---	---	0.24	0.54	1	70
III_H_2/ N_2:40/0	30	18	10	2695 /42	---	---	0.37	0.70	~1-2	45
III_H_2/ N_2:30/3	54	28	20	2687 /37	---	---	0.39	0.40	1	43

5.2.4.ii AFM

Figure 5.16 shows AFM images of graphene films (series III) transferred on quarts substrate followed by sonication for the films deposited at different H_2/N_2 gas flow rate of 30/0, 40/0 and 30/3 sccm. AFM images show that, graphene films are uniform in approximately 1 to 2 μm dimension having thickness in the range of 1 – 5 nm. Therefore, from the surface height profile of graphene films, we can also conclude that graphene films have approximately 1 to 8 layers in the large area of micron dimensions.

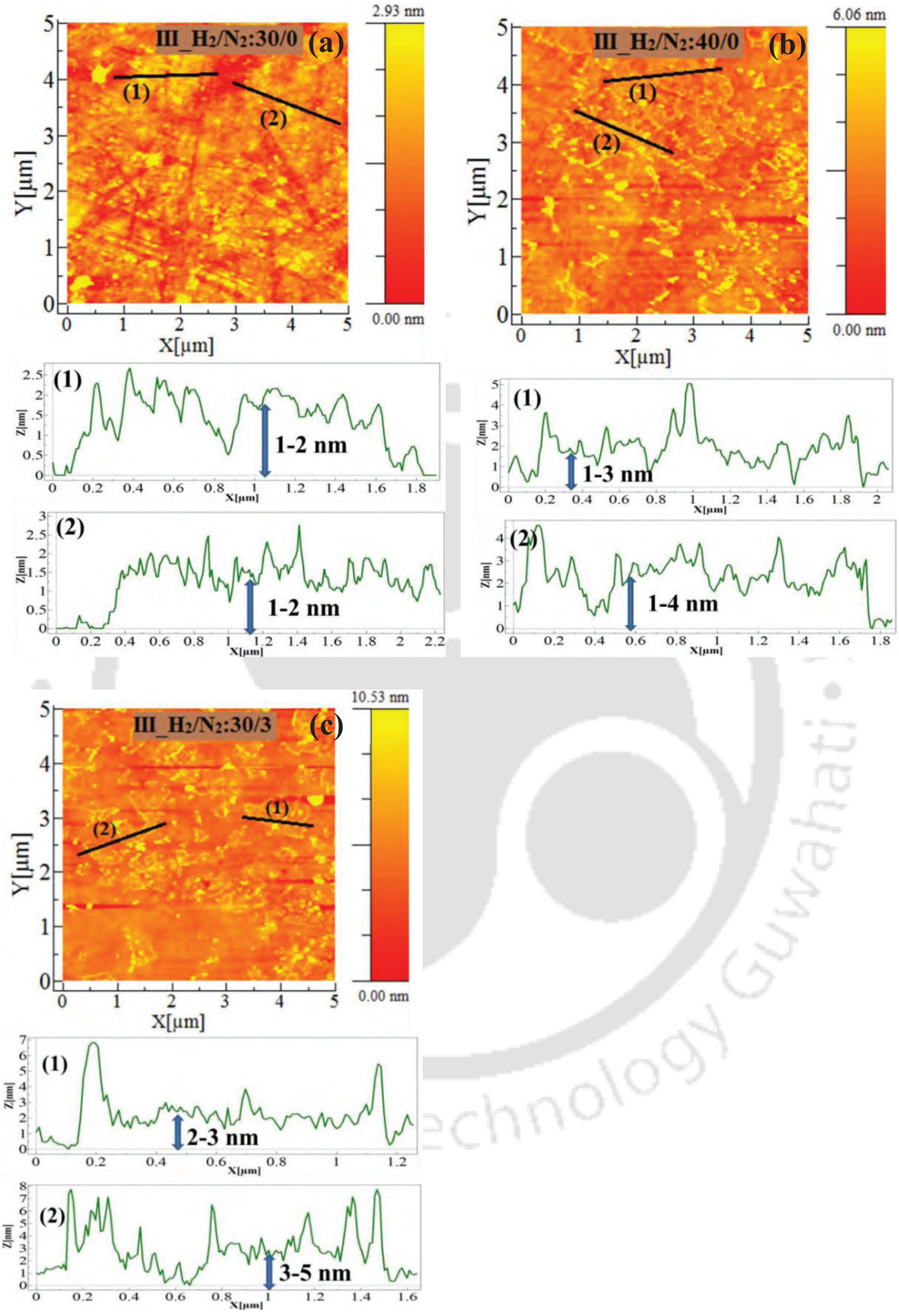

__Figure 5.16:__ AFM image and corresponding surface height profile of graphene films transferred on quartz substrate followed by sonication for the films deposited at different H_2/N_2 *gas flow rate of (a) 30/0 sccm, (b) 40/0 sccm and (c) 30/3 sccm at fixed PP of 1mbar.*

5.3 Optical properties of graphitic thin films

5.3.1 UV-Vis-NIR transmittance

Figure 5.17 shows transmission spectra of graphene films (series III) transferred on quartz substrate before and after sonication for the films deposited at different H_2/N_2 gas flow rate 30/0, 40/0 and 30/3 sccm. Transmission spectra were taken using blank quartz substrate as reference. From the spectra, we have observed that transparency of as transferred (without sonication) graphene films is in the range of 40 – 50 % in the visible region at 550 nm, which is increased to ~ 85 – 90 % after sonication. The high transparency of graphene shows that films are uniform over entire area of the surface. The photographic camera image of sonicated graphene films on quartz substrate are shown in figure 5.18. We can see the transparency of the films from the word “IIT” which is written on the back of the quartz substrates. Since, single layer graphene films absorb about 2.3% of incident light [2, 13, 26-28], therefore high transparency of sonicated films further confirms the formation of 1 to 6 layers of large area graphene films. A strong absorption at 268 nm is observed corresponding to $\pi \rightarrow \pi^*$ transition of C-C/C=C bond [29, 30].

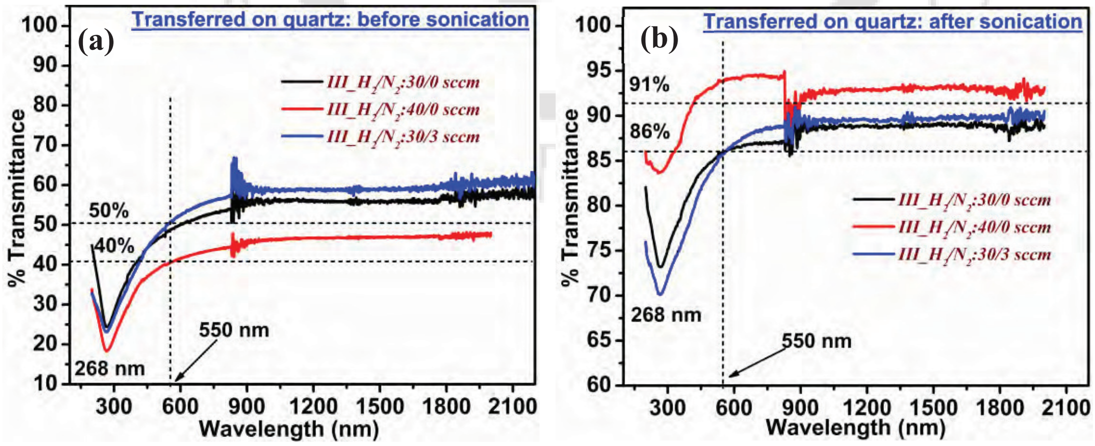

Figure 5.17: *UV-Vis-NIR transmission spectra of graphene films transferred on quartz substrate (a) before and (b) after sonication for the films deposited at different* H_2/N_2 *gas flow rate of 30/0, 40/0 and 30/3 sccm.*

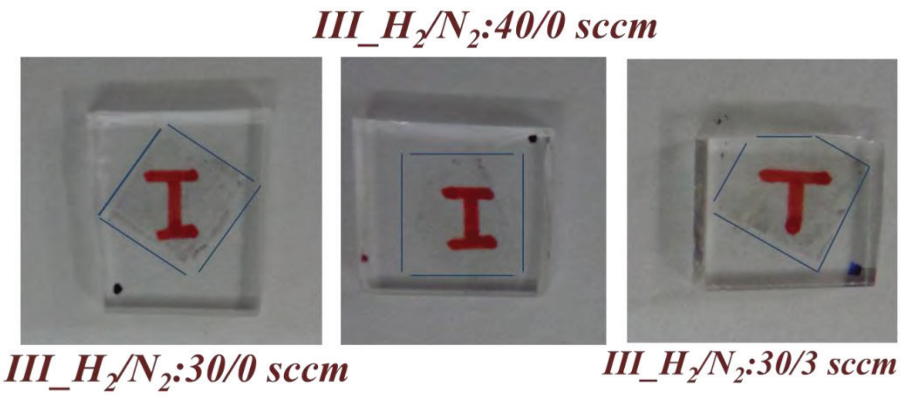

Figure 5.18: *Photographic camera image of graphene films transferred on quartz substrate after sonication for the films deposited at different* H_2/N_2 *gas flow rate. (Word "IIT" is written on the back side of the substrates for visualization of transparency of the films).*

5.3.2 Third order optical nonlinear refractive index coefficient

To study the optical nonlinearity of graphitic thin films prepared by HFCVD method, films prepared in series I_A for the films deposited at PP and t_d of 2 mbar and 10 min respectively and at T_S of 600 °C (HW149) are used. Third order optical nonlinear refractive index coefficient (n_2) of graphitic thin films was measured by close aperture configuration using single beam Z-scan technique after transfer of the films on quartz substrate (without sonication). Thickness of the films was 56 ± 8 nm, as measured by Stylus profilometer. Figure 5.19 shows the normalized transmission spectra of the films with respect to sample position (± z-axis). The ray diagram of close aperture Z-scan technique is shown in chapter 2 (figure 2.5). The decrease and increase in transmittance near the focus (z=0), due to decrease and increase in number of photons to the detector plane resulting in the valley followed by the peak, indicates positive nonlinearity of graphitic thin films. The transmittance profile as a function of on-axis sample position (±

z-axis) in closed aperture Z-scan is given by [31-33].

$$T(z,\Delta\phi) = 1 + \frac{4x\Delta\phi}{(x^2+1)(x^2+9)}, where\ x = \frac{z}{z_0} \quad \ldots\ldots\ldots\ldots\ldots\ldots\ldots\ldots (5.1)$$

Nonlinear phase shift ($\Delta\phi$) is determined by $\Delta\phi = 2\pi n_2 I_0 L_{eff}/\lambda$

Where, I_0 (=7.46 x 10^3 W/cm^2) is the light intensity on the sample at the focus (z=0) and L_{eff} is the effective thickness of the sample. Using the approximation Leff=L, equation (1) can be simplified as:

$$T(z) = 1 + \frac{az}{(1+bz^2)(9+bz^2)} \quad \ldots\ldots\ldots\ldots\ldots\ldots\ldots\ldots\ldots\ldots\ldots\ldots\ldots\ldots (5.2)$$

Where, $a = 4\Delta\phi/z_0 = 1.1845 \times 10^{10} n_2 L_{eff}$ and $b = 1/z_0^2$

z_0 (=2.5 mm) is the Rayleigh length of laser beam.

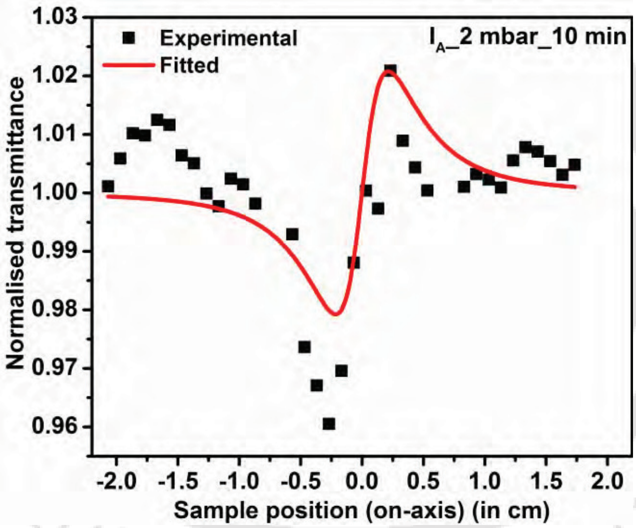

Figure 5.19: *Nonlinear transmission spectra of graphitic thin film deposited at PP of 2 mbar, t_d of 10 min and T_S of 600 °C.*

Nonlinear refractive index coefficient (n_2) of graphitic thin films was found to be 2.46 x 10^{-5} cm^2/W. The observed nonlinear refractive index coefficient is slightly in agreement with the values reported in literature. Zhang et al. [31] have reported non-linear refractive index of graphene of the order of ~ 10^{-7} cm^2/W with laser wavelength of 1550 nm.

5.4 Electrical properties of graphitic thin films

5.4.1 Room temperature I-V characteristics

Figure 5.20 shows the resistance of graphene films using two probes I-V characteristics for the films deposited at different H_2/N_2 gas flow rate of 30/0, 40/0 and 30/3 sccm. The measurements were performed on transferred graphene films on quartz substrate after sonication. Small dots of silver paste were used as electrodes with electrodes separation of ~ 8 μm. We have observed that, the resistance of all the films is in the range of 500 – 1200 ohm. These results show that graphene films are continuous in large dimension (~ in the range of μm). However, the slight change in resistance in different films could be due to variation in H_2 concentration during deposition or due to presence of defects in the films, which results in the variation of resistance [27, 34].

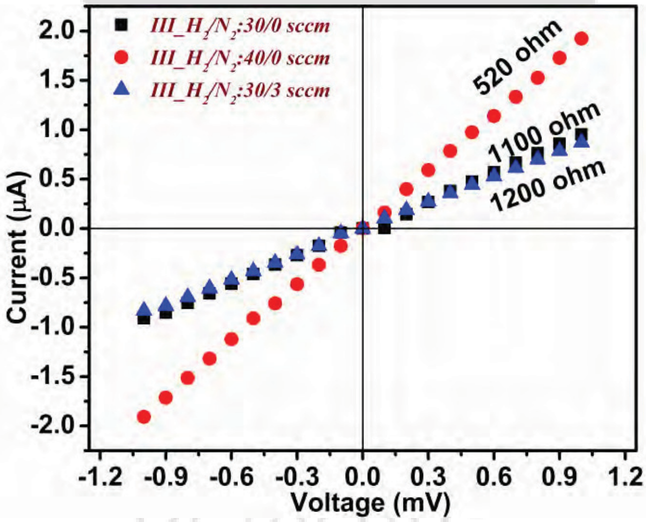

Figure 5.20: *Resistance of graphene for the films deposited at different H_2/N_2 gas flow rate of 30/0, 40/0 and 30/3 sccm.*

5.5 Influence of excitation wavelength and temperature on Raman spectra of single/multi - layers graphene films

As we have observed that for the films deposited with high dilution of H_2/N_2 gas flow rate and followed by sonication, the area of single / a few layer graphene films is increased to a few mm^2 size (figure 5.17, transmission spectra of graphene). Due to large area (~ 1cm) deposition of graphene films on Ni foil, different layer of graphene are observed at different locations of the films. In this section, we have studied the variation in peak position and FWHM in the Raman spectra of D/G/2D band with different number of graphene layers. In order to study these variations with different number of layers, Raman spectra were recorded for the films deposited at H_2/N_2 gas flow rate of 40/0 sccm at several locations of the films. The number of layers is estimated using peak intensity ratio of G and 2D band (I_G/I_{2D}). Measurements were performed after transfer of the films on quartz substrate followed by sonication. In this section we have also studied the effect of different excitation wavelength (laser energy) as well as effect of temperature on the Raman spectra of G/D/2D bands at given location in the film.

5.5.1 Variation in peak position and FWHM of G / 2D bands with number of layers

Figure 5.21 shows the Raman spectra of different graphene layers with laser wavelength of 632.8 nm. Peak position and FWHM of G and 2D bands vary with different number of layers. The variation in peak position and FWHM of G and 2D band with different number of layers are shown in figure 5.22. Here, it is observed that, peak position and FWHM of G and 2D bands are changed significantly only up to a few layers (approximately from single layer to a few 7-8 layers) and beyond this very small variation is observed. The number of layers is estimated using peak intensity ratio I_G/I_{2D}, also shown in figure 5.22. The peak position of G and 2D band for single layer graphene is 1588 and 2643 cm^{-1} respectively. However, in the case of multi-layers graphene films ($n \geq 20$), peak position of G band is shifted towards lower wavenumber side by 6 cm^{-1} and peak position of 2D band is shifted towards higher wavenumber side by 15 cm^{-1}. FWHM of G and 2D bands for single layer graphene are 15 and 35 cm^{-1} and it is increased to 21 and 51 cm^{-1} respectively for multi-layers graphene thin films, which is consistent with the results reported in literature [1, 2, 4, 15].

For the study of line shape broadening (symmetric/asymmetric) of 2D band with different number of layers, 2D bands are further deconvoluted into two Lorentzian peaks, as shown in figure 5.21 (b). From figure 5.21 (b), it is clear that in case of single layer graphene, the line shape of 2D band is symmetric. Whereas, with increasing number of layers, the line shape of 2D band is broadened and starts to increase asymmetry towards higher wavenumber side. The asymmetry of 2D band is caused by the increase in intensity of deconvoluted peak $2D_2$ in comparison to $2D_1$ with increasing number of graphene layers.

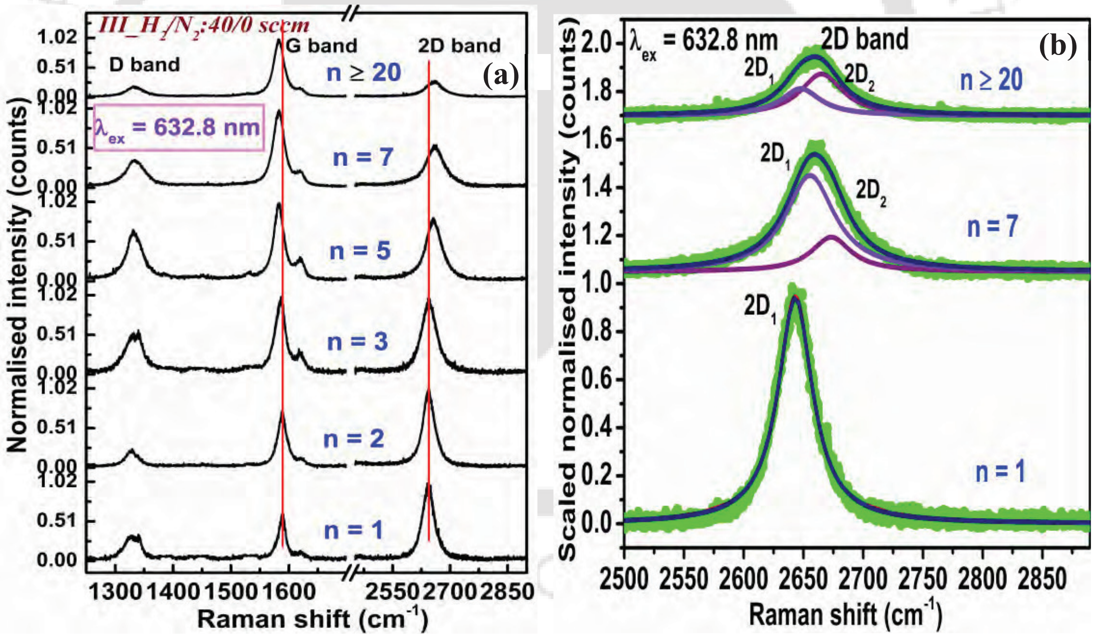

Figure 5.21: *(a) Raman spectra of different layers of graphene with excitation wavelength of 632.8 nm and (b) deconvoluted Raman spectra of 2D band.*

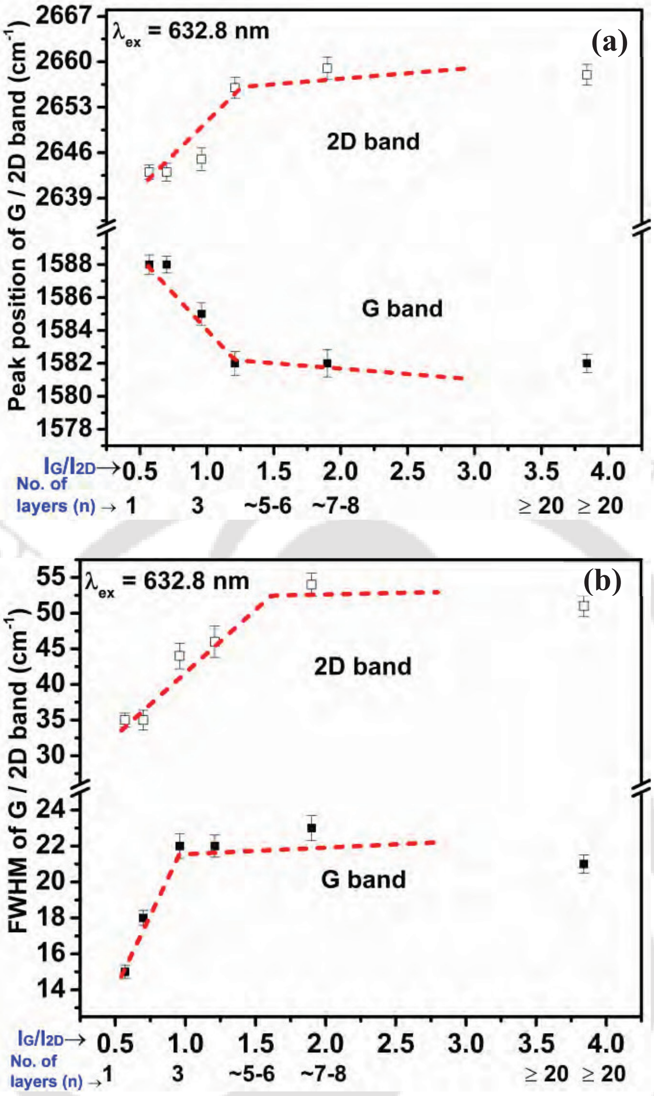

Figure 5.22: *Shift in (a) peak position and (b) FWHM of G and 2D bands with different number of layers at excitation wavelength of 632.8 nm. (Dotted lines are only for the guide line).*

5.5.2 Effect of excitation wavelength

Figure 5.23 shows the Raman spectra of single, tri and multi layers graphene films with three different excitation wavelengths of 488, 514.53 and 632.8 nm. It is observed that with increasing excitation laser energy (E_L), the peak position of D and 2D bands are shifted towards higher wavenumber side for all the different number of layers. However, no shift is observed in the peak position of G band. The peak position of D and 2D band for single layer graphene are 1330 and 2643 cm^{-1} respectively with an excitation wavelength of 632.8 nm (excitation energy 1.95 eV) and it is shifted towards higher wavenumber side 1358 and 2706 cm^{-1} respectively, with increasing excitation energy of 2.54 eV (laser wavelength 488 nm), which is also consistent with the results reported in literature [10, 11, 35, 36]. The observed frequency shift in the Raman spectra of D and 2D band with different laser excitation energy are shown in figure 5.24. This shows that D and 2D bands are highly dispersive in nature with a slope of 55±2 and 114±3 cm^{-1}/eV respectively for single layer graphene. The approximate similar laser energy dependence on the frequency shift of Raman D and 2D bands is observed for tri-layers and multi-layers (n ~10-15 layers) graphene films. The origin and dispersive behavior in the frequency of D and 2D bands originate from a double resonance Raman process [10, 11, 36, 37]. In the double resonance process, coupling between phonon wave-vector q and electronic state with wave-vector k take place near the Dirac K-point of the Brillouin zone. Therefore, with increasing laser energy (E_L), the resonance k wave-vector of electron moves away from the Dirac K-point and phonons farther from K-point are required for momentum conservation. As a results, phonon wave-vector q moves towards higher wavenumber side with increasing excitation energy [10, 23, 38].

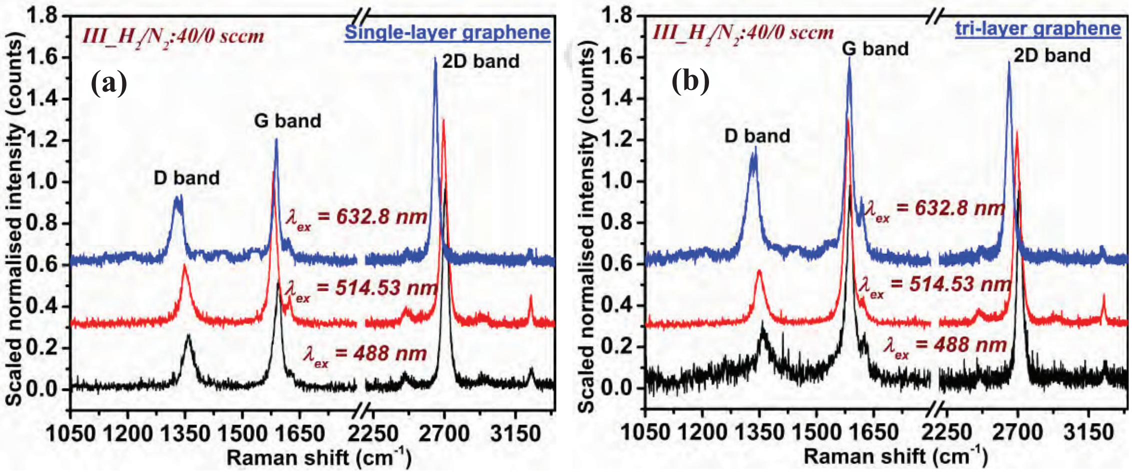

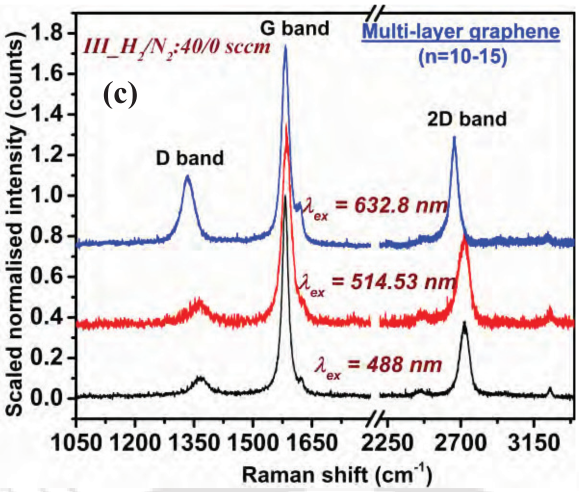

Figure 5.23: *Raman spectra of (a) single layer, (b) tri layers and (c) multi-layers graphene films at different excitation wavelength of 488, 514.53 and 632.8 nm.*

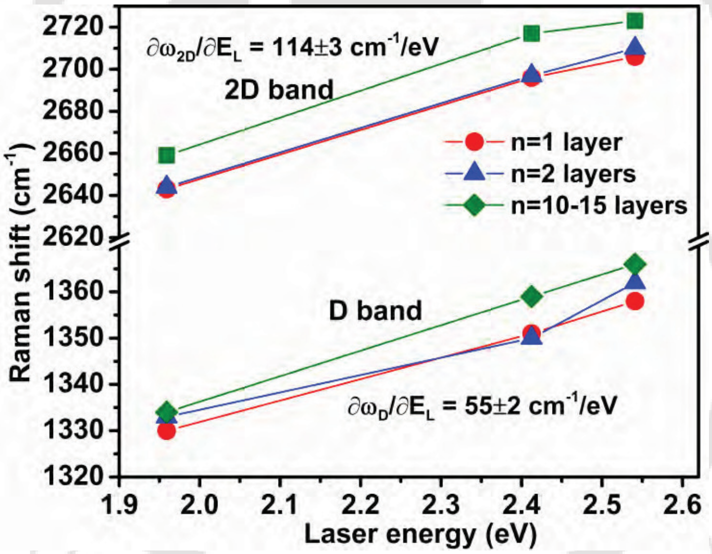

Figure 5.24: *Frequency dependence of D (ω_D) and 2D (ω_{2D}) bands on laser energy (E_L).*

5.5.3 Temperature dependent Raman spectra of single layer graphene

Temperature dependent Raman scattering was studied on single layer graphene films transferred on flint glass substrate (~ 200 µm, thick). The transferred films were sonicated before this measurement. The flint glass substrate was chosen to reduce the temperature difference between sensor and surface of the films. Raman spectra were recorded with an excitation wavelength of 488 nm. Figure 5.25 shows the temperature dependent Raman spectra of single layer graphene for different temperature ranging from -180 °C to 20 °C at a step of 10 °C. As we can see from the figure 5.25, no change is observed in relative peak intensity of D and G bands with increasing temperature, which indicates that single layer graphene films are quite stable with temperature. The influence of temperature on the peak position of different vibrational modes of carbon can be observed from the Raman spectra. Figure 5.26 (a) and (b) show the shift in peak position of G and 2D bands respectively. The peak position of G band is shifted towards lower wavenumber side (i.e. red shift) with increasing temperature, whereas 2D band does not show any shift. The reason of slight variation in peak position of G band with temperature could be due to the change in elastic modulus which can occur from the change in interatomic distance due to thermal expansion/contraction and anharmonic terms in lattice potential energy which could result in anharmonic coupling of phonon modes [11, 39, 40].

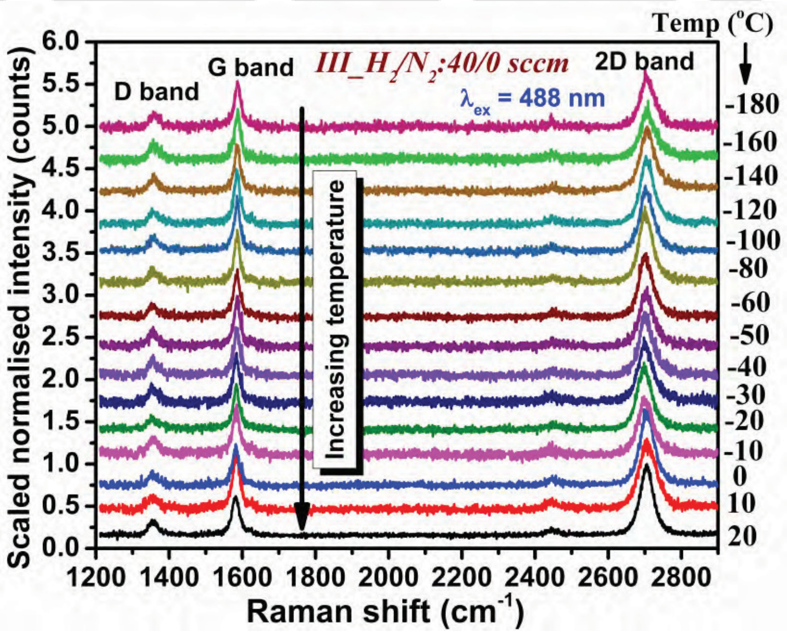

Figure 5.25: *Temperature dependent Raman spectra of single layer graphene from -180 to 20 °C.*

Figure 5.27 (a) show the variation of FWHM of G and 2D bands with respect to change in temperature. The variation in FWHM of both the phonon modes shows similar behavior in the measured temperature range from -180 ^{o}C to 20 ^{o}C. In both the phonon modes, FWHM remains more or less constant as the temperature is increased from -180 ^{o}C to -60 ^{o}C. However, with the increase in temperature from -60 ^{o}C to 20 ^{o}C, the FWHM is found to increase by ~ 5 cm^{-1}.

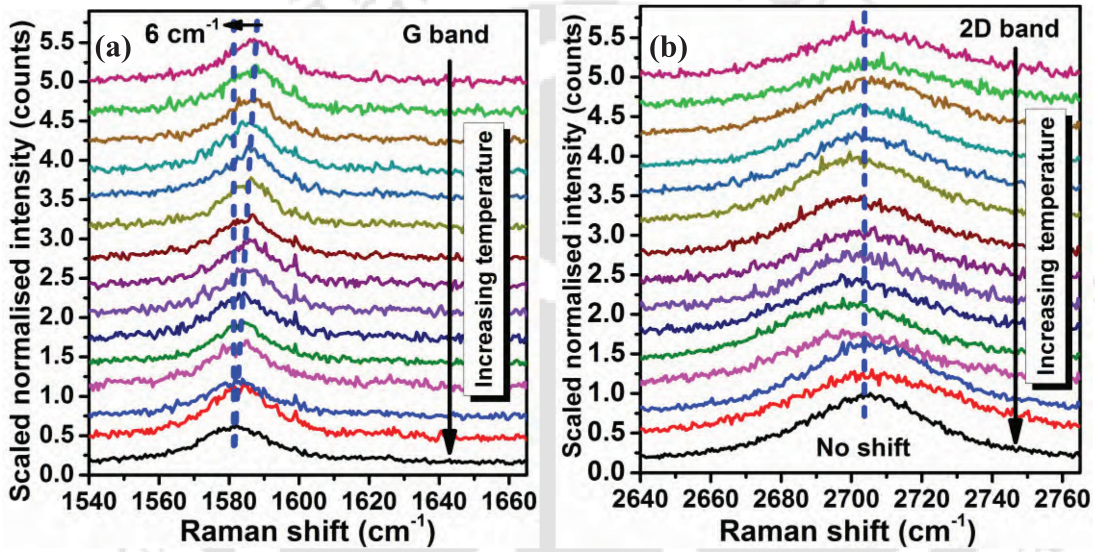

Figure 5.26: *Temperature dependent shift in peak position of (a) G band and (b) 2D band of single layer graphene.*

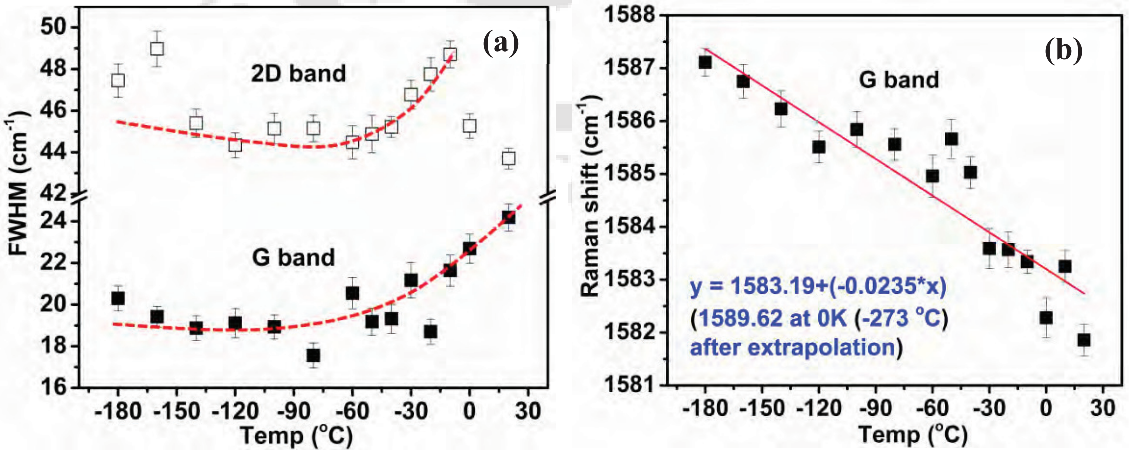

Figure 5.27: *(a) FWHM of G and 2D band of single layer graphene at different temperature and (b) shift in peak position of G band with increasing temperature from -180 to 20 ^{o}C. (Dashed lines are only for guide line and solid line represents linear fit).*

The shift in peak position of G band with temperature can be expressed by the following relation;

$$\omega = \omega_0 + \chi T \quad \ldots\ldots\ldots\ldots\ldots\ldots\ldots\ldots\ldots\ldots\ldots\ldots\ldots\ldots \quad (5.3)$$

where, ω_0 is the frequency of G band at temperature T=0 K (extrapolated) and χ is the first order temperature coefficient. The extracted value of first order temperature coefficient (χ), from figure 5.27 (b), for single layer graphene is -0.023 ± 0.002 cm^{-1}/K, which is in agreement with the results reported in literature [40-42].

5.6 Conclusion

Large area (~ in the dimension of μm) defects free single and multi-layers graphene films were successfully deposited on Ni foil by HFCVD method, which is relatively new technique for the growth of large area high quality graphene films. Graphene films are transferred on different substrates such as quartz and Si, using the method of chemical etching, which is important for the device fabrication on any substrates. The transferred graphene films show structural properties approximately similar to as deposited films on Ni foil. This indicates that films are successfully transferred on other substrates. We have studied the influence of different deposition parameters, in order to deposit defect free graphene, such as process pressure, substrate temperature, deposition time and $CH_4/H_2/N_2$ gas flow rate variations on structural properties of the films. Structural properties of the films were studied by FESEM, AFM, TEM and Raman scattering. From the analysis of structural properties of graphene for the films deposited at different deposition parameters, we have observed that low process pressure, high substrate temperature and low methane gas concentration are the key parameters for the growth of large area single layer graphene. As we have seen that from the optimization of deposition parameters, films have less defects at relatively low T_S of 600 ^oC, which is advantage of HFCVD method where precursor gases are dissociated at very high filament temperature (~ 2100 ^oC). We have also studied the effect of N_2 on the growth of graphene films. The incorporation of N atoms with graphene can be seen from the enhancement in the peak intensity ratio I_D/I_G in comparison to pure graphene films. However, further investigation is needed to study the N_2 doping in graphene films. We have studied the influence of different excitation laser energy in the range of 1.95 – 2.54 eV and effect of temperature in the range of -180 to 20 ^oC on single layer graphene. With the increase in excitation energy, blue shifts are observed in the peak position of D and 2D band, whereas with the increase in temperature from -180 to 20 ^oC, red shift is observed in the peak position of G band and no shift is observed in the peak positions of D and 2D band. Thus from the above observations, we can conclude that HFCVD is very good technique for the growth of defects free graphene at relatively low substrate temperature in comparison to other CVD technique.

5.7 References

[1] H.J. Park, J. Meyer, S. Roth, V. Skákalová, Growth and properties of few-layer graphene prepared by chemical vapor deposition, Carbon, 48 (2010) 1088-1094.

[2] L. Huang, Q.H. Chang, G.L. Guo, Y. Liu, Y.Q. Xie, T. Wang, B. Ling, H.F. Yang, Synthesis of high-quality graphene films on nickel foils by rapid thermal chemical vapor deposition, Carbon, 50 (2012) 551-556.

[3] A.V. Tyurnina, K. Tsukagoshi, H. Hiura, A.N. Obraztsov, Structural and charge transport characteristics of graphene layers obtained from CVD thin film and bulk graphite materials, Carbon, 52 (2013) 49-55.

[4] S. Amini, J. Garay, G. Liu, A.A. Balandin, R. Abbaschian, Growth of large-area graphene films from metal-carbon melts, Journal of Applied Physics, 108 (2010) 094321.

[5] Q. Yu, J. Lian, S. Siriponglert, H. Li, Y.P. Chen, S.-S. Pei, Graphene segregated on Ni surfaces and transferred to insulators, Applied Physics Letters, 93 (2008) 113103.

[6] C. Faugeras, A. Nerrière, M. Potemski, A. Mahmood, E. Dujardin, C. Berger, W.A. de Heer, Few-layer graphene on SiC, pyrolitic graphite, and graphene: A Raman scattering study, Applied Physics Letters, 92 (2008) 011914.

[7] J. Maultzsch, S. Reich, C. Thomsen, Double-resonant Raman scattering in graphite: Interference effects, selection rules, and phonon dispersion, Physical Review B, 70 (2004) 155403.

[8] A. Kaniyoor, S. Ramaprabhu, A Raman spectroscopic investigation of graphite oxide derived graphene, AIP Advances, 2 (2012) 032183.

[9] H. Zhou, C. Qiu, F. Yu, H. Yang, M. Chen, L. Hu, Y. Guo, L. Sun, Raman scattering of monolayer graphene: the temperature and oxygen doping effects, Journal of Physics D: Applied Physics, 44 (2011) 185404.

[10] L.M. Malard, M.A. Pimenta, G. Dresselhaus, M.S. Dresselhaus, Raman spectroscopy in graphene, Physics Reports, 473 (2009) 51-87.

[11] R. Beams, L.G. Cançado, L. Novotny, Raman characterization of defects and dopants in graphene, Journal of Physics: Condensed Matter, 27 (2015) 083002.

[12] F. Tuinstra, J.L. Koenig, Raman Spectrum of Graphite, The Journal of Chemical Physics, 53 (1970) 1126-1130.

[13] L. Gao, W. Ren, J. Zhao, L.-P. Ma, Z. Chen, H.-M. Cheng, Efficient growth of high-quality graphene films on Cu foils by ambient pressure chemical vapor deposition, Applied Physics Letters, 97 (2010) 183109.

[14] B.-J. Lee, T.-W. Lee, S. Park, H.-Y. Yu, J.-O. Lee, S.-H. Lim, G.-H. Jeong, Low-temperature synthesis of thin graphite sheets using plasma-assisted thermal chemical vapor deposition system, Materials Letters, 65 (2011) 1127-1130.

[15] A. Gupta, G. Chen, P. Joshi, S. Tadigadapa, Eklund, Raman Scattering from High-Frequency Phonons in Supported n-Graphene Layer Films, Nano Letters, 6 (2006) 2667-2673.

[16] Y. Kim, W. Song, S.Y. Lee, C. Jeon, W. Jung, M. Kim, C.-Y. Park, Low-temperature synthesis of graphene on nickel foil by microwave plasma chemical vapor deposition, Applied Physics Letters, 98 (2011) 263106.

[17] A.C. Ferrari, J.C. Meyer, V. Scardaci, C. Casiraghi, M. Lazzeri, F. Mauri, S. Piscanec, D. Jiang, K.S. Novoselov, S. Roth, A.K. Geim, Raman Spectrum of Graphene and Graphene Layers, Physical Review Letters, 97 (2006) 187401.

[18] A. Reina, X. Jia, J. Ho, D. Nezich, H. Son, V. Bulovic, M.S. Dresselhaus, J. Kong, Large Area, Few-Layer Graphene Films on Arbitrary Substrates by Chemical Vapor Deposition, Nano Letters, 9 (2009) 30-35.

[19] J.J. Lander, H.E. Kern, A.L. Beach, Solubility and Diffusion Coefficient of Carbon in Nickel: Reaction Rates of Nickel-Carbon Alloys with Barium Oxide, Journal of Applied Physics, 23 (1952) 1305-1309.

[20] T. Yamada, M. Ishihara, J. Kim, M. Hasegawa, S. Iijima, A roll-to-roll microwave plasma chemical vapor deposition process for the production of 294 mm width graphene films at low temperature, Carbon, 50 (2012) 2615-2619.

[21] T. Yamada, M. Ishihara, M. Hasegawa, Large area coating of graphene at low temperature using a roll-to-roll microwave plasma chemical vapor deposition, Thin Solid Films, 532 (2013) 89-93.

[22] M.S. Dresselhaus, A. Jorio, A.G. Souza Filho, R. Saito, Defect characterization in graphene and carbon nanotubes using Raman spectroscopy, Philosophical Transactions of the Royal Society of London A: Mathematical, Physical and Engineering Sciences, 368 (2010) 5355-5377.

[23] A.C. Ferrari, Raman spectroscopy of graphene and graphite: Disorder, electron–phonon coupling, doping and nonadiabatic effects, Solid State Communications, 143 (2007) 47-57.

[24] C. Soldano, A. Mahmood, E. Dujardin, Production, properties and potential of graphene, Carbon, 48 (2010) 2127-2150.

[25] Y. Sui, B. Zhu, H. Zhang, H. Shu, Z. Chen, Y. Zhang, Y. Zhang, B. Wang, C. Tang, X. Xie, G. Yu, Z. Jin, X. Liu, Temperature-dependent nitrogen configuration of N-doped graphene by chemical vapor deposition, Carbon, 81 (2015) 814-820.

[26] R.R. Nair, P. Blake, A.N. Grigorenko, K.S. Novoselov, T.J. Booth, T. Stauber, N.M.R. Peres, A.K. Geim, Fine Structure Constant Defines Visual Transparency of Graphene, Science, 320 (2008) 1308-1308.

[27] X. Li, Y. Zhu, W. Cai, M. Borysiak, B. Han, D. Chen, R.D. Piner, L. Colombo, R.S. Ruoff, Transfer of Large-Area Graphene Films for High-Performance Transparent Conductive Electrodes, Nano Letters, 9 (2009) 4359-4363.

[28] J. Kim, M. Ishihara, Y. Koga, K. Tsugawa, M. Hasegawa, S. Iijima, Low-temperature synthesis of large-area graphene-based transparent conductive films using surface wave plasma chemical vapor deposition, Applied Physics Letters, 98 (2011) 091502.

[29] S. Saxena, T.A. Tyson, S. Shukla, E. Negusse, H. Chen, J. Bai, Investigation of structural and electronic properties of graphene oxide, Applied Physics Letters, 99 (2011) 013104.

[30] F.T. Thema, M.J. Moloto, E.D. Dikio, N.N. Nyangiwe, L. Kotsedi, M. Maaza, M. Khenfouch, Synthesis and Characterization of Graphene Thin Films by Chemical Reduction of Exfoliated and Intercalated Graphite Oxide, Journal of Chemistry, 2013 (2013) Article ID 150536.

[31] H. Zhang, S. Virally, Q. Bao, L. Kian Ping, S. Massar, N. Godbout, P. Kockaert, Z-scan measurement of the nonlinear refractive index of graphene, Optics Letters, 37 (2012) 1856-1858.

[32] M. Sheik-bahae, A.A. Said, E.W. Van Stryland, High-sensitivity, single-beam n_2 measurements, Optics Letters, 14 (1989) 955-957.

[33] G.V. Prakash, M. Cazzanelli, Z. Gaburro, L. Pavesi, F. Iacona, G. Franzò, F. Priolo, Nonlinear optical properties of silicon nanocrystals grown by plasma-enhanced chemical vapor deposition, Journal of Applied Physics, 91 (2002) 4607-4610.

[34] A. Srivastava, C. Galande, L. Ci, L. Song, C. Rai, D. Jariwala, K.F. Kelly, P.M. Ajayan, Novel Liquid Precursor-Based Facile Synthesis of Large-Area Continuous, Single, and Few-Layer Graphene Films, Chemistry of Materials, 22 (2010) 3457-3461.

[35] L.G. Cançado, K. Takai, T. Enoki, M. Endo, Y.A. Kim, H. Mizusaki, A. Jorio, L.N. Coelho, R. Magalhães-Paniago, M.A. Pimenta, General equation for the determination of the crystallite size La of nanographite by Raman spectroscopy, Applied Physics Letters, 88 (2006) 163106.

[36] K. Sato, R. Saito, Y. Oyama, J. Jiang, L.G. Cançado, M.A. Pimenta, A. Jorio, G.G. Samsonidze, G. Dresselhaus, M.S. Dresselhaus, D-band Raman intensity of graphitic materials as a function of laser energy and crystallite size, Chemical Physics Letters, 427 (2006) 117-121.

[37] M.J. Matthews, M.A. Pimenta, G. Dresselhaus, M.S. Dresselhaus, M. Endo, Origin of dispersive effects of the Raman D band in carbon materials, Physical Review B, 59 (1999) R6585.

[38] H. Wang, J. You, L. Wang, M. Feng, Y. Wang, Theory of the evolution of 2D band in the Raman spectra of monolayer and bilayer graphene with laser excitation energy, Journal of Raman Spectroscopy, 41 (2010) 125-129.

[39] N.R. Raravikar, P. Keblinski, A.M. Rao, M.S. Dresselhaus, L.S. Schadler, P.M. Ajayan, Temperature dependence of radial breathing mode Raman frequency of single-walled carbon nanotubes, Physical Review B, 66 (2002) 235424.

[40] I. Calizo, A.A. Balandin, W. Bao, F. Miao, C.N. Lau, Temperature Dependence of the Raman Spectra of Graphene and Graphene Multilayers, Nano Letters, 7 (2007) 2645-2649.

[41] I. Calizo, S. Ghosh, W. Bao, F. Miao, C. Ning Lau, A.A. Balandin, Raman nanometrology of graphene: Temperature and substrate effects, Solid State Communications, 149 (2009) 1132-1135.

[42] M.J. Allen, J.D. Fowler, V.C. Tung, Y. Yang, B.H. Weiller, R.B. Kaner, Temperature dependent Raman spectroscopy of chemically derived graphene, Applied Physics Letters, 93 (2008) 193119.

Chapter 6

Graphene Oxide and Thermally Reduced Graphene Oxide Thin Films

In this chapter, structural, optical and electrical properties of as prepared graphene oxide (GO) by chemical routes and thermally reduced GO thin films at different temperatures are studied in details. Thin films of GO were prepared on quartz and undoped Si substrates by drop casting method. Structural properties of GO and thermally reduced GO thin films are studied by Raman scattering, field emission scanning electron microscopy (FESEM), atomic force microscopy (AFM), Fourier transform infrared spectroscopy (FTIR), X-ray photoelectron spectroscopy (XPS) and transmission electron microscopy (TEM). Optical and electrical properties of the films are studied by UV-Vis-NIR spectroscopy and I-V measurement with two probes respectively. The motivation behind this chapter is to study the properties of GO / reduced GO thin films with different fraction of oxygen containing functional groups bonded with carbon atoms.

6.1 Experimental details

6.1.1 Preparation of GO and thermally reduced GO thin films

Graphene oxide was prepared by modified Hummers method [1-5] using graphite powder as a source material. Graphite powder of grain size less than 75 μm (-200 mesh) with 99.999% purity (stock no. 40799) was purchased from Alfa Aesar. Preparation details of GO thin films are described below in details. Graphite powder (1g) was stirred in 98% H_2SO_4 (18 ml) for 3h. $KMnO_4$ (3g) was then gradually added into the solution while stirring in ice tub. The mixture was kept on stirrer for 1h at 40 – 50 °C and solution turned reddish in color. The resulting solution was then diluted by adding 25 ml of de-ionized water and mixture was heated at 90 °C for 30 min. Solution was then diluted by adding 75 ml of de-ionized water and finally 30% H_2O_2 solution (5 ml) was added to it. The resulting solution was greenish yellow in color. The mixture was washed with 5% HCl followed by de-ionized water until the pH of the solution became neutral. The solution was subsequently centrifuged twice at 4000 rpm for 30 min and resulting GO solution was obtained in brownish color. The solution was further filtered and dried in vacuum. For making thin films of graphene oxide, GO powder was subsequently dissolved in de-ionized water such that resulting concentration was 0.1 mg/ml. GO thin films (~ 70 nm, thick) were deposited on 1cm x 1cm quartz and undoped Si substrates by drop casting using 20 μl of the solution. Thickness of the films could be controlled using the optimized concentration of the solution. Due to its hydrophilic nature [6-8], GO easily disperses in water and therefore spreads over the substrate resulting in uniform thin films. Thickness of the films was measured using stylus profilometer.

The removal of oxygen containing functional groups from graphene oxide thin films was performed by thermal reduction at four different temperatures 130, 200, 300 and 400 °C for 1h under high vacuum ($\sim 10^{-6}$ mbar).

6.2 Structural properties of GO and thermally reduced GO thin films

6.2.i FESEM

Figure 6.1 shows the FESEM image of thermally reduced GO thin films on undoped Si substrate at two different reduction temperatures of 130 and 400 °C. As we can see from the FESEM image, films are uniformly spread over entire area of the substrates with lots of wrinkles and no observed discontinuity in the films. Thermally reduced GO thin films have smooth surface for the films annealed at 130 °C, however, formation of pores of size in the range of ~ 500 - 700 nm are observed for the films annealed at 400 °C. The reason of these structural changes at high reduction temperature of 400 °C could be due to removal of weak oxygen containing functional groups bonded with carbon atoms [4, 9, 10].

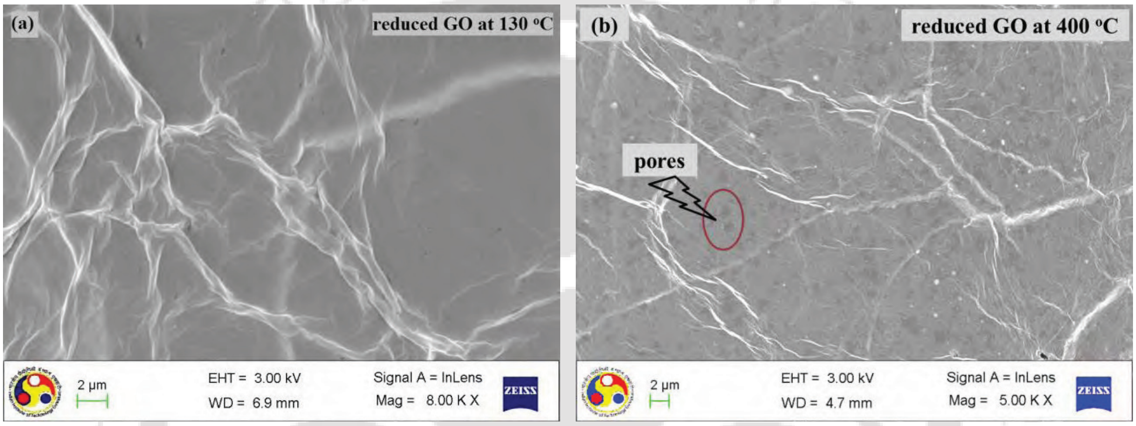

***Figure 6.1:** FESEM image of thermally reduced GO thin films on undoped Si substrate at two different reduction temperatures of (a) 130 °C and (b) 400 °C.*

6.2.ii Raman scattering

Figure 6.2 shows the Raman spectra of as prepared GO and thermally reduced GO thin films on quartz substrate with excitation wavelength of 514.53 and 632.8 nm. Raman spectrum of graphite powder is also shown here for comparison with the as prepared and thermally reduced GO films. Defects free graphite powder shows the characteristic peaks at 1583 cm^{-1} (G band) and 2730 cm^{-1} (2D band) with a small shoulder at lower wavenumber side 2690 cm^{-1} with excitation wavelength of 514.53 nm. The as prepared and thermally reduced GO films show the prominent characteristic peaks at 1350 and 1596 cm^{-1} corresponding to D and G bands respectively. In addition, some more characteristic peaks with small intensity, in as prepared and thermally reduced GO films, are also observed at 2690 cm^{-1} (2D band), 2930 cm^{-1} (D+G band) and 3206 cm^{-1} (G+D' band) with excitation wavelength of 514.53 nm. Raman spectra of GO and reduced GO thin films with excitation wavelength of 632.8 nm show similar characteristic peaks corresponding to different bands such as D band, G band, etc. as in the case of 514.53 nm. However, peak position of D and 2D bands are shifted towards lower wavenumber side 1331 cm^{-1} and 2673 cm^{-1} respectively with excitation wavelength of 632.8 nm. The increase in FWHM of G band and presence of D band in all the films, i.e. as prepared and reduced GO films, in comparison to graphite powder ensures that defects are produced in the carbon basal planes and on the edges due to functionalization of graphite powder by several functional groups. Even after removal of functional groups to a large extent, reduced GO films still contain a significant amount of residual defects which is caused by the creation of permanent defects in the carbon basal planes during functionalization [2, 9, 11, 12].

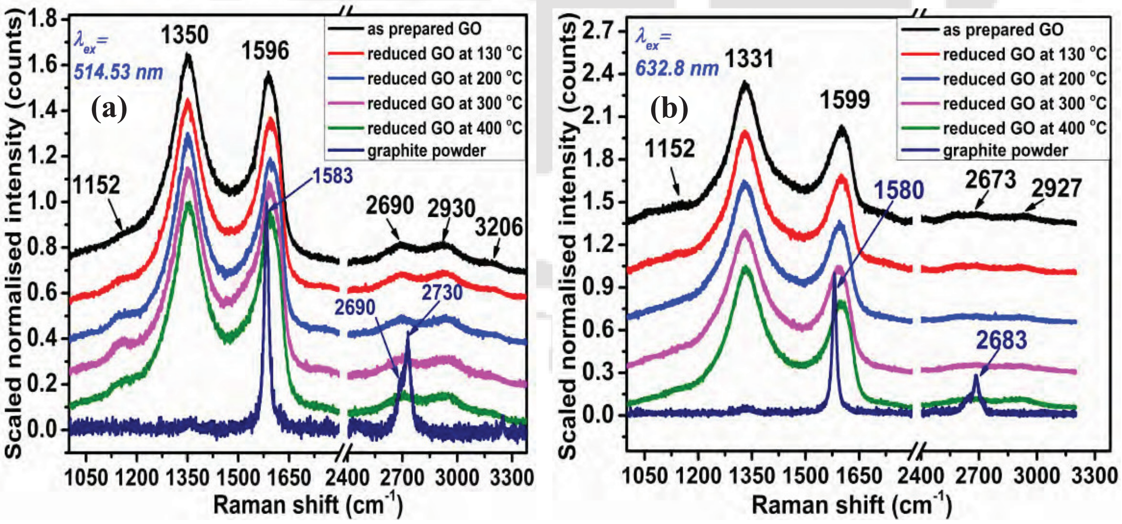

Figure 6.2: *Raman spectra of as prepared GO and thermally reduced GO thin films on quartz substrate at different excitation wavelength of (a) 514.53 nm and (b) 632.8 nm.*

Table 6.1: FWHM, peak intensity ratio of D and G band (I_D/I_G) and average grain size (L_a) of sp^2 bonded carbon at two different excitation wavelength of 514.53 and 632.8 nm.

Samples	**514.53 nm (2.40 eV)**				**632.8 nm (1.95 eV)**			
	FWHM (D band) (cm^{-1})	FWHM (G band) (cm^{-1})	I_D/I_G (using intensity)	Grain size, L_a (nm)	FWHM (D band) (cm^{-1})	FWHM (G band) (cm^{-1})	I_D/I_G (using intensity)	Grain size, L_a (nm)
Graphite powder	---	16	0	inf.	---	13	0	inf.
GO	132	73	1.11	15.15	118	75	1.49	25.82
reduced GO at 130 °C	130	79	1.08	15.57	122	73	1.50	25.65
reduced GO at 200 °C	119	79	1.13	14.88	141	72	1.42	27.09
reduced GO at 300 °C	131	80	1.07	15.71	153	74	1.35	28.50
reduced GO at 400 °C	133	75	1.04	16.17	136	73	1.33	28.93

The FWHM of D and G bands and peak intensity ratio I_D/I_G with different excitation wavelength are shown in table 6.1. The main difference in the Raman spectra of GO / reduced GO thin films at different excitation wavelength of 514.53 and 632.8 nm is the difference in peak intensity ratio I_D/I_G. The peak intensity ratio I_D/I_G is increased with increasing laser excitation wavelength (or decreasing energy of laser), which is also in agreement with the results reported in literature [11, 13]. Raman spectra of the GO and reduced GO films show that with increasing reduction temperature, peak intensity ratio I_D/I_G is gradually decreased for both the excitation wavelength of 514.53 and 632.8 nm. These results show that with increasing reduction temperature, the amount of oxygen containing functional groups bonded with carbon atoms is decreased and at the same time reformation of grains with neighboring sp^2 bonded carbon atoms is increased. As a result, grain size of sp^2 bonded carbon atoms is slightly increased with increase in reduction temperature. The grain size of sp^2 bonded carbon atoms has been calculated using Tuinstra-Koenig expression [14], which is related to the peak intensity ratio of D and G band (I_D/I_G) [13, 15]. The average sp^2 grain size is observed in the range of 15 – 17 nm and 25 – 29 nm for excitation wavelength of 514.53 nm and 632.8 nm respectively for as prepared and thermally reduced GO thin films, which is consistent with the other results reported in literature [3, 16].

6.2.iii AFM

Figure 6.3 shows AFM image of as prepared GO thin films on quartz substrate. As can be seen from the enlarged view of AFM image, films are uniformly spread over the substrates with the roughness of approximately 3.4 nm.

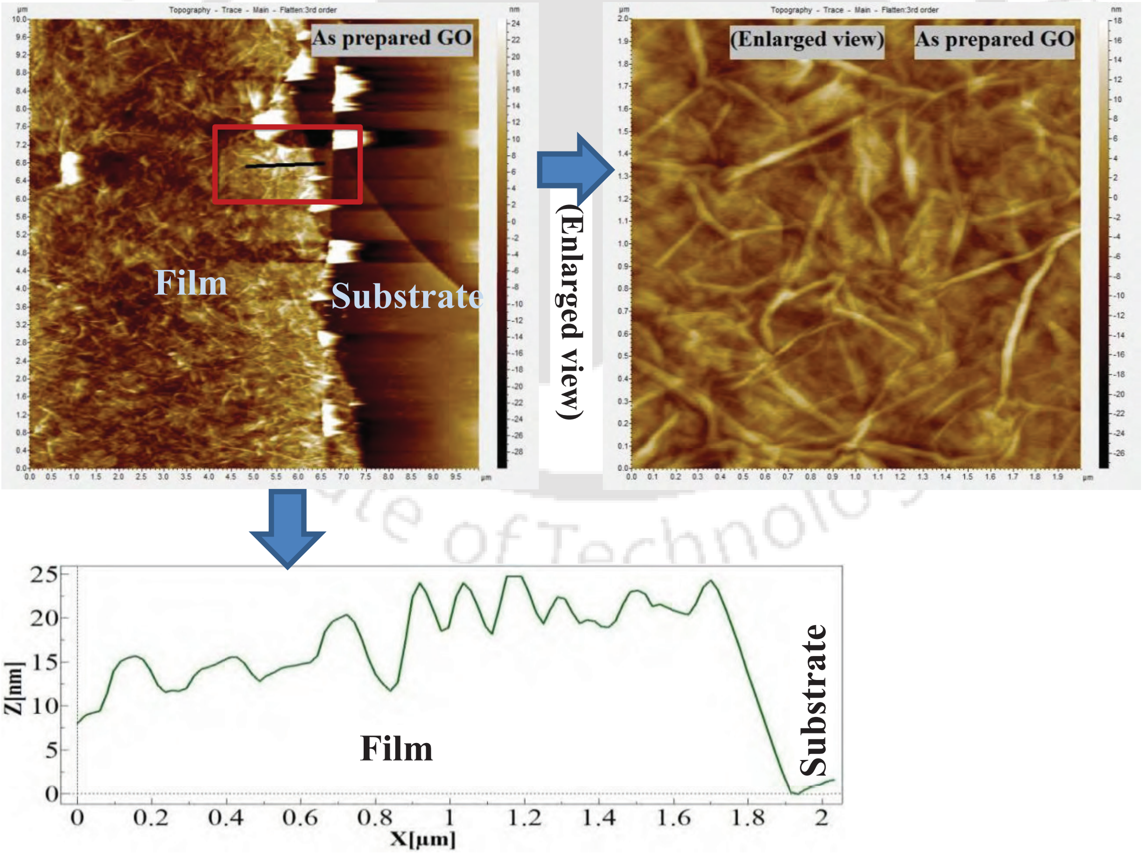

Figure 6.3: *AFM image and surface height profile of as prepared GO thin films on quartz substrate.*

For measuring the thickness of the film, AFM image is taken at the edges of the film after scratching the sample surface. The thickness of the films is measured using surface height profile of AFM image and it is ~ 20 – 25 nm, which is slightly lower in comparision to thickness (~ 70 nm) measured using stylus profilometer. This slight variation in thickness of the films could be due to scan length which is different in two cases, scan length in AFM is in µm whereas films are scanned in mm dimension using stylus profilometer.

6.2.iv FTIR

Figure 6.4 shows the FTIR transmission spectra of as prepared GO and thermally reduced GO thin films on undoped Si substrate at four different reduction temperatures of 130, 200, 300 and 400 °C. FTIR spectra of as prepared GO films show the absorption peak centered at 1580 cm^{-1} corresponding to sp^2 bonded C-C/C=C stretching vibrations in aromatic rings. In addition, absorption peaks corresponding to several oxygen containing functional groups are also present. Absorption peaks at 1100 cm^{-1} and 1216 cm^{-1} respectively, correspond to symmetric and asymmetric stretching vibration of C-O and absorption peak at 1727 cm^{-1} corresponds to stretching vibration of C=O bonds. The presence of these carbon atoms bonded with oxygen suggests that graphite powder is functionalized with several oxygen containing functional groups such as carboxyl, carbonyl, etc. FTIR spectra of GO also show a broad absorption peak centered at 3290 cm^{-1} and 1437 cm^{-1} corresponding to O-H stretching vibration of hydroxyl group. In the case of reduced GO film at 130 °C, the absorption peak corresponding to –OH is greatly reduced, however, all other functional groups are still present which suggests that not much compositional changes occurred in the film reduced at 130 °C. The absorption peaks of oxygen containing functional groups are found to reduce with further increase in reduction temperature. For the films annealed at 400 °C, the peaks at 1100 cm^{-1} and 1216 cm^{-1} merge together and resulting peak is shifted towards 1216 cm^{-1}. This is due to removal of some oxygen bonded atoms from GO. A shift towards 1216 cm^{-1} is also an indication of dominance of asymmetric C-O stretching bonds over symmetric stretching bonds. The presence of peaks at 1216 cm^{-1} and 1727 cm^{-1} suggests a partial restoration of some carboxyl functional group in carbon basal plane even after reduction at 400 °C [3, 9, 12, 16, 17].

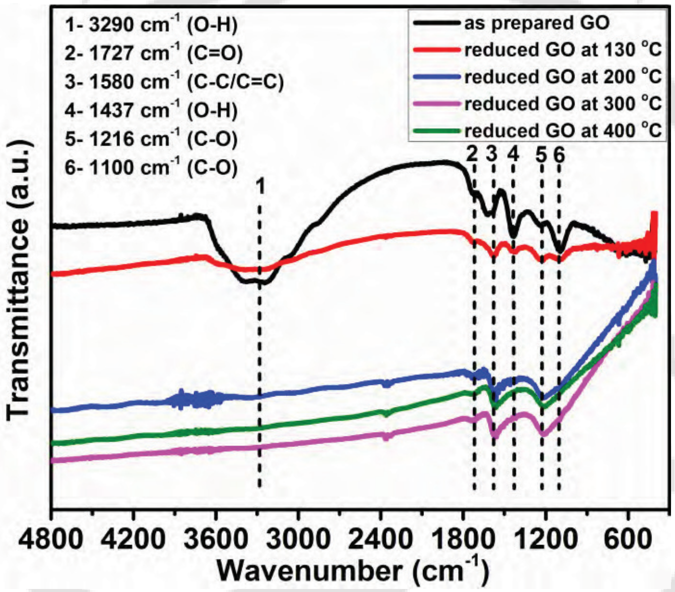

Figure 6.4: *FTIR transmission spectra of as prepared GO and thermally reduced GO at different temperatures of 130, 200, 300 and 400 °C.*

6.2.v XPS

Figure 6.5 shows the XPS survey spectra of as prepared GO and thermally reduced GO thin films on quartz substrate at different reduction temperatures of 200, 300 and 400 °C. Spectra were taken after Ar+ ion sputtering for 5 min. XPS spectra show three different characteristic peaks at approximately 284, 400 and 530 eV corresponding to C1s, N1s and O1s respectively [16]. For detail study of the core level XPS spectra of C1s, all the measured spectra are deconvoluted using Gaussian peak fit into four different characteristic peaks corresponding to different bonding energy of the atoms in the molecules. Figure 6.6 shows the deconvoluted C1s XPS spectra of as prepared GO and thermally reduced GO at different reduction temperatures of 200, 300 and 400 ^{o}C. Deconvoluted spectra show four different characteristic peaks at approximately 284.1, 285.6, 287.2 and 288.8 eV corresponding to C-C, C-O (hydroxyl), C=O (carbonyl) and O=C-O (carboxyl) groups respectively [2, 16, 18]. The C-C peak refers to the sp^2 bonded carbon atoms, while oxygen containing functional groups refers to the sp^3 hybridized carbon components [17, 19, 20]. The relative fractions of sp^2 bonded carbon atoms and sp^3 bonded oxygen containing functional groups in all the samples (as prepared GO and thermally reduced GO at different reduction temperature) are calculated using integrated area of the corresponding peaks in the deconvoluted C1s XPS spectra and values are listed in table 6.2. The sp^2 and sp^3 fractions of each functional groups are calculated using integrated area of individual group divided by total integrated area of all the functional groups (C-C, C-O, C=O and O=C-O). A decrease in relative fraction of all the oxygen containing functional groups is observed with increase in reduction temperature. In as prepared GO films, a very low fraction (~ 3%) of carbon atoms is bonded in sp^2 mode and fraction of sp^2 bonded carbon is increased to ~ 65% for reduced GO films at 400 ^{o}C. As we can see (from table 6.2) the fraction of sp^2 and sp^3 bonded carbon with different reduction temperature, the fraction of sp^3 modes in carbonyl group (C=O bond) is slightly increased for the films reduced at 400 ^{o}C in comparison to 300 ^{o}C. This could be due to structural changes in one form of oxygen containing functional groups to other at high temperature. An increase in fraction of sp^2 bonded carbon atoms confirms the formation of graphitic carbon/graphene after thermal reduction.

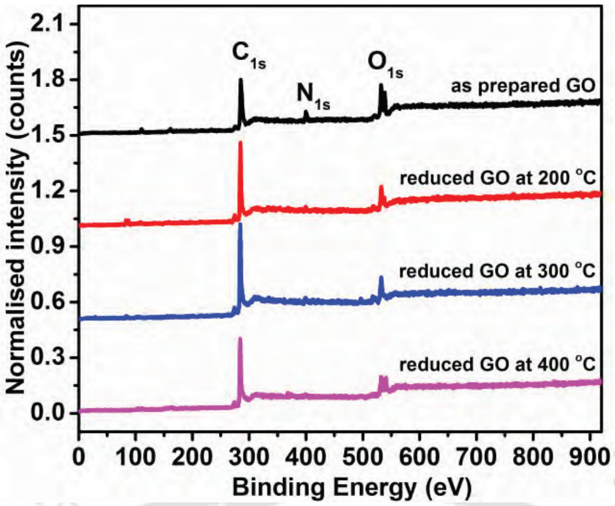

Figure 6.5: *XPS survey spectra of as prepared and thermally reduced GO at different reduction temperatures of 200, 300 and 400 °C.*

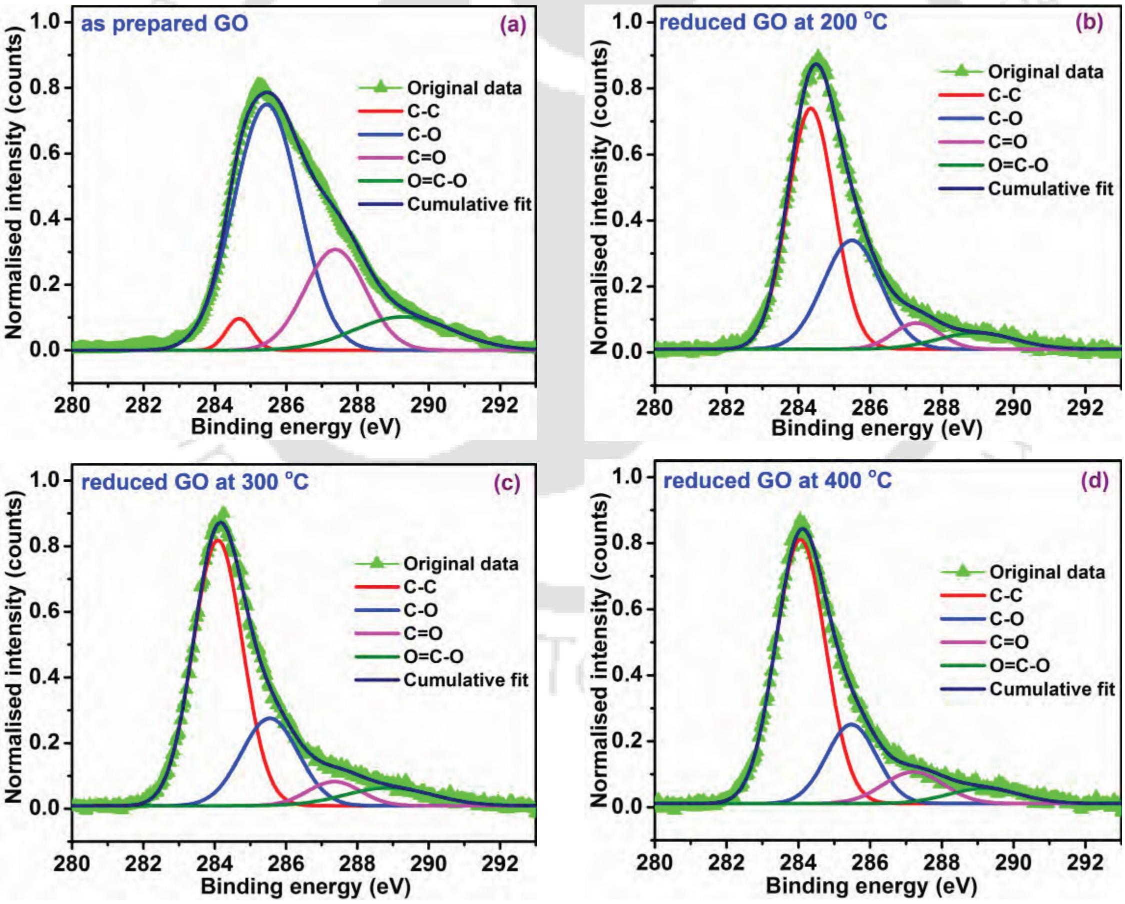

Figure 6.6: *Deconvoluted detail core C1s XPS spectra of (a) as prepared GO and thermally reduced GO thin films at different reduction temperatures of (b) 200 °C, (c) 300 °C and (d) 400 °C.*

Table 6.2: Relative fraction of sp^2 and sp^3 bonded carbon for GO and thermally reduced GO films corresponding to different functional groups.

Samples	Relative fraction of sp^2 and sp^3 (in %)			
	C-C (sp^2)	**C-O (sp^3)**	**C=O (sp^3)**	**O=C-O (sp^3)**
as prepared GO	3.19	61.34	23.04	12.41
reduced GO at 200 °C	56.66	31.42	5.71	6.19
reduced GO at 300 °C	63.22	23.76	5.82	7.17
reduced GO at 400 °C	65.56	19.81	9.43	5.18

6.2.vi TEM

Figure 6.7 shows the TEM image and selected area electron diffraction (SAED) pattern of reduced GO thin films, which is reduced at 400 °C on TEM grid (Cu mesh). TEM image shows the black spots at several locations of the film. These black spots indicate the porosity in the films, which is produced during the reduction of GO thin films at high temperature. These results are also in agreement with the FESEM image (section 6.2.i), where porosity is observed for the films reduced at 400 °C. SAED pattern shows the amorphous nature of the films, whereas, at some locations we have also observed the crystalline nature of the films. The amorphous nature of the films could be due to insertion of oxygen atom bonded with carbon atoms and further reduction of oxygen at high temperature. From SAED pattern, interlayer $d_{spacing}$ is calculated using Digital Gatan software and compared with the JCPDS (Joint Committee on Powder Diffraction Standards) data. The center ring with an interlayer spacing of 3.21 Å corresponds to (002) plane of graphite. As we move from the center ring, inperplanar spacing are 2.37, 1.87 and 1.66 Å corresponding to (100), (102) and (004) plane of graphitic carbon respectively, which is consistent with the results reported in literature [3, 21, 22].

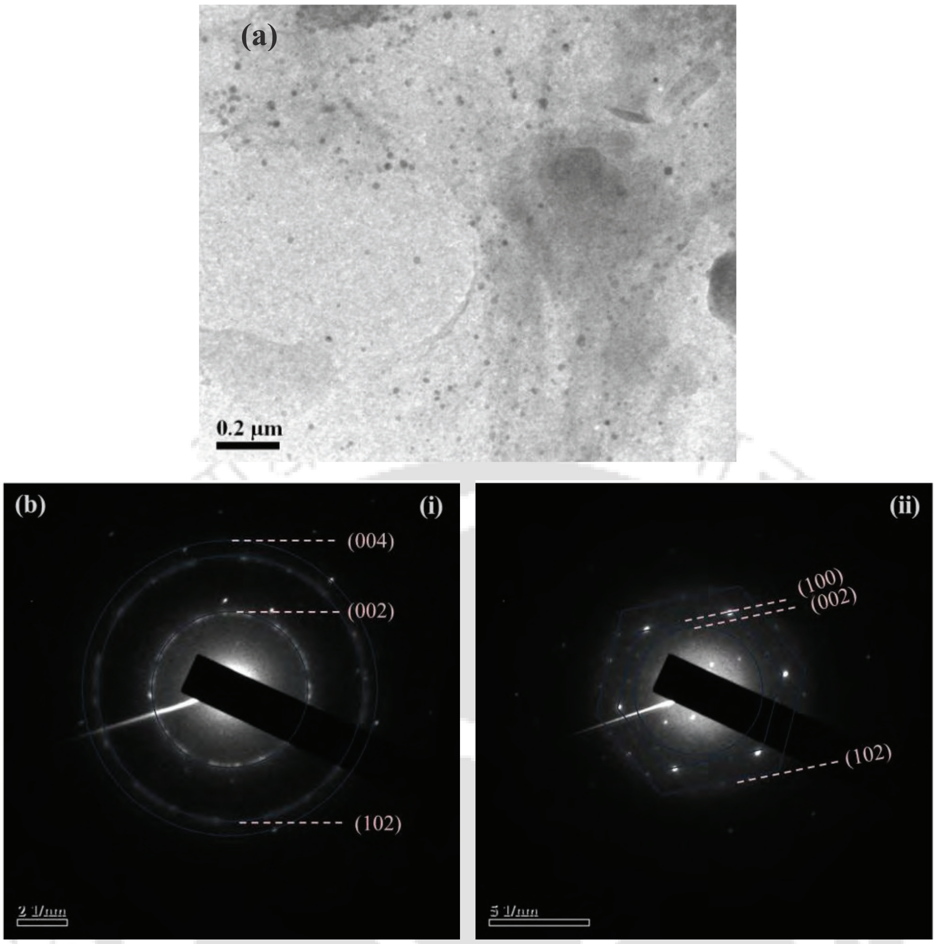

Figure 6.7: *(a) TEM image and (b) SAED pattern ((i) corresponds to amorphous, (ii) corresponds to crystalline nature) of reduced GO thin films at reduction temperature of 400 °C.*

6.3 Optical properties of GO and thermally reduced GO thin films

6.3.1 UV-Vis-NIR absorbance

Figure 6.8 shows the UV-Vis-NIR absorption spectra of as prepared GO and thermally reduced GO thin films on quartz substrate at different reduction temperature of 130, 200, 300 and 400 °C. Absorption spectra were recorded using blank quartz substrate as a reference. The absorption spectra of as prepared GO shows maximum absorption at 230 nm corresponding to $\pi \rightarrow \pi^*$ transitions of aromatic sp^2 bonded C-C/C=C bonds and a small shoulder at approximately 300 nm corresponding to $n \rightarrow \pi^*$ transitions of carbonyl groups (C=O bonds) [6]. A shift in position of 230 nm peak towards higher wavelength is observed for thermally reduced GO thin films; the shift increases with increasing reduction temperature. Further, for the films reduced at 400 °C, absorption peak is observed at 262 nm. The absorption peak at 300 nm is almost absent in reduced GO thin films for the reduction temperature of T > 200 °C, suggesting the removal of C=O bonds. The reason of shift in absorption peak towards higher wavelength as well as increase in broadening with increasing reduction temperature are due to the removal of oxygen containing functional groups at higher reduction temperature of T > 200 °C, which results in the more $\pi \rightarrow \pi^*$ transition in sp^2 bonded carbon atoms at lower energy in comparison to sp^3 bonded carbon atoms with oxygen [6].

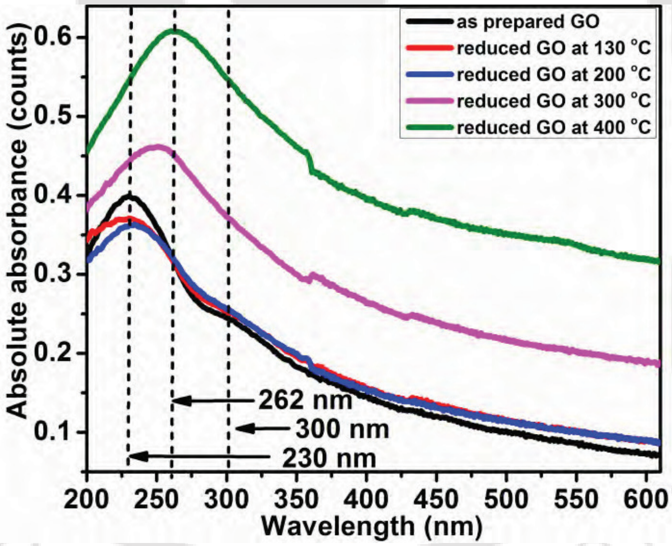

Figure 6.8: *UV-Vis-NIR absorption spectra of as prepared GO and thermally reduced GO at different reduction temperatures of 130, 200, 300 and 400 °C.*

6.4 Electrical properties of GO and thermally reduced GO thin films

6.4.1 Temperature dependent electrical conductivity (σ – T) (300 – 520K)

Figure 6.9 shows the electrical conductivity (σ) of as prepared GO and thermally reduced GO thin films (at reduction temperature of 130, 200 and 400 °C) as a function of temperature in the range of 300 – 520 K. For as prepared GO films, σ (300 K) is very low ~6.8 x 10^{-6} S/cm and remains low till the temperature is raised to 370 K. Beyond 370 K, a sharp increase in conductivity is observed up to 440 K. With further increase in temperature, conductivity is thermally activated with activation energy of about 0.26 eV. Activation energy of thermally activated carriers is measured from the Arrhenius plot, as given in equation 6.1.

$$\sigma = \sigma_0 \exp\left(\frac{-E_a}{K_B T}\right) \ldots\ldots\ldots\ldots\ldots\ldots\ldots\ldots\ldots\ldots\ldots (6.1)$$

where, σ_0 is the pre-factor, E_a is activation energy, K_B is Boltzmann's constant and T is absolute temperature in kelvin.

A similar variation in σ with temperature is observed in the case of thermally reduced GO at 130 and 200 ^{o}C, with a slight increase in magnitude of σ (300 K); higher σ (300 K) value for the films reduced at higher temperature. The magnitude of σ (520 K) for these three films, as deposited GO and thermally reduced GO at 130 and 200 ^{o}C, are nearly same in the range of 50 – 60 S/cm suggesting the similar electronic structure of these films at 520 K. A drastic increase in σ (300 K) by almost seven orders of magnitude is observed for films reduced at 400 ^{o}C, for which conductivity is thermally activated in the measured temperature range of 300 – 520 K with small activation energy 0.05 eV. This sharp increase in conductivity for GO films reduced at temperature $T \geq 200$ ^{o}C is associated with a significant decrease in C-O bond concentration along with the increase in concentration of C-C bond (table 6.2). Electrical conductivity σ (300 K) and σ (520 K) with activation energy for all the films are listed in table 6.3. A systematic increase in σ (300 K) value over seven orders of magnitude with different annealing temperatures is a clear indication of switching from insulator to semi-metallic behavior of GO films. Therefore, structural properties which correspond to change in electrical conductivity of GO films can easily be tuned for different device applications [7, 23-26].

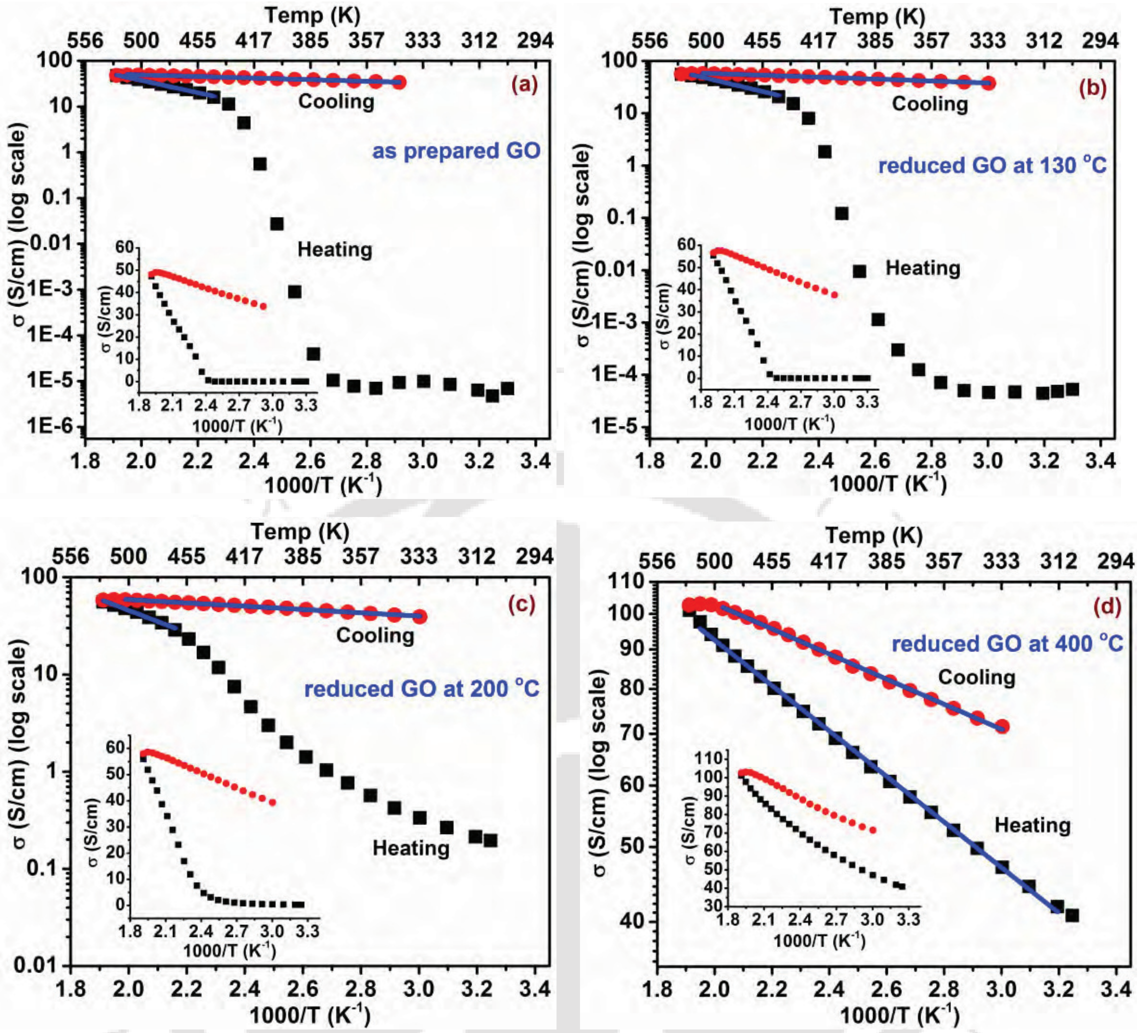

Figure 6.9: *Temperature dependent electrical conductivity of (a) as prepared GO and reduced GO at different reduction temperatures of (b) 130 °C, (c) 200 °C and (d) 400 °C.*

Table 6.3: Electrical conductivity (σ) at 300K and 520K and corresponding activation energy for GO and thermally reduced GO thin films

Samples	**Activation energy (eV) (440 – 520K) Heating cycle**	**Activation energy (eV) (520 - 330K) cooling cycle**	**σ (300K) (S/cm)**	**σ (520K) (S/cm)**
as prepared GO	0.26	0.034	6.8×10^{-6}	48
reduced GO at 130 °C	0.25	0.036	5.2×10^{-5}	56
reduced GO at 200 °C	0.22	0.033	1.9×10^{-1}	57
reduced GO at 400 °C	0.05	0.032	40	102

6.5 Conclusion

Graphene oxide was synthesized using chemically derived modified Hummer's method. We have studied the structural, optical and electrical properties of GO thin films. To study the structural, optical and electrical properties of the films with different fraction of oxygen containing functional groups, as prepared GO thin films were thermally reduced at different reduction temperature of 130, 200, 300 and 400 °C. From the study of different properties of as prepared and reduced GO thin films, we have observed the structural changes in the films within the temperature range of 130 – 200 °C and no structural changes are observed below 130 °C, which is confirmed by UV-Vis-NIR absorption as well as FTIR transmission spectra. The corresponding changes in oxygen containing functional groups are further confirmed by XPS spectra. We have also studied the electrical properties of as prepared and reduced GO thin films. The as prepared GO films show the room temperature (at 300 K) electrical conductivity of the order of 10^{-6} S/cm and conductivity of the films increase with increasing reduction temperature. The room temperature electrical conductivity of reduced GO films at different reduction temperature of 130, 200 and 400 °C is 5.2×10^{-5}, 1.9×10^{-1} and 40 S/cm respectively. The conductivity of the films (GO / reduced GO) increase with increasing in temperature from 300 K to 520 K. The conductivity of the films at 520 K are 48, 56, 57 and 102 S/cm respectively for as prepared GO and reduced GO thin films at 130, 200 and 400 °C. These results suggest that with increase in reduction temperature, the fractions of oxygen containing functional groups are decreased and corresponding electrical conductivity is increased. Thus, the fraction of sp^2 and sp^3 bonded carbon in reduced graphene oxide can be easily tuned specially for the development of sensing devices.

6.6 References

[1] L. Qiu, H. Zhang, W. Wang, Y. Chen, R. Wang, Effects of hydrazine hydrate treatment on the performance of reduced graphene oxide film as counter electrode in dye-sensitized solar cells, Applied Surface Science, 319 (2014) 339-343.

[2] D. Yang, A. Velamakanni, G. Bozoklu, S. Park, M. Stoller, R.D. Piner, S. Stankovich, I. Jung, D.A. Field, C.A. Ventrice Jr, R.S. Ruoff, Chemical analysis of graphene oxide films after heat and chemical treatments by X-ray photoelectron and Micro-Raman spectroscopy, Carbon, 47 (2009) 145-152.

[3] K. Krishnamoorthy, M. Veerapandian, K. Yun, S.J. Kim, The chemical and structural analysis of graphene oxide with different degrees of oxidation, Carbon, 53 (2013) 38-49.

[4] Y. Zhu, W. Cai, R.D. Piner, A. Velamakanni, R.S. Ruoff, Transparent self-assembled films of reduced graphene oxide platelets, Applied Physics Letters, 95 (2009) 103104.

[5] K. Krishnamoorthy, R. Mohan, S.-J. Kim, Graphene oxide as a photocatalytic material, Applied Physics Letters, 98 (2011) 244101.

[6] D.C. Marcano, D.V. Kosynkin, J.M. Berlin, A. Sinitskii, Z. Sun, A. Slesarev, L.B. Alemany, W. Lu, J.M. Tour, Improved Synthesis of Graphene Oxide, ACS Nano, 4 (2010) 4806-4814.

[7] G. Venugopal, K. Krishnamoorthy, S.-J. Kim, An investigation on high-temperature electrical transport properties of graphene-oxide nano-thinfilms, Applied Surface Science, 280 (2013) 903-908.

[8] S. Some, Y. Xu, Y. Kim, Y. Yoon, H. Qin, A. Kulkarni, T. Kim, H. Lee, Highly Sensitive and Selective Gas Sensor Using Hydrophilic and Hydrophobic Graphenes, Scientific Reports, 3 (2013) 1868.

[9] B. Zhao, P. Liu, Y. Jiang, D. Pan, H. Tao, J. Song, T. Fang, W. Xu, Supercapacitor performances of thermally reduced graphene oxide, Journal of Power Sources, 198 (2012) 423-427.

[10] H. Huang, Y. Ying, X. Peng, Graphene oxide nanosheet: an emerging star material for novel separation membranes, Journal of Materials Chemistry A, 2 (2014) 13772-13782.

[11] A. Kaniyoor, S. Ramaprabhu, A Raman spectroscopic investigation of graphite oxide derived graphene, AIP Advances, 2 (2012) 032183.

[12] H. Feng, R. Cheng, X. Zhao, X. Duan, J. Li, A low-temperature method to produce highly reduced graphene oxide, Nature Communication, 4 (2013) 1539.

[13] M.S. Dresselhaus, A. Jorio, A.G. Souza Filho, R. Saito, Defect characterization in graphene and carbon nanotubes using Raman spectroscopy, Philosophical Transactions of the Royal Society of London A: Mathematical, Physical and Engineering Sciences, 368 (2010) 5355-5377.

[14] F. Tuinstra, J.L. Koenig, Raman Spectrum of Graphite, The Journal of Chemical Physics, 53 (1970) 1126-1130.

[15] R. Beams, L.G. Cançado, L. Novotny, Raman characterization of defects and dopants in graphene, Journal of Physics: Condensed Matter, 27 (2015) 083002.

[16] H. Nantao, Y. Zhi, W. Yanyan, Z. Liling, W. Ying, H. Xiaolu, W. Hao, W. Liangmin, Z. Yafei, Ultrafast and sensitive room temperature NH_3 gas sensors based on chemically reduced graphene oxide, Nanotechnology, 25 (2014) 025502.

[17] Y. Hu, K. Wang, Q. Zhang, F. Li, T. Wu, L. Niu, Decorated graphene sheets for label-free DNA impedance biosensing, Biomaterials, 33 (2012) 1097-1106.

[18] S. Prezioso, F. Perrozzi, L. Giancaterini, C. Cantalini, E. Treossi, V. Palermo, M. Nardone, S. Santucci, L. Ottaviano, Graphene Oxide as a Practical Solution to High Sensitivity Gas Sensing, The Journal of Physical Chemistry C, 117 (2013) 10683-10690.

[19] G. Venugopal, K. Krishnamoorthy, R. Mohan, S.-J. Kim, An investigation of the electrical transport properties of graphene-oxide thin films, Materials Chemistry and Physics, 132 (2012) 29-33.

[20] D.W. Lee, J.W. Seo, sp^2/sp^3 Carbon Ratio in Graphite Oxide with Different Preparation Times, The Journal of Physical Chemistry C, 115 (2011) 2705-2708.

[21] A. Kaniyoor, S. Ramaprabhu, Thermally exfoliated graphene based counter electrode for low cost dye sensitized solar cells, Journal of Applied Physics, 109 (2011) 124308.

[22] T. Cui, R. Lv, Z.-H. Huang, H. Zhu, Y. Jia, S. Chen, K. Wang, D. Wu, F. Kang, Low-temperature synthesis of multilayer graphene/amorphous carbon hybrid films and their potential application in solar cells, Nanoscale Research Letters, 7 (2012) 1-7.

[23] K.S. Vasu, B. Chakraborty, S. Sampath, A.K. Sood, Probing top-gated field effect transistor of reduced graphene oxide monolayer made by dielectrophoresis, Solid State Communications, 150 (2010) 1295-1298.

[24] H.-J. Shin, K.K. Kim, A. Benayad, S.-M. Yoon, H.K. Park, I.-S. Jung, M.H. Jin, H.-K. Jeong, J.M. Kim, J.-Y. Choi, Y.H. Lee, Efficient Reduction of Graphite Oxide by Sodium Borohydride and Its Effect on Electrical Conductance, Advanced Functional Materials, 19 (2009) 1987-1992.

[25] W. Gao, L.B. Alemany, L. Ci, P.M. Ajayan, New insights into the structure and reduction of graphite oxide, Nature Chemistry, 1 (2009) 403-408.

[26] M.J. Kim, Y. Jeong, S. Sohn, S.Y. Lee, Y.J. Kim, K. Lee, Y.H. Kahng, J.-H. Jang, Fast and low-temperature reduction of graphene oxide films using ammonia plasma, AIP Advances, 3 (2013) 012117.

Chapter 7

Graphene Channel Field Effect Transistor

In this chapter, we report the fabrication of graphene channel field effect transistor (GFET) on p-type heavily doped Si substrate and study of transport properties of charge carriers.

7.1 Experimental details

7.1.1 Fabrication of graphene channel field effect transistor (GFET)

Graphene channel field effect transistor was fabricated on SiO_2 coated (300 nm, thick) boron doped p-type Si substrate (resistivity, 0.0005 – 0.001 ohm cm). In this device, graphene films are used as a channel. Graphene films were deposited on Ni foil by hot filament chemical vapor deposition (HFCVD) method using optimized deposition parameters as obtained in chapter 5 (series III: H_2/N_2 dilution): $CH_4/H_2/N_2$ gas flow rate of 5/40/0 sccm, T_S of 700 ^oC and t_d of 10 min. Films were further annealed at 800 ^oC for 1h under high vacuum, immediately after deposition. As prepared graphene films on Ni foil were transferred on SiO_2 coated Si substrate for making the device. Procedure for the fabrication of GFET is described below. After transfer of graphene films on Si substrate, channel was made using mask having width of 60 μm. Al electrodes (~ 400 nm, thick) were deposited using thermal evaporation on the top of graphene film at room temperature for source (s) and drain (d) electrodes and on the back side of Si substrate for gate (g) electrode. The channel length (L) and channel width (W) of as prepared GFET were 60 and 76 µm respectively. The front view of as fabricated GFET and its schematic diagram are shown in figure 7.1. Gate electrode is on the back side of Si substrate.

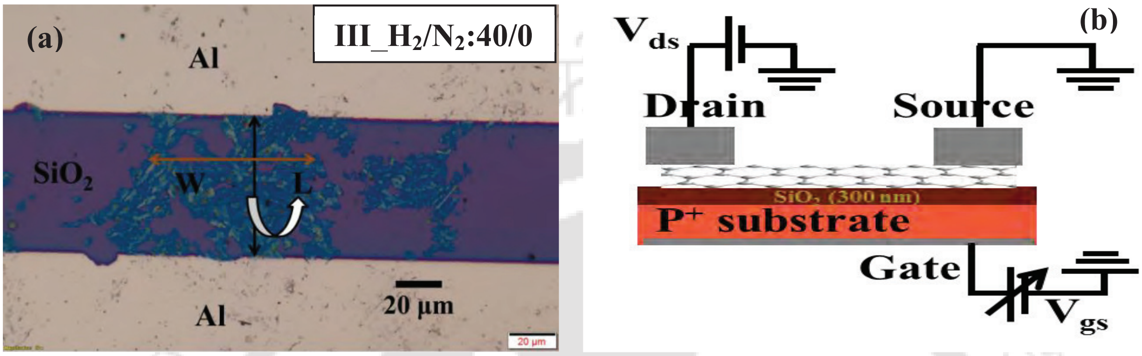

***Figure 7.1:** (a) As fabricated GFET on heavily doped p-type Si substrate and (b) its schematic diagram.*

7.2 Identification of number of graphene layers in channel

7.2.1 Raman scattering

Figure 7.2 shows the enlarged view of graphene channel and Raman spectra of graphene films at different locations in the channel. Raman spectra were recorded with an excitation wavelength of 514.53 nm. From Raman spectra, we can see that different characteristic features in terms of peak intensity ratio I_G/I_{2D} and FWHM of 2D band are observed at different locations in the films. Peak intensity ratio I_G/I_{2D} and FWHM for the Raman spectra of graphene films at different locations are in the range of 1.06 – 2.77 and 46 – 64 cm^{-1} respectively. This shows that graphene channel has different number of layers (tri-layers to multi-layers ($n \geq 15$)) in different region [1-3]. However, from the contrast of the films, it is expected that films have ~ 3 – 10 layers in approximately 50% area of the channel. The enlarge view of the channel shows that films are not continuous throughout the channel.

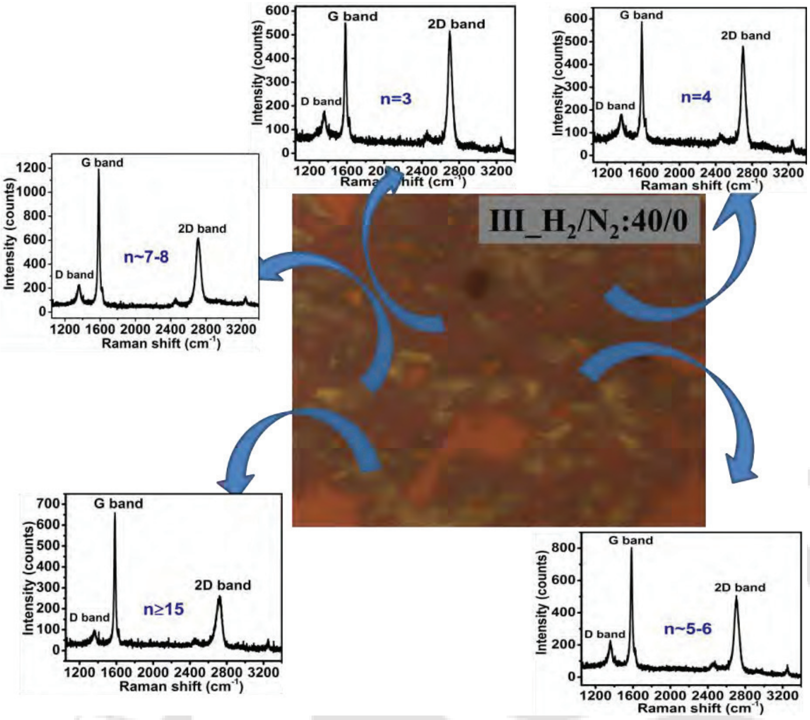

Figure 7.2: *Enlarged view of graphene channel and Raman spectra of graphene film at different locations in the channel.*

7.3 Transport properties of GFET

Figure 7.3 shows the variation in drain current (I_d) by varying gate to source voltage (V_{gs}) at fixed drain to source voltage (V_{ds}) of 100 mV. V_{gs} is varied from +30 to -30 V in step of 1V. It is observed that I_d is decreased from 8.46 μA to 7.80 μA with decreasing V_{gs} from +30 to -30 V. A decrease in drain current with decrease in gate voltage indicates that the current conduction is dominated by electrons in the channel. However, decay in drain current could also be possible due to defects in the films. Therefore for the confirmation of effect of gate voltage, measurements were performed with different gate voltage in on/off sequence, as shown in figure 7.4. These measurements show that drain current comes to the initial value of zero gate voltage after minimizing the gate voltage. This indicates that decay in drain current is not due to defects in the films, but is caused by gate voltage. The variation in drain current (I_d) with V_{ds} at different V_{gs} is shown in figure 7.5.

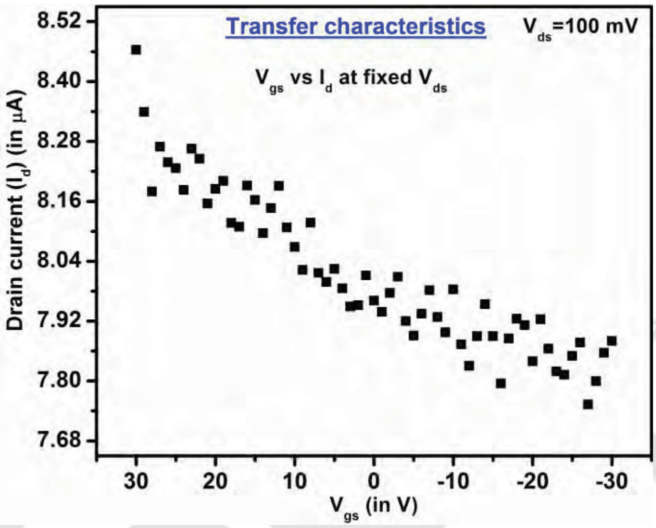

Figure 7.3: *Variation in drain current (I_d) with V_{gs} at fixed V_{ds} of 100 mV.*

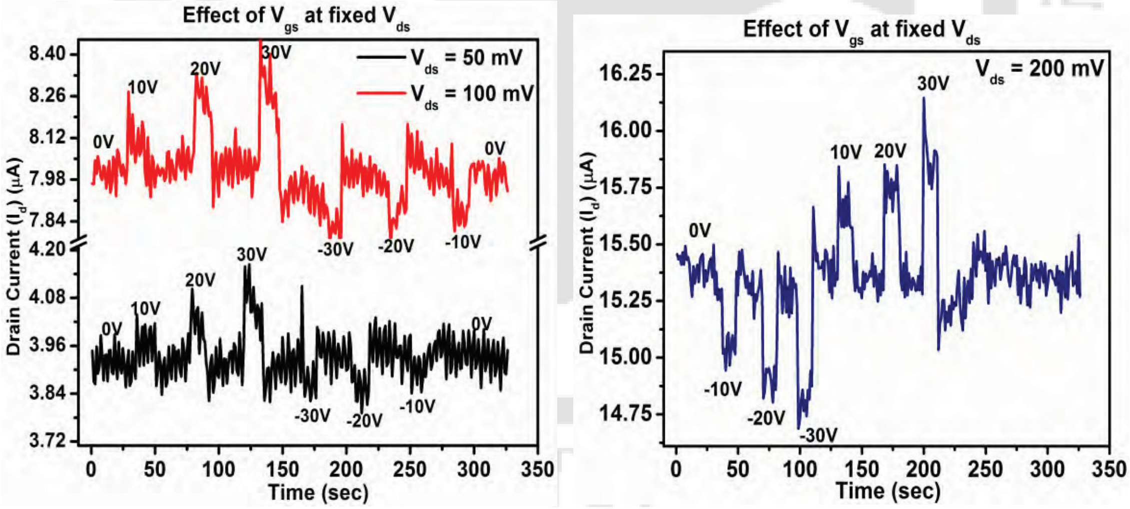

Figure 7.4: *Variation in drain current (I_d) with different V_{gs} (from 0 to 30 V and -30 to 0 V) in on/off sequence at fixed V_{ds} of 50, 100 and 200 mV.*

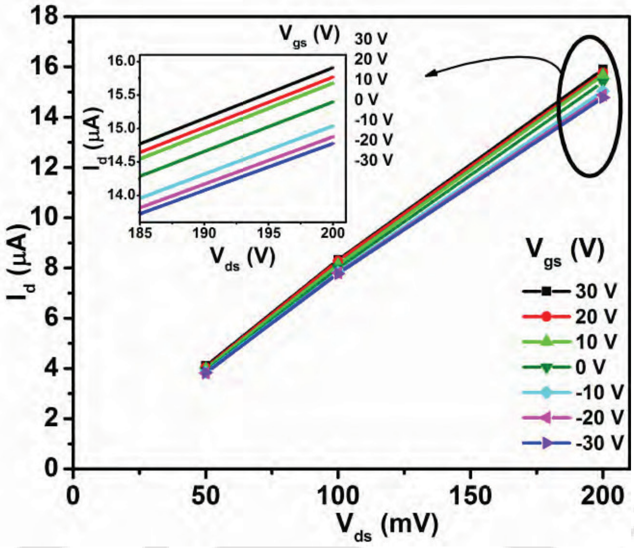

Figure 7.5: *Variation in drain current (I_d) with V_{ds} at different V_{gs} from -30 to 30V.*

From the transfer characteristic of GFET (figure 7.3), carrier mobility (µ) is calculated using equation (7.1) by measuring change in drain current (I_d) associated with the corresponding change in gate voltage (V_{gs}) [4].

$$\mu = \left(\frac{L}{W C_g V_{ds}} \right) \left(\frac{\Delta I_{ds}}{\Delta V_{gs}} \right) \text{...} (7.1)$$

Where, C_g (= $\varepsilon_o \varepsilon_r$ / d) is the gate capacitance per unit area (in F/cm^2), ΔI_{ds} is the change in drain current corresponding to change in gate to source voltage (ΔV_{gs}). ε_o is the permittivity of free space, ε_r is the relative static permittivity (i.e. dielectric constant) of the material (SiO_2 = 3.9) and d is the thickness of oxide layer. The gate capacitance per unit area (C_g) of oxide layer is 11.50 x 10^{-9} F/cm^2. The measured carrier mobility is ~ 10 cm^2/V-s. The measured carrier mobility is low in comparison to values reported in literature [4-10]. Wei et al. [4] have reported carrier mobility in the range of 300 – 1200 cm^2/V-s with the channel length of 2 µm and Reina et al. [5] have reported carrier mobility in the range of 100 – 2000 cm^2/V-s with the channel length of 5 – 15 µm for the graphene films prepared by CVD method. The carrier mobility of graphene is reported in the range of 10,000 – 15,000 cm^2/V-s for the mechanically exfoliated graphene films by noble laureate Novoselov et al. [11]. The observed low carrier mobility of our device could be due to the length of channel being much larger (60 μm) than reported in literature. An overestimate of channel width (due to discontinuity in the film) and the presence of multi-layers graphene films could also influence the calculated carrier mobility.

7.4 Conclusion

Graphene channel field effect transistor is fabricated on heavily doped P-type Si substrates. Transport characteristic of GFET shows the decrease in drain current with decrease in V_{gs}. This indicates that current conduction is dominated by electrons in the channel. However, the observed carrier mobility ~ 10 cm^2/V-s is low in comparison to other reports in literature.

7.5 References

[1] A. Gupta, G. Chen, P. Joshi, S. Tadigadapa, Eklund, Raman Scattering from High-Frequency Phonons in Supported n-Graphene Layer Films, Nano Letters, 6 (2006) 2667-2673.

[2] L.M. Malard, M.A. Pimenta, G. Dresselhaus, M.S. Dresselhaus, Raman spectroscopy in graphene, Physics Reports, 473 (2009) 51-87.

[3] A.C. Ferrari, J.C. Meyer, V. Scardaci, C. Casiraghi, M. Lazzeri, F. Mauri, S. Piscanec, D. Jiang, K.S. Novoselov, S. Roth, A.K. Geim, Raman Spectrum of Graphene and Graphene Layers, Physical Review Letters, 97 (2006) 187401.

[4] D. Wei, Y. Liu, Y. Wang, H. Zhang, L. Huang, G. Yu, Synthesis of N-Doped Graphene by Chemical Vapor Deposition and Its Electrical Properties, Nano Letters, 9 (2009) 1752-1758.

[5] A. Reina, X. Jia, J. Ho, D. Nezich, H. Son, V. Bulovic, M.S. Dresselhaus, J. Kong, Large Area, Few-Layer Graphene Films on Arbitrary Substrates by Chemical Vapor Deposition, Nano Letters, 9 (2009) 30-35.

[6] M.C. Lemme, T.J. Echtermeyer, M. Baus, H. Kurz, A Graphene Field-Effect Device, Electron Device Letters, IEEE Electron Device Letters, 28 (2007) 282-284.

[7] M.C. Lemme, T.J. Echtermeyer, M. Baus, B.N. Szafranek, J. Bolten, M. Schmidt, T. Wahlbrink, H. Kurz, Mobility in graphene double gate field effect transistors, Solid-State Electronics, 52 (2008) 514-518.

[8] H.-C. Kang, H. Karasawa, Y. Miyamoto, H. Handa, H. Fukidome, T. Suemitsu, M. Suemitsu, T. Otsuji, Epitaxial graphene top-gate FETs on silicon substrates, Solid-State Electronics, 54 (2010) 1071-1075.

[9] I. Meric, C.R. Dean, A.F. Young, N. Baklitskaya, N.J. Tremblay, C. Nuckolls, P. Kim, K.L. Shepard, Channel Length Scaling in Graphene Field-Effect Transistors Studied with Pulsed Current−Voltage Measurements, Nano Letters, 11 (2011) 1093-1097.

[10] N. Daniel, R. Alfonso, K. Jing, Electrical characterization of graphene synthesized by chemical vapor deposition using Ni substrate, Nanotechnology, 23 (2012) 015701.

[11] K.S. Novoselov, A.K. Geim, S.V. Morozov, D. Jiang, Y. Zhang, S.V. Dubonos, I.V. Grigorieva, A.A. Firsov, Electric fied effect in atomically thin carbon films, Science, 306 (2004) 666-669.

Chapter 8

Conclusion and Future Scopes

This chapter summarizes the work reported in present thesis on the growth and properties of different nanomaterials of carbon allotropes such as diamond like carbon (DLC), carbon nanoflakes (CNF), graphene and reduced graphene oxide (rGO) thin films. In this thesis work, we have studied the influence of different deposition parameters such as process pressure (PP), substrate temperature (T_S), CH_4/H_2 precursor gases flow rates, deposition time (t_d) and filament to substrate distance on the growth of different allotropes of carbon using hot filament chemical vapor deposition (HFCVD) method. We have also achieved a few results, which are not reported in literature prior to this work. The overall conclusion of thesis work and future research scopes are given in the following sections.

8.1 Thesis conclusion

- High density of sp^3 bonded DLC thin films are deposited on non-carbon affinity p-type Si / ITO coated glass substrates without any surface pretreatment by HFCVD method at distance 1 cm between filament and substrate. The density of diamond like particles on ITO coated glass substrate is in the range of 10^{10} – $10^{11}/cm^2$, which is higher in comparison to 10^8 – $10^9/cm^2$ for the films on Si substrate.

- High fraction of sp^3 bonded carbon atoms in DLC films, as measured from Raman spectra with an excitation wavelength of 488 nm, is observed on both the Si and ITO coated glass substrates at optimized methane concentration of 25 – 40% and beyond this range formation of graphitic phase is increased.
- Carbon nanoflakes are also successfully deposited on p-type Si and corning 1737 glass substrates by HFCVD method at distance of 1.5 cm between filament and substrate. The lateral size of as deposited flakes is in nm and size of the flakes is increased with increasing PP, whereas height of the flakes is increased with increase in substrate temperature.
- CNF as grown on Si substrate are aligned more in vertical direction as compared to flakes on corning glass substrate. This indicates that Si substrate is more suitable for the growth of flake type structures.
- CNF show high electrical conductivity in the range of 20 – 30 S/cm at room temperature and conductivity of the films is found to increase almost linearly with increasing temperature having very small temperature coefficient of resistance of the order of 10^{-3}/K.
- Large area (~ in the dimension of μm) defect free single and multi-layers graphene films were successfully deposited on Ni foil by HFCVD at distance of 1.5 cm between filament and substrate. This is relatively new method for the growth of large area high quality graphene. Growth of defects free single layer graphene using HFCVD method reported for the first time by our group during present thesis work.
- The HFCVD method is also suitable for the growth of high quality large area multi-layers graphene films at relatively low substrate temperature as compared

to other CVD method, since in HFCVD method precursor gases decompose at very high filament temperature of ~ 2000 – 2200 °C.

- Graphene films have low resistance (~ 500 ohm) and are highly transparent (~ 90%) in Vis-NIR region, which is very good for the new generation of transparent electrodes in optoelectronic devices.
- Third order optical nonlinearity is observed in CNF as well as multi-layers graphene thin films. The value of third order nonlinear refractive index coefficient (n_2) is of the order of 10^{-5} cm^2/W. This indicates that planar or vertically aligned graphene films may also be used as nonlinear medium in the field of nonlinear photonics.
- Reduced graphene oxide (GO) thin films are fabricated by thermal reduction of GO at different annealing temperatures of 130, 200, 300 and 400 °C for 1h. GO films are highly insulating and conductivity of the films are increased with increase in annealing temperature. This indicates that electrical properties of GO can be tuned by thermal reduction of GO at different temperature.
- Graphene channel field effect transistor (GFET), having channel length of 60 μm, is fabricated using multi-layers graphene as deposited by HFCVD method. The observed carrier mobility is ~ 10 cm^2/V-s. The low carrier mobility of our device could be due to discontinuity in the films throughout the channel.

8.2 Scope for future work

Some of the future research scopes based on the present studies could be followings:

- Though, we are able to deposit high fraction of sp^3 bonded diamond like carbon thin films, it could be further improved by the optimization of other deposition parameters such as substrate temperature and process pressure.

- We have studied the fraction of sp^3 bonded carbon in as deposited DLC films on different substrates. Further studies could be done on the mechanical properties, such as hardness, Young's modulus, etc. with different fraction of sp^3 bonded carbon atoms.
- With further optimization of deposition parameters, it might be possible to deposit single layer graphene in large area (~ in mm dimension) using HFCVD method. This may make HFCVD to be a popular method for the growth of large area single layer graphene like other CVD techniques.
- Further studies could be done on the doping of graphene by different atoms like nitrogen, phosphorous, etc. for the opening of band gap in graphene.
- With the increase in requirement of energy, development of energy storage device with high energy density is a challenge. Therefore, further studies could be done on the optimization of porosity of carbon / graphene based composite films while maintaining electrical conductivity to improve the performance of electrodes in storage device such as battery, supercapacitor, etc.

LIST OF PUBLICATIONS

International Journals

1. **Mukesh Singh**, Asha Yadav, Shailendra Kumar, pratima Agarwal, "Annealing induced electrical conduction and band gap variation in thermally reduced graphene oxide films with different sp^2/sp^3 fraction", *Applied Surface Science* **326** (2015) 236 – 242.

2. **Mukesh Singh**, H.S. Jha, Pratima Agarwal, "Growth of large sp^2 domain size single and multi-layer graphene films at low substrate temperature using hot filament chemical vapor deposition", *Materials Letters* **126** (2014) 249 – 252.

3. **Mukesh Singh**, H. S. Jha, Asha Yadav, Pratima Agarwal, "Study of the growth of graphene film on Ni and Si substrates by hot filament chemical vapor deposition", *AIP Conf. Proc.* **1536** (2013) 545 – 546.

4. **Mukesh Singh**, H. S. Jha, Pratima Agarwal, "Synthesis of high density nucleation of nano-crystalline diamond films on non-carbon affinity substrates", *AIP Conf. Proc.* **1538** (2013) 213 – 218.

5. **Mukesh Singh**, H. S. Jha, Asha Yadav, Lalhriatzuala, Dinesh Deva, Pratima Agarwal, "Fabrication of two dimensional carbon nanostructures using hot wire chemical vapor deposition technique", *Proc. of SPIE* **8549** (2012) 854926.

Manuscripts under preparation

1. **Mukesh Singh**, Indrajeet Kumar, Alika Khare, Pratima Agarwal, "Electrical and nonlinear optical properties of carbon nanoflakes grown on corning glass substrates by hot filament chemical vapor deposition".

2. **Mukesh Singh**, Pratima Agarwal, "Raman scattering study on graphene: effect of temperature and excitation wavelength".

Papers presented in International / National conferences

1. **Mukesh Singh**, H. S. Jha, Asha Yadav, Pratima Agarwal, “Synthesis of single and multi-layer graphene films and its application in field effect transistor”, *International Conference on Nanoscience & Technology*, Panjab University, March 3 – 5, 2014.

2. **Mukesh Singh**, H. S. Jha, Asha Yadav, Pratima Agarwal, “Synthesis of reduced graphene oxide thin films by plasma enhanced chemical vapor deposition”, *International conference on Nanotechnology*, Haldia Institute of Technology, West Bengal, October 25 – 26, 2013.

3. **Mukesh Singh**, H. S. Jha, Asha Yadav, Pratima Agarwal, “Study of the growth of graphene film on Ni and Si substrates by hot filament chemical vapor deposition”, *International conference on Recent Trends in Applied Physics & Material Science*, Govt. college of Engineering & Technology, Bikaner, February 2 – 2, 2013.

4. **Mukesh Singh**, H. S. Jha, Pratima Agarwal, “Synthesis of high density nucleation of nano-crystalline diamond films on non-carbon affinity substrates”, *National conference on carbon materials*, BARC Mumbai, November 1 – 3, 2012.

5. **Mukesh Singh**, H. S. Jha, Asha Yadav, Lalhriatzuala, Dinesh Deva, Pratima Agarwal, “Fabrication of two dimensional carbon nanostructures using hot wire chemical vapor deposition technique”, *International workshop on Physics of Semiconductor devices*, IIT Kanpur, December 19 – 22, 2012.